ABSTRACT

Title of dissertation: ULTRA-FAST DYNAMICS OF SMALL MOLECULES IN STRONG FIELDS

Kun Zhao, Doctor of Philosophy, 2006

Dissertation directed by: Professor Wendell T. Hill, III
Institute for Physical Science and Technology
& Department of Physics

Correlation detection techniques (*image labeling*, *coincidence imaging*, and *joint variance*) are developed with an image spectrometer that is capable of collecting charges ejected over 4π sr and a digital camera that can be synchronized with the laser repetition rate at up to 735 Hz. With these techniques, molecular decay channels ejecting atomic fragment ions with different momenta (energies) can be isolated; thus the initial molecular configurations (bond lengths and/or bond angles) and orientations as well as their distributions can be extracted. These techniques are applied to study strong-field induced dynamics of diatomic and triatomic molecules.

Specific studies included the measurement of (1) the Coulomb explosion energy as a function of bond angle in linear (CO_2) and bent (NO_2) triatomics and (2) the ejection anisotropy relative to the laser polarization axis during Coulomb explosions in both triatomic (CO_2 and NO_2) and diatomic (H_2, N_2 and O_2) systems. All the experiments were performed with 100 fs, 800 nm laser pulses focused to intensities

of $0.1 \sim 5.0 \times 10^{15}$ W/cm^2.

The explosion energy of NO_2 decreases monotonically by more than 25% from the smallest to the largest bond angles. By contrast, the CO_2 explosion energies are nearly independent of bond angle. The enhanced ionization and static screening models in two-dimension with three charge centers were developed to simulate the explosion energies as a function of bond angle. The predictions of both models are consistent with the measurements of CO_2 and NO_2. At the same time, the observed explosion signals as a function of bond angle for both CO_2 and NO_2 show large-amplitude vibrations. The peaks of the explosion signal distributions for both CO_2 and NO_2 appear near the equilibrium bond angles of the neutral systems.

The ejection angular distributions in triatomic (CO_2 and NO_2) and diatomic (H_2, N_2, and O_2) Coulomb explosions were measured; the contribution made to the ejection anisotropy by geometric and dynamic alignment was studied by comparing the images obtained with linearly and circularly polarized fields. Different angular distributions of the molecules are consistent with different ionization stages, induced dipole moments and rotational constants. A narrower distribution of H_2 than other diatomics is confirmed by its nearly complete dynamic alignment in the field. The results also show that the large dynamic alignment in the linear triatomic CO_2 is consistent with the fact that more electrons have been removed and the precursor molecular ion spends more time in the field prior to the explosion than diatomic systems such as N_2 and O_2.

ULTRA-FAST DYNAMICS OF SMALL MOLECULES IN STRONG FIELDS

by

Kun Zhao

Dissertation submitted to the Faculty of the Graduate School of the
University of Maryland, College Park in partial fulfillment
of the requirements for the degree of
Doctor of Philosophy
2006

Advisory Commmittee:

Professor Wendell T. Hill, III, Chair/Advisor
Professor Julius Goldhar, Dean's Representative
Professor Millard Alexander
Professor Rajarshi Roy
Professor Robert Walker

DEDICATION

This dissertation is dedicated to my grandparents.

ACKNOWLEDGMENTS

This work partially belongs to my wife, Xuanxuan, the best thing that ever happened to me. She is a good wife and my best friend. She gives me all the help, support and love in every facet of my life and research. Without her, my life would be in vain.

First and foremost I'd like to thank my advisor, Professor Wendell Hill for giving me such an extraordinary opportunity to challenge physics as well as myself and have fun in the process. He is an excellent advisor and a nice person. Without his extreme patience and constant guidance over the past years, this work would be simply impossible. His knowledge and insight on physics has enriched me. It has been a great pleasure to work with and learn from him.

Special thanks are extended to my defense committee members whose names begin this dissertation. I could not ask for a more qualified group for the final step of my graduate study. Special thanks are also extended to Mr. Tim Howard and Mr. Lee Elberson, who read this entire manuscript and gave me enormous help on the language.

My colleagues in our group have enriched my school life in many ways. Mr. Ilya Arakelyan, Mr. Narupon Chattrapiban, Mr. Vishal Chintawar, Mr. Lee Elberson, and Dr. Menkir Getahum have always helped and supported me. I really enjoy talking about physics, philosophy, music, movies and everything else with them. I

wish them a successful career.

I would also like to acknowledge help and support from professors and staff members of Institute for Physical Science and Technology and Chemical Physics Program, Dr. Michael Coplan, Dr. Millard Alexander, Dr. Michael Fisher, Dr. Rajarshi Roy, Mrs. Diane Mancuso, Mrs. Patricia Wynn, and Mrs. Debbie Jenkins in particular. Their help is highly appreciated.

I owe my deepest thanks to my mom, dad and sister who have always cared for me, loved me and talked to me. I am so lucky to be born into such a wonderful family. I wish my grandparents could see my graduation. May they rest in peace.

TABLE OF CONTENTS

LIST OF TABLES

LIST OF FIGURES

Chapter 1

INTRODUCTION

1.1 Motivation and Goal

For decades, physicists, chemists and laser engineers have been fascinated by the possibility of controlling molecular dynamics and chemical reactions with lasers. This interest is driven in part by the desire to produce unusual products or to enhance reaction rates that are not easily obtained by statistical means. Schemes for laser-based control have been the subject of investigation both theoretically and experimentally (see, for example, Refs. [1] – [8]). Control approaches have been applied to a variety of different molecular processes – laser-induced dissociation [3], bond rearrangement [5], and dissociative ionization [6] are a few examples. Many control experiments involve intense and/or "shaped"[1] laser pulses. Most often these shaped pulses are very complicated and the affect they have on the molecular system is not clear. Consequently, there is a need to develop ways to probe the molecular system during excitation with these intense and exotic pulses. The research presented in this thesis is part of an effort to develop ways to probe molecular systems during and after excitation that will reveal the physics and dynamics induced by

[1]The temporal and/or spectral profile (or "shape") of a laser pulse can be adjusted or changed by certain devices such as a liquid-crystal or acousto-optic modulator, which can delay the phase and/or reduce the amplitude of certain frequency components of the pulse, or eliminate some components completely. The adjusted pulse is usually referred to as a "shaped" pulse and the process as pulse shaping.

such control pulses.

The contribution this thesis makes to this effort is two-fold: (1) the development of image-based correlation techniques to capture snap-shots of the molecular structure from which bond angles and bond lengths at the time the system falls apart can be extracted and (2) the application of the developed techniques to investigate bond-angle dependence, anisotropy and alignment issues associated with intense-field dissociative-ionization of 2- and 3-atom systems. The detection tools developed and the knowledge gained through the experiments presented here will aid future experiments probing more complicated aspects of the dynamics. Ultimately, this approach can be applied to investigate dynamics in larger systems with transform-limited[2] and/or shaped laser pulses.

In an attempt to make direct measurements of the molecular structure, scientists launched the field of Coulomb explosion imaging with fast molecular beams (for example, see Refs. [9, 10, 11]). In these experiments, a beam of molecular ions was accelerated through thin foils. When the molecular ions pass through the foil, several electrons are stripped away on a sub-femtosecond time scale before the constituent atoms can move very far. The resulting highly charged molecular ions explode into atomic ions due to their mutual Coulomb repulsion. Since the time scale of the beam-foil interaction is on the order of femtoseconds or even shorter, the internal motion of the molecular ion is essentially frozen when the explosion is initiated. Thus, the trajectories of the fragments contain the information about

[2]The minimum value of the time-bandwidth product of a pulse is about $\Delta f \cdot \tau \gtrsim 0.5$, where Δf is the frequency spread of the optical spectrum and τ is the pulse width [12]. The transform limit is the minimum pulse width that is possible for a given spectrum. A pulse at this limit is called transform-limited.

the state of the parent molecular ion prior to the explosion. In beam-foil experiments, two-dimensional area detectors were used to capture the fragments providing graphical views of the structure. However, since the molecular ions are moving in the laboratory frame, the image must be transformed to retrieve views of the structure in the molecular frame.

Inspired by the beam-foil experiments, Coulomb explosion experiments were begun with intense sub-picosecond lasers [13, 14]. In the laser experiments, time-of-flight (TOF) detectors were used initially to capture the fragments. In contrast to the beam-foil studies, which is no longer an active field, investigations based on laser-induced Coulomb explosions continue to be a thriving area of research both experimentally [15] – [69] and theoretically [70] – [97]. This is fostered by the flexibility laser-based experiments afford. In particular, the laser can participate in the dynamics by exciting the precursor molecule to specific states prior to the explosion. The disadvantage of laser-based experiments is the pulse duration, 10 – 100 fs. At the longer times, the molecules have time to evolve during the irradiation. While the laser-molecule interaction leads to many complications, it provides a knob for controlling the dynamics. However, in order for control to be fully realized, a better understanding of the laser-molecule interaction is critical.

In light of this brief overview, the two primary goals of this study are (1) to develop quantitative detection techniques to probe laser-induced dynamics of small molecules associated with Coulomb explosions and (2) to investigate bond-angle-specific explosion, ejection anisotropy and dynamic alignment. With these techniques, the experiments were performed with transform-limited pulses that had

widths of 100 fs (full width at half maximum, FWHM) and focused intensities of $0.1 - 5.0\times10^{15}$W/cm^2. The results provide a foundation upon which future studies involving more exotic pulses can be built.

1.2 Research Background and Contributions of This Study

Dissociative ionization of molecules, induced by short and intense laser pulses (pulse widths $\tau = 50$ fs – tens of picoseconds and intensities $I \geq 10^{14}$ W/cm^2), has been under intensive investigation [14] – [97] for more than fifteen years. Both experimental and theoretical investigations started with diatomics, and many different molecules have been studied. Examples include H_2 [15] – [22], D_2 [15, 19, 23], HI [14], N_2 [13, 24] – [39], O_2 [28, 32, 40] – [42], CO [27, 28, 31, 43] – [45], NO [46, 47], Cl_2 [37, 41, 42, 48], Br_2 [41, 42], I_2 [37, 41, 42, 49] – [55]. Triatomic molecules have also been investigated, such as CO_2 [32, 36, 56] – [63], N_2O [32, 64], CS_2 [65], OCS [66], H_2O [32, 67], NO_2 [63, 68] and SO_2 [33, 69]. Early experiments used TOF ion mass spectroscopy to collect and analyze the atomic ions following Coulomb explosions, as we have mentioned. Two-dimensional position-sensitive detectors, which were first introduced in this lab [22], have become the primary workhorse for contemporary experiments because they are capable of detecting fragments ejected into different angles simultaneously, allowing the angular distributions to be extracted [23, 54, 62, 63, 65].

When this research started, nearly all previous analyses were based on TOF spectra or pseudo-images composed of TOF spectra obtained by rotating the po-

larization axis of the laser relative to the TOF axis. The distinguishing mark of a Coulomb explosion, however, is the molecular decay into atomic ions. Since the ions ejected from a system with three or more atoms are not along a straight line, in general, the explosion partners could not be collected simultaneously in previous studies, requiring numerical simulations and momentum (and energy) conservation to be used to identify explosion partners. Unfortunately, this identification is not necessarily unique, even for diatomic explosions. *Covariance mapping* was introduced by Frasinski *et al.* [98] to identify partners in TOF waveforms uniquely using a covariance between different charges obtained from a large number of laser shots. However, when used on TOF waveforms, it is difficult to extract quantitative information for bent explosion channels. At the same time, TOF imaging and covariance mapping are incompatible and have to be done in separate experiments. Thus, the images acquired from TOF waveforms cannot be used to determine specific bond angles. Consequently, there was a need for a new approach to study larger systems. To that end, laser-induced Coulomb explosion of 3-atom systems was re-examined with the techniques developed in this work, which are more sensitive to molecular geometry and orientation with the laser polarization axis.

The work in this thesis employed momentum imaging based on the image spectrometer capable of collecting all explosion partners ejected into 4π sr introduced by Zhu and Hill [22], which was the first study where a two-dimensional area detector was employed to investigate laser-induced Coulomb explosions as well as the first study to extend the correlation technique to two-dimensional images (a two-dimensional analogue of *covariance mapping*). The 4π image spectrometer coupled

to a high frame-rate digital camera affords high event rates in the detection [99, 100]; several hundred ions per laser pulse can be handled in principle, significantly higher than other imaging techniques, such as COLTRIMS (cold-target recoil-ion momentum spectroscopy, developed at nearly the same time as our approach) with delay-line anodes [23, 65, 101, 102]. The high event-rate of our approach ensures that a large number of explosion events can be collected in a reasonable time so that the statistical-based correlation approach can be applied to isolate ions arriving at specific times or having specific momenta. The following techniques were developed in this work, *image labeling* [99], *coincidence imaging* [63], and *joint variance* [103].

The first important observation [13] in laser-induced dissociative-ionization (Coulomb explosion) experiments is with relatively long pulses that the total final kinetic energy (also referred to as *kinetic energy release*) of the atomic fragment ions is much less than the Coulomb potential energy determined at the equilibrium bond length (R_e) of the molecule assuming pure Coulomb repulsion. The energy deficit is about 50% for molecules composed of light atoms (H, C, N, O, etc.), and decreases to about 30% for molecules with heavier atoms (Cl, I, for example) [70]. The universality of the deficit, which is a slow function of charge states, suggests residual bonding is probably not the primary cause. The deficit is consistent with two possibilities: enhanced ionization [14, 53, 70] – [78] and electron screening [79] – [82]. The enhanced-ionization model assumes that the positively charged molecular ion explodes at a critical internuclear separation (R_C) where the molecular ionization rate peaks. Consequently, it is far easier to reach an ionization stage that supports the Coulomb explosion at R_C. The electron-screening model assumes

ionization starts at R_e but the positive charges are screened by the photo-electrons that have not left the vicinity of their parent molecule. The energy deficit results from the positive ions moving through the cloud of the photo-electrons causing them to decelerate, so that the final kinetic energy is smaller than the original Coulomb potential energy of the ions at R_e in the absence of the electrons. Details of these models will be discussed in the next chapter.

A second observation is that strong-field dissociative ionization induces large-amplitude bending motion and structural deformation in triatomic systems. Large-amplitude bending about the equilibrium bond angle has been observed in triatomic systems, such as CO_2 [56, 58, 60, 61], SO_2 [33, 69] and OCS [66]. Bent molecules, NO_2 [68] and H_2O [67], were found to be deformed toward the linear configuration while linear CS_2 [65] was reported to be distorted toward a bent configuration. Furthermore, the evidence also suggested that the explosion energy can depend on the bond angle [65]. The dynamics associated with triatomics in strong fields has also been studied theoretically with the time-dependent Schrödinger equation, field-induced adiabatic states and the potential surfaces [83, 84, 85]. For CO_2, these studies showed that the laser-deformed CO_2^{2+} potential surface favors the symmetric bond stretching that triggers the large-amplitude bending motion of CO_2^{2+}.

To exam laser-induced affects in 3-atom systems with 2D imaging, we focused our studies on two systems: CO_2 [62] and NO_2. The purpose was to compare linear and bent systems and their responses to light. We used the correlation techniques developed to isolate specific precursor molecular geometries (bond angles prior to explosion). The experimental results contain several interesting features. For example,

the explosion energy for NO_2 decreases monotonically by ∼25% from the smallest to the largest bond angle. By contrast, the CO_2 explosion energy is nearly independent of bond angle. To simulate the explosion, we extended the one-dimensional 2-atom enhanced ionization model [70, 73, 74] into two-dimension for three charge centers and developed a single-parameter static-screening model based on the concept of electron-screening effect [79] – [82]. In the enhanced-ionization model, the bond-angle dependence of the explosion energy is primarily due to the variation of the energy levels of the electronic states at three charge centers. In the static-screening model, the variation of the explosion energy as a function of the bond angle is related to the density and shape of the photo-electron distribution around the exploding molecular ion. The predictions of both the enhanced-ionization and static-screening models are consistent with the measured explosion energies for CO_2 and NO_2. At the same time, we observed large-amplitude vibrations in explosion signals of both CO_2 and NO_2.

The third important observation in laser-induced dissociative-ionization experiments is that the angular distribution of the ejected atomic ions is anisotropic. For diatomics, the ions are ejected along the polarization axis of the laser primarily [13]. Atomic ions ejected from triatomics have a large propensity for coupling to the polarization axis as well [58]. Specifically, the outer ions are ejected primarily along the polarization axis while the central ion tends to be ejected in a direction that is perpendicular to the polarization axis.

The ejection anisotropy has been the subject of constant debate for nearly two decades [13, 36, 37, 39, 41, 42, 61, 63, 69, 86]. Two effects contribute to the

anisotropy, the so-called geometric [13, 86] and dynamic alignment [45, 87]. Geometric alignment relies on the induced dipole moments being larger along the molecule than opposite. Thus, it is easier to ionize the molecule when its molecular axis is parallel to the laser polarization axis. The molecule that explodes are aligned with the polarization axis producing the anisotropy. Dynamic alignment refers to the field exerting a torque on the molecular axis, inducing the molecule to rotate itself into alignment with the field prior to the Coulomb explosion. When active, more molecules participate in dissociative ionization than would in its absence.

Geometric and dynamic alignment are commingled in typical Coulomb explosion experiments performed with linearly polarized light, making them difficult to be distinguished. Several authors have pointed out that enhanced ionization will ensue without dynamic alignment in circularly polarized fields since the polarization axis rotates too quickly (a period of $T = \lambda/c = 2.67$ fs, where c is the speed of light and $\lambda = 800$ nm is the laser wavelength) for the molecule to respond to the instantaneous torque [36, 39, 41, 42, 61]. Thus far, previous studies have provided tests for determining when dynamic alignment is active. With only a few exceptions, however, the bulk of the work has focused on diatomics. The correlation detection techniques we developed, with an ability to isolate orientations of the molecular axis (the line connecting the two outer atoms in the system) relative to polarization axis in triatomics, provides a unique opportunity to study alignment issues for more complex explosions. Comparing explosion images induced by linearly and circularly polarized fields not only allows the two effects to be distinguished, it provides a quantitative measure of the contribution that dynamic alignment makes

to the anisotropy. We studied ejection anisotropy in the images of triatomic (CO_2 and NO_2) [63] and diatomic (H_2, N_2, and O_2) systems. Of these systems, the ions ejected from CO_2 and NO_2 were observed to have narrower distributions than N_2, O_2 and H_2. The narrower distributions can be explained in terms of the ionization stage the precursor molecule reaches before the explosion, the induced dipole moment and moment of inertia of the system. The degree of dynamic alignment of H_2 is the highest among the samples, due to its small moment of inertia. Surprisingly, however, the degree of dynamic alignment for CO_2 was found to be larger than those for N_2 and O_2, which have smaller moments of inertia. We explained this in terms of the length of time the precursor molecular ion spends in the field prior to the Coulomb explosion.

This manuscript is organized as the following. Chapter 2 reviews the existing theories and models of strong-field molecular dynamics. The apparatus including the laser system, the image spectrometer, and the digital camera are described in Chapter 3. The correlation detection techniques are introduced in Chapter 4. Chapter 5 presents the experimental results and the analysis with the theoretical models. Chapter 6 gives the summary and possible future work related to this study. All the formulas in this thesis are in MKS units, except where explicitly specified otherwise.

Chapter 2

BASIC CONCEPTS IN STRONG-FIELD MOLECULAR DYNAMICS

This chapter provides a review of two models that have been suggested to explain the energy deficit observed during Coulomb explosions with laser pulses longer than 50 fs (Sec. 2.1). The mechanism behind the anisotropy of the ejected ions observed in laser-induced Coulomb explosions of diatomic and triatomic molecules (Sec. 2.2) is also summarized.

2.1 Kinetic Energy Release

At laser intensities higher than 10^{14} W/cm^2, the strength of the average electric field is more than 2.7×10^8 V/cm, which is a significant fraction of the internal field of the valence electrons in atoms and molecules (on the order of 10^9 V/cm) leading to ionization. Non-resonant ionization of atoms and molecules in intense laser fields can be divided into two regimes by the Keldysh parameter γ [104],

$$\gamma = \sqrt{\frac{I_p}{2U_p}}, \qquad U_p = \frac{e^2E_0^2}{4m_e\omega^2}, \qquad E_0 = \sqrt{\frac{2I_0}{\epsilon_0 c}}, \tag{2.1}$$

where I_p is the atomic or molecular ionization potential; U_p is the ponderomotive potential, a measure of the quiver energy of a free electron in an oscillating field; e, m_e, E_0, ω, I_0, ϵ_0 and c are the elementary charge, the electron mass, the peak field strength, the angular frequency, the peak intensity of the laser, the permittivity of

free space, and the speed of light, respectively. The Keldysh parameter represents the ratio between the laser and electron-tunneling frequencies. For $\gamma \gg 1$, the laser frequency is much higher than the tunneling frequency and the ionization is a multiphoton process. The atom or molecule is ionized as several photons are absorbed simultaneously. This occurs for short-wavelength laser fields. For $\gamma \ll 1$, the high-intensity and long-wavelength regime, the electron can gain enough energy ($U_p > I_p$) to tunnel out of the potential barrier within one laser cycle so that tunneling ionization dominates and the ionization rates are less dependent on the laser frequency and the internal structure of the atom or molecule. Dissociative ionization due to intense laser fields in the visible and infrared range has a Keldysh parameter $\gamma \leq 1$, and the multiphoton mechanism no longer applies. At the same time, the nuclear motion makes molecular ionization more complicated than the atomic case. The ionization rate is affected by the nuclear separation in a molecule and dissociation and ionization are interlaced, making the theoretical predictions more difficult. Thus, models of molecular ionization where $\gamma \sim 1$ must consider multiple charge centers and explain the dynamics of both electrons and nuclei in laser-induced dissociative ionization. Under such circumstances, two main streams of theoretical work have been suggested to explain the energy deficit of the Coulomb explosion in the experiments.

The first model (Sec. 2.1.1) is based on *enhanced ionization* at a critical internuclear separation (R_C) [14, 53, 70] – [78]. It assumes that the positively charged molecular ion explodes at R_C. The value that R_C assumes is dictated by the fact that laser-induced ionization of the molecule to the critical ionization stage (the

stage where enough electrons have been removed so that the system explodes) is far easier at R_C than at R_e. The final kinetic energy is determined by the relatively small Coulomb potential energy of the fragment ions at R_C. The second model (Sec. 2.1.2) assumes ionization starts at R_e but the positive charges are screened by the photo-electrons that have not left the vicinity. This *electron-screening* effect [79] – [82] has been calculated in the Thomas-Fermi description of the electrons [88, 105], which treats the electrons as a continuous distribution. The energy deficit results from the positive ions moving through the cloud of the photo-electrons causing them to decelerate, so that the final kinetic energy is smaller than the original Coulomb potential energy of the ions at R_e in the absence of the electrons.

2.1.1 Enhanced Ionization and Charge Resonance

A classical over-the-barrier ionization model was first applied to calculate the appearance intensities[1] of different charge states of atoms in intense laser fields [106]. As this calculation was extended to diatomic molecules, enhanced ionization at R_C was discovered [53, 70, 73, 77]. This phenomenon was also found in the quantum treatment of molecular dissociative-ionization [73] – [76, 78], and interpreted by the dynamics of the charge-resonance (CR) states, which are the two lowest eigenstates of the electron in a symmetric double-well Coulomb potential [107, 108]. The R_C predicted by classical and quantum calculations is comparable and believed to be the origin of the energy deficit observed in the Coulomb explosion experiments.

[1] Appearance intensity of a charge state is usually understood as the minimum laser intensity at which this charge state is produced.

In atomic cases [106], a single valence electron is placed in the Coulomb potential of the ion core and a static field consistent with the peak laser intensity. The electron energy level is determined by the ionization potential of the atom or ion. As the strength of the laser field increases, the Coulomb potential barrier is lowered. Ionization is assumed to occur when the height of the barrier is equal to the electron energy level (over-the-barrier ionization, Fig. 2.1a). Assuming the laser polarization is along the x-axis and the origin is at the nucleus, the combined potential in one dimension and the electron energy level can be expressed as,

$$V_{atom} = -\frac{Kqe}{|x|} - eE_0x, \qquad \varepsilon_{atom} = -I_p, \tag{2.2}$$

where qe is the charge of the ion, E_0 is the peak field strength of the laser, I_p is the field-free ionization potential, and $K = 1/(4\pi\epsilon_0)$ is the constant of proportionality in Coulomb's law in MKS units – Coulomb's constant. The potential barrier is found at x_0 where $\partial V_{atom}/\partial x = 0$. The intensity required for over-the-barrier ionization can be determined by equating the height of the potential barrier $V_{atom}(x_0)$ to the electron energy level, $-I_p$. The appearance intensities predicted in such a simple model agreed very well with the experimental results of noble gases [106] (Fig. 2.2). Since tunneling ionization begins before the electron energy level reaches the potential barrier, the appearance intensity and over-the-barrier ionization described in this simplified model are actually the saturation point of tunneling ionization. However, in a classical point of view, the terms "appearance intensity" and "over-the-barrier" are justified. Thus, they will be used in the following discussion of classical field ionization.

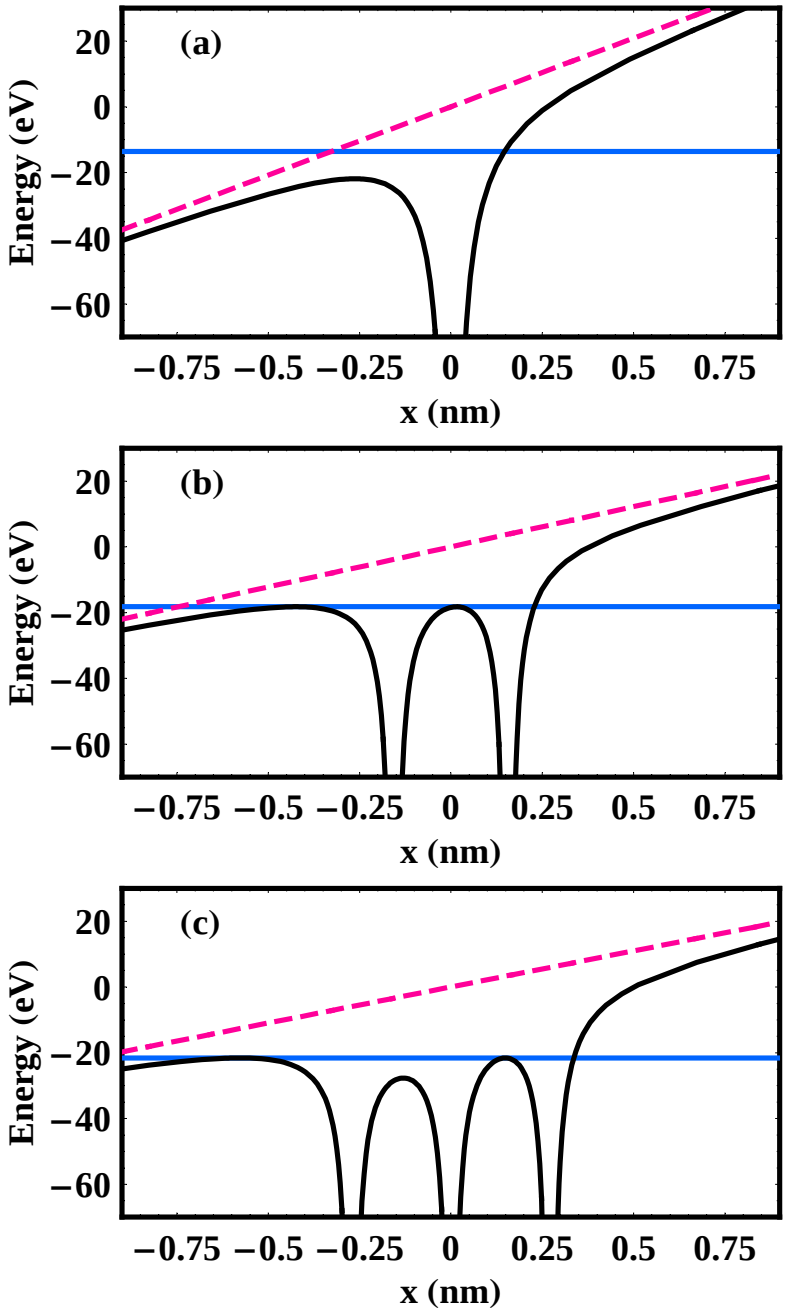

Figure 2.1: Classical over-the-barrier ionization model of an electron in the combined atomic or molecular field and laser field for (a) atomic (X^{q+}), (b) diatomic (X^{q+}, X^{q+}), and (c) linear triatomic (X^{q+}, X^{q+}, X^{q+}) systems. The black, blue and red curves represent, respectively, the electron potential energy as a function of the electron position, the electron energy level, and the laser-electron coupling eEx in eV. The laser electric field is pointing to the left.

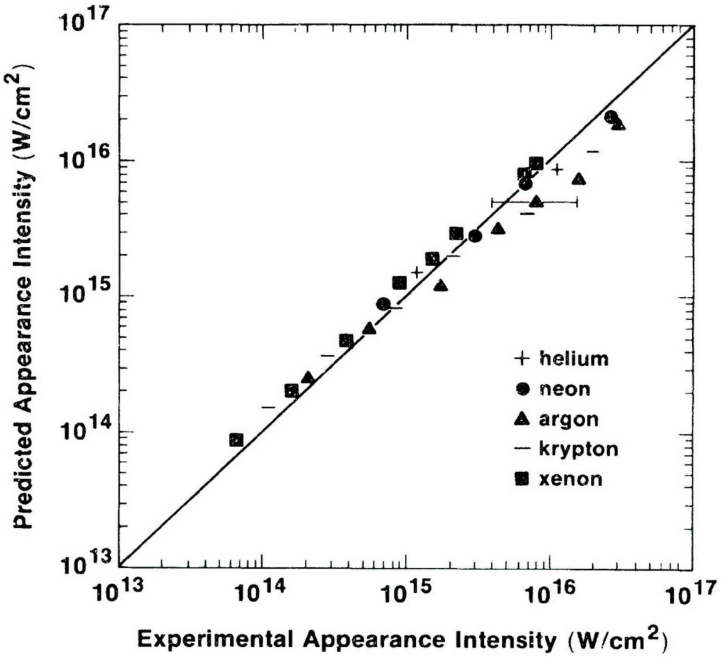

Figure 2.2: Comparison of experimentally determined and theoretically predicted appearance intensities using a simple classical theory. The solid line corresponds to exact agreement. (Fig. 3 of Ref. [106]) Reprinted figure with permission from S. Augst, D. Strickland, D. D. Meyerhofer, S. L. Chin, and J. H. Eberly, Phys. Rev. Lett. **63**, 2212 (1989). Copyright (1989) by the American Physical Society.

For diatomic molecules, a similar field-ionization model was introduced by Codling *et al.* [14, 71, 72]. The valence electron of a molecule or molecular ion is placed in the classical Coulomb potential well of two point-like ion cores (Fig. 2.1b). The electron energy level is determined by the ionization potential of the atom or atomic ion shifted by the Coulomb force of the other ion. When the static field of a linearly polarized laser is applied along the molecular axis, the potential well is distorted. In addition to the same potential barrier of the combined field as in the atomic case, there is also an inner barrier between the two ions in a diatomic molecule. The heights of these two barriers depend not only on the field strength (laser intensity), but also on the separation between the two nuclei. Later,

the combined potential field in diatomic over-the-barrier ionization (also in one dimension) was derived as [53, 70, 73, 74, 77]

$$V_{mol} = -\frac{Kq_1e}{|x - R/2|} - \frac{Kq_2e}{|x + R/2|} - eE_0x, \tag{2.3}$$

and the electron energy levels in the double-well potential (Fig. 2.1b) were given by

$$\begin{aligned} \varepsilon_+ &= -q_1I_{p1} - Kq_2e/R + eE_0R/2, \\ \varepsilon_- &= -q_2I_{p2} - Kq_1e/R - eE_0R/2, \end{aligned} \tag{2.4}$$

where the subscripts, + and −, refer to the energy levels in the up-hill and down-hill potential wells, respectively; q_1e and q_2e are the charges of the two ions; E_0 is the peak field strength; R is the internuclear separation (bond length); $K = 1/(4\pi\epsilon_0)$; I_p is the ionization potential of the atom and ionization potential of the ion with charge qe is assumed proportional to the atomic ionization potential, $I_p^{(q)} = qI_p$ [74]. The $eE_0R/2$ term accounts for the Stark-shift. The laser polarization and the molecular axis are along the x-axis, and the origin is at the center of the molecule.

At short bond lengths, near R_e, the electron can move freely between the nuclei. Ionization is difficult because the electron is confined by the potential well. As the bond length increases and the nuclei move apart, the inner barrier increases to block the movement of the electron. When the electron is trapped (electron localization) in the up-hill potential well, the right well in Fig. 2.1b, the electron energy level is Stark-shifted upward by $eE_0R/2$ (Eq. 2.4). When the electron energy level is high enough to overcome both the inner and outer barriers, the system ionizes. If the bond length increases further, the inner barrier also increases so

that ionization requires a higher intensity. For a given molecule or ion, there is an optimum bond length – R_C – where the electron energy level in the up-hill well is at the same height as both the inner and outer barriers (Fig. 2.1b), and the ionization occurs at a minimum intensity [14, 53, 70, 71, 72, 77].

The appearance intensities of the diatomic molecular ions can be estimated in a similar manner as in the atomic case. The inner and outer potential barriers can be found at x_{inner} and x_{outer} where $\partial V_{mol}/\partial x = 0$. The ionization field amplitude at a specified internuclear separation can be determined by equating the height of the inner potential barrier $V_{mol}(x_{inner})$ to the electron energy level in the up-hill potential well ε_+. It is also required that the outer potential barrier be lower than or equal to the inner barrier, $V_{mol}(x_{outer}) \leq V_{mol}(x_{inner})$, so that the electron can pass over the down-hill potential well and enter the continuum after it passes the inner barrier. The lowest appearance intensity is found at $R_C \simeq 4/I_p$ (in atomic unit) [70], where $V_{mol}(x_{outer}) = V_{mol}(x_{inner}) = \varepsilon_+$. The kinetic energy release of the fragment ions due to the Coulomb explosion can be predicted from $\mathcal{E}_k = Kq_1q_2e^2/R_C$. The energy deficit is defined as the difference between the kinetic energy release and the Coulomb potential energy at R_e,

$$\mathcal{E}_D \equiv \mathcal{E}_C - \mathcal{E}_k = K\frac{q_1q_2e^2}{R_e} - K\frac{q_1q_2e^2}{R_C}. \tag{2.5}$$

The predictions were in agreement with the experimental measurements [70]. This model can be extended to triatomic systems (Fig. 2.1c) [32, 66].

The electron localization and over-the-barrier ionization were also investigated with quantum calculations [73] – [76, 78]. The ionization rates at different inter-

nuclear separations of diatomic molecules were calculated from the time-dependent Schrödinger equation of the valence electron. A smoothing parameter ($s \sim 0.1$ nm) was employed in one-dimensional calculations to remove the singularities of the Coulomb potential and can be adjusted to give similar ionization potentials as the exact three-dimensional systems [73, 76]. The maximum of the ionization rate – *enhanced ionization* – was found at an R_C similar to that predicted by the classical calculation.

In the quantum treatment, the electron energy levels in the combined field of the Coulomb potential and the laser radiation are assumed to be related to charge-resonance states (Eq. 2.4) [107, 108]. There are two important factors related to the charge-resonance states [73] – [76]. First, their dipole transition moment grows linearly as $R/2$ when the internuclear distance increases. A sufficient population can be pumped into the upper state or upper potential well by the oscillating field. If the internuclear separation is large enough to raise the inner potential barrier, the electron will be confined in the upper well and the transition from the upper state to the lower state will be suppressed – electron localization. Second, the electron in the upper charge-resonance state is freed when the laser field reduces the potential barriers. Thus, the population in the upper level is removed by the field in an efficient and fast manner – enhanced ionization. At smaller internuclear separations, the population in the upper state is not sufficient to enhance the ionization. At larger separations, although the upper state is well populated, the higher potential barriers reduce the ionization rate. In both cases, ionization will have a lower rate or require a higher laser intensity. In short, dynamic localization of the charge-resonance states

and static barrier suppression by the laser field lead to an enhanced ionization rate at R_C.

Numerical calculations using the time-dependent Schrödinger equation have been extended to two-electron molecules (H_2) [89, 90, 91], and triatomic cases (H_3^{2+} and H_3^+) [92] – [95]. The critical internuclear separation in triatomic molecules, again assuming charge-resonance transitions, leads to $R_C \simeq 5/I_p$ (in atomic unit) where R_C is the distance between two end atoms in the molecule [94].

Although the energy deficit in the Coulomb explosion predicted by R_C (Eq. 2.5) agrees with the experimental data, the enhanced ionization model has several weak points. First, the model does not explain how the molecule stretches to R_C. Recent quantum mechanical calculations for CO_2 using time-dependent adiabatic states and their potential surfaces [83, 84, 85] have shown that the neutral molecule does not stretch to R_C but the ionic states (CO_2^{2+}, for example) do stretch on a time scale comparable to the laser pulse width ($\sim$ 100 fs). Second, the photo-electrons are assumed to leave the vicinity of the molecular ion instantly after ionization. However, a combination of the facts that the photo-electrons will be attracted back to the positive molecular ion and that a significant part of them will be trapped by the laser field [109, 110] means that there will be a cloud of electrons remaining in the vicinity of the molecular ion. Thus, the electrons may need to be taken into account in order to understand laser-induced molecular dissociative ionization.

2.1.2 Electron Screening Effect

The model that includes the effects of the electrons is based on a reduced repulsive Coulomb force between the atomic ions. The observed energy deficit is explained by the photo-electrons decelerating the exploding molecular ion, which was first mentioned by Cornaggia *et al.* [29, 56].

In the electron screening model [79] – [82], the electrons start to be removed from the molecule at R_e when the laser field is applied. The positively charged atomic cores start to repel each other under the mutual Coulomb repulsion. As more electrons are being removed, they do not leave rapidly, but form a cloud near the atomic cores. As the atomic cores move through the cloud of electrons, a larger volume of the electron cloud is enclosed in the increasing space between nuclei. The resultant electron-screening effect decelerates the motion of the fragments significantly such that the observed kinetic energy release is smaller.

The electron-screening effect was calculated in the Thomas-Fermi model, which treats the electrons as a continuous distribution of charged particles. A density function $\rho_e(\vec{r})$, instead of wave functions for individual particles, is employed to represent the electrons in the system. The electrons, in an atom or molecule, fill all the energy levels up to the Fermi energy in the mean field $\Phi(\vec{r})$, which is an average electrostatic potential of the electron distribution and the nuclear charges. The number density of the electrons with energies lower than the Fermi energy (ε_F) is given by [105]

$$n(\vec{r}) = \rho_e(\vec{r})/m_e = \frac{[2m_e(\varepsilon_F - e\Phi(\vec{r}))]^{3/2}}{3\pi^2\hbar^3}, \tag{2.6}$$

where m_e is the mass of electron. In an external field, $\Phi(\vec{r})$ is determined self-

consistently by the external field and the combination of the electron distribution and the nuclear charges. The electron density depends on the mean field. If the external field is large enough, the electrostatic potential is bent at some $\vec{r}$ where the electron density drops below zero, which means some electrons spill over the potential barrier and ionization occurs.

To study a molecule subject to a short laser pulse of optical frequency in this model, a time-dependent approach is used [79] – [82, 111] where the hydrodynamic equations describe an electronic fluid shaken by an external oscillating field. Besides a time-dependent mass density $\rho_e(\vec{r}, t)$ similar to $\rho_e(\vec{r})$ in Eq. 2.6, a velocity field $\vec{v}(\vec{r}, t)$ is introduced to characterize the dynamics of such an electron fluid in a many-electron system. The time-dependent mean field $\Phi(\vec{r}, t)$ is determined by the oscillating field and the strong internal interaction of the fluid self-consistently and governs the motion of the fluid. With appropriate initial conditions – the electron density $\rho_e(\vec{r}, t = 0)$ and the electrostatic field $\Phi(\vec{r}, t = 0)$ of the molecular system without the external field – the density and velocity fields are found numerically on a space grid at each temporal step. The kinetic energies of the fragment ions are also calculated at the same time.

The Thomas-Fermi description of the electrons was first applied to calculate the appearance intensities for atomic ionization and the results were in agreement with measurements [88, 111]. For molecules, interlaced ionization and dissociation were observed in the time-dependent numerical simulation. The result of Brewcyzk *et al.* [79, 80, 81] clearly showed the early acceleration and later deceleration of the nuclei in the process of the Coulomb explosion of Cl_2 induced by an intense laser

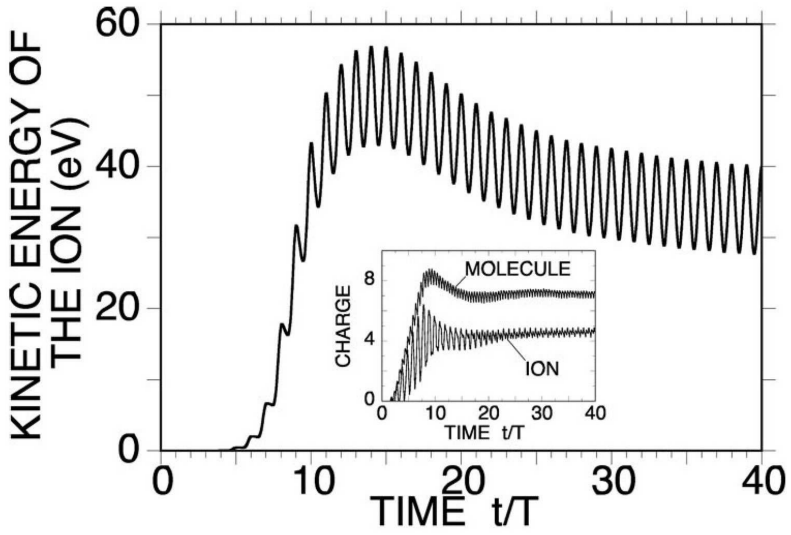

Figure 2.3: Simulated evolution of the features of the Cl_2 molecule for a linearly polarized laser pulse with a peak intensity of 1.25 $\times 10^{16}$ W/cm^2 and $\lambda = 610$ nm ramped to maximum intensity in ten optical periods. Main figure shows the kinetic energy of the atomic ion fragments vs time. Note that Coulomb explosion begins near the peak intensity; deceleration of the fragments sets in around 20 optical periods. Inset: Distribution of net electrical charge including both nuclear and electronic components. (Fig. 1 of Ref. [81]) Reprinted figure with permission from M. Brewczyk and K. Rzążewski, Phys. Rev. A **61**, 023412 (2000). Copyright (2000) by the American Physical Society.

field (Fig. 2.3). The variations of ion charge (net charge in a small area around individual atomic cores) and molecule charge (ion charge plus the negative charges enclosed between nuclei) with time show that the number of electrons enclosed in the space between atomic cores increases as the nuclei move apart. There are up to two units of electron charge between atomic cores during the process when the Coulomb explosion is simulated in two-dimensional calculations. The kinetic energy deficit, with respect to the Coulomb explosion at R_e as a result of photo-electron screening, was confirmed at the end of the simulation. Hering *et al.* [82] extended this model to Coulomb explosions of linear triatomic molecules and calculated the

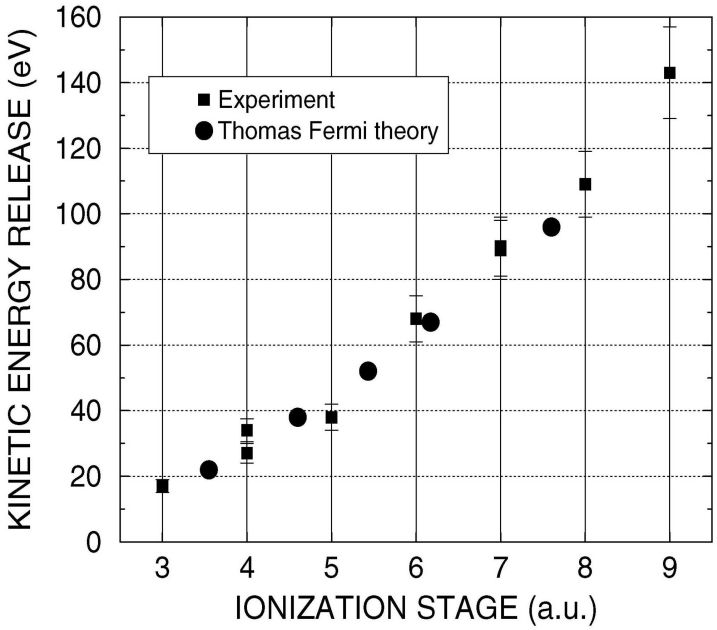

Figure 2.4: Calculated and experimental multifragmentation channels kinetic energy releases vs total number of removed electrons in the Coulomb explosion of CO_2 induced by a linearly polarized laser pulse. (Fig. 1 of Ref. [82]) Reprinted figure with permission from Ph. Hering, M. Brewczyk, and C. Cornaggia, Phys. Rev. Lett. **85**, 2288 (2000). Copyright (2000) by the American Physical Society.

kinetic energies of the ions at the end of the simulations for different charge states. The results were consistent with the experimental data (Fig. 2.4).

Three points in this model need to be examined more carefully. First, the electrostatic potential (mean field) neglects the instantaneous interaction between electrons. For example, the electron-electron scattering is not taken into account. Second, the model treats the electrons as a continuous distribution. When the number of electrons freed through ionization is low, this statistical treatment may not be valid. Third, the calculated kinetic energy of the ions in the simulation (Fig. 2.3) shows a large-amplitude oscillation in time. Whether the final or asymptotic kinetic energy at the end of the simulation is sensitive to the initial or final times and

the stability of the simulation have not been addressed. Meanwhile, the numerical calculation of the dynamics involved in this model is very time-consuming.

2.2 Ejection Anisotropy

As the energy deficit in molecular Coulomb explosion experiments has been widely recognized, it is also well established that the angular distribution of the atomic fragments ejected subsequent to strong-field induced dissociative-ionization is anisotropic. Two effects contribute to the anisotropy, the so-called geometric [13, 86] and dynamic [45, 87] alignment.

Geometric alignment relies on the argument that molecules are preferentially selected along the polarization axis [13, 86] during the ionization process. The laser-induced transition of electrons depends on $\langle \vec{\mu} \cdot \vec{E} \rangle$, where $\vec{\mu}$ is the induced dipole moment and $\vec{E}$ is the laser electric field. Since $\vec{\mu}$ is due to either moving charge from one side of the molecule to the other (charge resonance, dipole transitions [73]) or induced molecular polarizability, it is largest when parallel to the molecular axis. Consequently, $\langle \vec{\mu} \cdot \vec{E} \rangle$ is largest when $\vec{E}$ is parallel to $\vec{\mu}$ that is along the molecular axis and is a function of the *geometric* orientation angle, θ_g, defined as the angle between the polarization and the molecular axes. Thus, molecules with their axes more aligned with the field are easier to ionize leading to an anisotropic angular distribution for the explosion components subsequent to dissociative ionization.

Dynamic alignment refers to the fact that more molecules are torqued to participate in enhanced ionization than would in pure geometric alignment. For sufficiently

long pulses, compared with the molecular rotation period, an induced polarizability can cause dynamic alignment [45, 87] due to the development of pendular states – superpositions of field-free rotational states of the molecules [112, 113]. In short pulses ($\sim$ 100 fs), dynamic alignment is caused by the field exerting a torque on the molecular axis, inducing the molecule to align itself with $\vec{E}$ prior to the Coulomb explosion [36, 42, 96, 97].

Both alignment effects coexist and contribute to the ejection anisotropy in typical Coulomb-explosion experiments performed with linearly polarized light, making them difficult to distinguish. Geometric alignment, or angular dependence of enhanced ionization, has been calculated by the classical field-ionization model [86] and time-dependent Schrödinger equation [96], while simulations by Schmidt *et al.* [37] provide a convincing argument that pulses as short as 130 fs can induce significant dynamic alignment in diatomic systems prior to the Coulomb explosion. Thus far, previous experimental studies have provided qualitative tests for determining when dynamic alignment is active. These tests include varying the polarization [36, 39, 41, 42, 61], wavelength and pulse width of the field [37], laser intensity [37, 39], the moment of inertia of the molecules [41, 42], and the charge state of the constituent atoms [37, 39, 41, 42, 61]. The anisotropy measurement has also been compared with a two-dimensional over-the-barrier ionization calculation [86]. In general, dynamic alignment increases as the moment of inertia decreases and the laser intensity increases, and it is also a function of the ionization charge states [37, 39, 41, 42, 61]. It appears to be clear that dynamic alignment is inactive in I_2 [41, 42, 86] and active in H_2 [86], N_2 [36, 37, 39, 86], O_2 [41, 42] and CO_2 [36, 61].

In a static field, dynamic alignment is characterized by the pendular states [112, 113]. The static field implies two conditions. The first is that the laser pulse width needs to be sufficiently long compared with the molecular rotation period so that the molecules have enough time to fall into pendular states. The second is that the laser frequency needs to be much greater than the reciprocal of the pulse width ($\nu \gg \tau^{-1}$) and it takes many laser cycles for the molecule to be aligned so that the field can be averaged over the pulse duration. Then, the time-independent Hamiltonian for the pendular states in a static field is given by

$$H = B\mathbf{J}^2 - \frac{1}{2}E_0^2\left((\alpha_\parallel - \alpha_\perp)\cos^2\theta_g + \alpha_\perp\right), \tag{2.7}$$

where $\mathbf{J}^2$ is the squared angular momentum operator, $B = \hbar/(4\pi c I_m)$ the rotational constant with I_m as the moment of inertia, E_0 the peak field strength, and $\alpha_\parallel$ ($\alpha_\perp$) the polarizabilty component parallel (perpendicular) to the molecular axis. The interaction potential [113]

$$V_p = -\frac{1}{2}E_0^2\left((\alpha_\parallel - \alpha_\perp)\cos^2\theta_g + \alpha_\perp\right) = -V_\perp - \Delta V\cos^2\theta_g \tag{2.8}$$

is attractive to the point of $\theta_g = 0$ if $\alpha \equiv \alpha_\parallel - \alpha_\perp > 0$. The depth of the potential well is

$$\Delta V = V_\parallel - V_\perp = \frac{E_0^2}{4B}(\alpha_\parallel - \alpha_\perp) = \frac{\alpha E_0^2}{4B}, \tag{2.9}$$

where $V_{\parallel,\perp} = \frac{E_0^2}{4B}\alpha_{\parallel,\perp}$ are the potential energies at parallel and perpendicular directions to the field. The torque that a molecule feels in such a potential well is

$$\mathcal{T} = -\frac{\partial V_p}{\partial\theta_g} = -\Delta V\sin 2\theta_g = -\frac{\alpha E_0^2}{4B}\sin 2\theta_g, \tag{2.10}$$

Table 2.1: Molecular properties for H_2, N_2, O_2, CO_2, NO_2 and I_2. The equilibrium bond length (R_e) and the ground-state rotational constant (B_0) are extracted from experimental measurements [114]. The moment of inertia (I_m) is calculated from the ground-state R_e (The value of NO_2 is calculated at its ground-state bond angle $\theta_{be} = 134^\circ$). The ground-state rotational time is $\tau_e = 1/(2cB_0)$ because the rotational energy at the ground state is $E_0 = h\nu = hcB_0J(J+1)$ with $\nu = 1/\tau_e$ and $J = 1$.

	H_2	N_2	O_2	CO_2	NO_2	I_2
R_e (nm)	0.074	0.110	0.121	0.116	0.119	0.267
I_m ($\times 10^{-40}$ gm cm^2)	0.455	14.0	19.4	71.5	67.2	751
B_0 (cm^{-1})	60.853	1.998	1.438	0.390	0.434	0.0374
τ_e (ps)	0.27	8.35	11.60	42.76	38.43	446

which increases as the laser field or molecular polarizability increases and the rotational constant decreases.

However, the rotation time of small molecules listed in Table 2.1 is on the order of tens of picoseconds or even more except for H_2. The analysis of pendular states may not be valid for the ultrafast dynamics induced by 100 fs laser pulses, at least for the ground states of the molecules. Instead, the pendular potential provides a confinement to the molecules, which will inevitably be ionized once trapped in the potential well. As the depth of the well ($\Delta V \propto \vec{\mu} \cdot \vec{E}/B$) increases, the molecules are trapped more tightly near the ploarization axis.

To understand the torque on the molecular axis exerted by the field of a short pulse, a classical pendulum equation of motion has been solved for the dynamic alignment of a polarized molecule [36, 42, 96, 97]. The torque ($\vec{\mathcal{T}}$) of a dipole moment ($\vec{\mu}$) in an external electric field ($\vec{E}$) has the form of

$$\vec{\mathcal{T}} = \vec{\mu} \times \vec{E}, \qquad \mathcal{T} = \mu E \sin\theta_g, \tag{2.11}$$

where θ_g is the angle between $\vec{\mu}$ and $\vec{E}$. Thus the equation of motion is

$$I_m \ddot{\theta_g} = -\mathcal{T}, \qquad \ddot{\theta_g} = -\frac{\mu E}{I_m} \sin\theta_g, \tag{2.12}$$

where I_m is the moment of inertia of the molecule. Assuming the induced dipole moment is $\mu = \alpha E \cos\theta_g$ and the field takes the time-average value $E = E_0/\sqrt{2}$, Eq. 2.12 becomes

$$\frac{\mathrm{d}^2(2\theta_g)}{\mathrm{d}t^2} = -\frac{E_0^2 \alpha}{2I_m} \sin 2\theta_g. \tag{2.13}$$

At the small-angle limit ($\theta_g \to 0$), the pendular frequency is

$$\omega_p = \sqrt{\frac{E_0^2 \alpha}{2I_m}}. \tag{2.14}$$

For general values of θ_g, Eq. 2.13 can be solved with the *elliptic integral of the first kind* – $K(\sin^2\theta)$ [115] (App. A). The rotation time for the molecule to move from θ_g to parallel to the polarization direction can be expressed as

$$\tau_r = \frac{K(\sin^2\theta_g)}{\omega_p}. \tag{2.15}$$

For $\theta_g < \pi/2$, $K(\sin^2\theta_g)$ is on the order of unity.

At this point, Bandrauk and Ruel [96] assumed $\alpha \sim R^3$, and estimated the rotation time as

$$\tau_r \propto \frac{1}{E_0}\sqrt{\frac{\mu_m}{R}}, \tag{2.16}$$

where, μ_m is the reduced mass with $I_m = \mu_m R^2$ and R is the molecular bond length. However, this relationship between the polarizability and molecular size ($\alpha \sim R^3$) was derived for a hydrogen atom using perturbation theory, and valid mostly for atoms or spherical molecules [105]. For a linear molecule in an intense field, especially one elongated to $R_C \sim 2 - 3 \times R_e$, this may not be valid.

Nevertheless, as shown in the equation of motion (Eq. 2.12), the degree of dynamic alignment should increase as the dipole moment and electric field increase and moment of inertia decreases. Besides, by integrating the equation of motion, one can see that the molecules would be aligned more by spending a longer time in the field.

Chapter 3

APPARATUS

This chapter describes the apparatus used in this study, including the femtosecond laser system, the image spectrometer and vacuum system, digital camera and computer system for data acquisition. The overall experimental setup is shown in Fig. 3.1. Section 3.1 describes the lasers, their operation and beam diagnostics. The characteristics and operation of the image spectrometer and vacuum chamber are described in Sec. 3.2. The digital camera and computer system, which are the foundation of the correlation detection techniques that will be described in the next chapter, are discussed in Sec. 3.3.

3.1 Laser System

The kilohertz femtosecond laser system employed in this study was manufactured by Spectra Physics/Positive Light. The gain medium in both the oscillator and amplifier is Ti:Sapphire (Ti^{3+}:Al_2O_3) crystal, where the Ti^{3+} titanium ion is responsible for the laser radiation. Absorption transitions occur at wavelengths between 400 and 600 nm, while fluorescence transitions exist between 670 and about 1100 nm. Stable and high-output laser emission is available from wavelengths 690 to 1080 nm in the oscillator depending on the optics set [116]. A longitudinal pump is utilized in both the oscillator and amplifier to ensure the pump and cavity modes

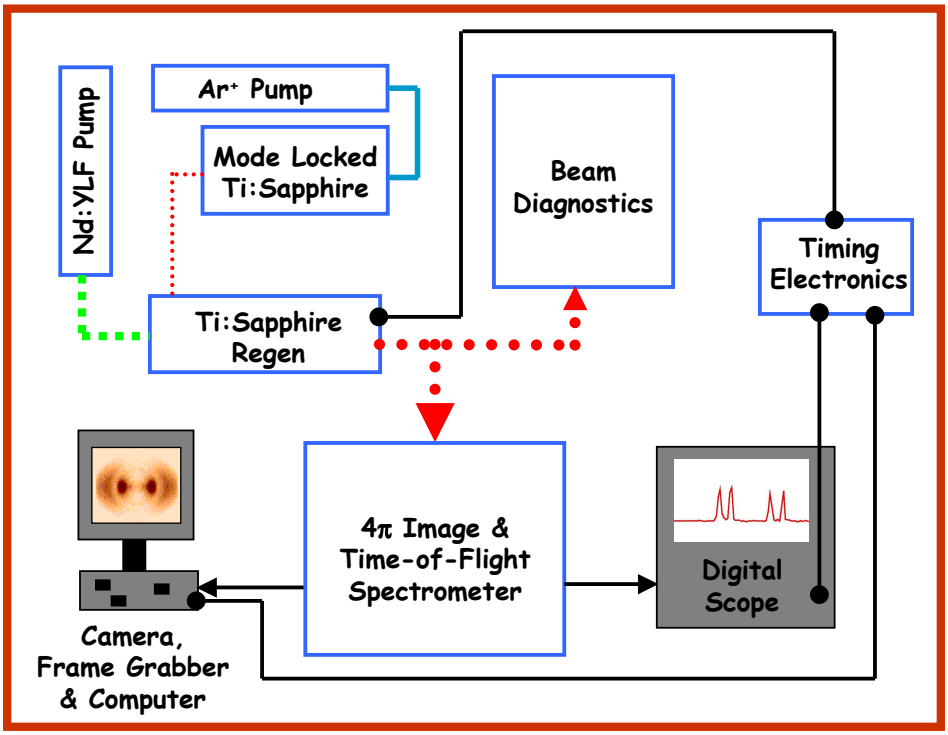

Figure 3.1: The overall experimental setup includes three parts. (1) The 100 fs, 800 nm Ti:sapphire laser system (Spectra Physics/Positive Light) includes a mode-locked Ti:Sapphire oscillator (Tsunami) pumped by an argon ion laser (BeamLok), a Ti:Sapphire regenerative amplifier (Spitfire) with stretcher and compressor pumped by a Nd:YLF laser (Merlin), and beam diagnostics; (2) 4π image and TOF spectrometer housed in a vacuum chamber; (3) digital camera and oscilloscope with computer and timing electronics.

are collinear and overlapped within a long distance inside the Ti:Sapphire rod.

The entire system is composed of four lasers. The mode-locked Ti:Sapphire oscillator (Tsunami, tunable over 735 – 840 nm) is pumped by an All-line continuous-wave (CW) argon ion laser (BeamLok 2060) at 5.5 W. The two most intense emission lines from the argon laser are at 488.0 and 514.5 nm [117]. The average power output of Tsunami is 400 mW with a 76 MHz repetition rate so the energy per pulse is about 5 nJ. The measured pulse width in daily operation is 60 – 80 fs with a 12

nm bandwidth at 800 nm central wavelength. The output pulses from the oscillator are seeded into a chirped-pulse regenerative amplifier (Spitfire including stretcher and compressor) pumped by a Q-switch intracavity doubled Nd:YLF laser (Merlin, 527 nm) at 8 – 10 W. The final output power from the amplifier is as high as 1 W average power at 1 kHz repetition rate and 90 – 120 fs pulse width with 10 nm bandwidth at 800 nm central wavelength.

The mode-locked pulses in Tsunami are sustained by a mechanism called self mode locking, which can be explained by the optical Kerr effect in the laser medium [118]. As a high-intensity Gaussian beam passes through a medium, index refraction of the material is changed by the nonlinear effect according to $n(r) = n_0 + n_2 I(r)$, where r is the radial distance on the wavefront, I is the intensity, n_0 and n_2 are the linear and 2nd order nonlinear index refraction. In a Gaussian beam, I drops as r increases so that $n(r)$ also decreases and the medium will act as a positive lens to make the beam size smaller. This is known as self-focusing. The mode-locked beam has a higher intensity than the CW mode with the same average power in the cavity so that it has a tighter waist in the laser medium. As the oscillator is longitudinally pumped by another laser beam, the spatial gain profile created by the Gaussian shape of the pump beam acts like a soft aperture which gives the tighter mode-locked cavity mode higher gain, or more loss for the CW mode [119]. Thus, the mode-locked beam is favored over the CW mode by the optical Kerr effect and a stable pulse train is sustained. At the same time, the width of the mode-locked pulse is broadened every time it travels through the laser medium. The positive group-velocity dispersion (GVD) or chirp is a combination of the second derivative of the

linear index refraction with respect to the wavelength ($d^2n_0/d\lambda^2$) and self phase modulation by the nonlinear effect in the laser medium – $n(t) = n_0 + n_2 I(t)$, where t is time. In order to generate short pulses close to the transform-limit, negative GVD is introduced by a four-prism sequence to compensate the positive GVD in the laser rod [12, 116, 120, 121].

In order to obtain high peak power, the oscillator pulses need to be amplified. For short pulse amplification, three issues have to be addressed in the design of the amplifier, a broad bandwidth to support the full spectrum of the short pulse, a near-saturation fluence in the medium to extract the energy as much as possible, and a low intensity to prevent material damage and nonlinear effect distorting the spacial and temporal profiles of the pulses. While the first requirement is fulfilled by the large gain-bandwidth of the Ti:Sapphire crystal itself, the other two are accomplished by the chirped pulse amplification (CPA) [122]. The short pulses (80 fs) from the oscillator are first stretched to 100 – 200 ps by a folded diffraction grating stretcher, which disperses different frequencies and causes the higher frequency components to travel longer distances through the stretcher than lower frequency components. The dispersion is positive and linear. The low peak power pulses are then amplified in a regenerative amplifier cavity by a factor of about 10^6 in about 20 round trips. After the amplified pulse exits the cavity, a grating compressor reverses the process in the stretcher to remove the positive chirp introduced by the stretcher as well as the extra linear dispersion introduced by the amplifier cavity. The pulse width is compressed back to about 100 fs and the final power can be as high as 10 GW (1 mJ/100 fs) [123].

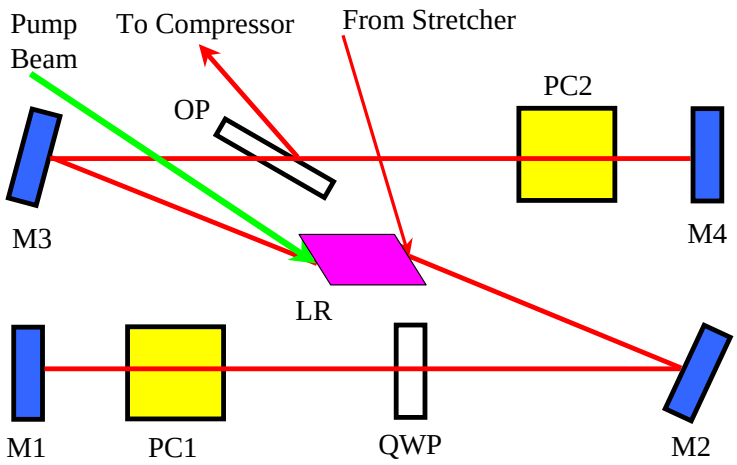

Figure 3.2: Cavity of the regenerative amplifier. M1 – M4 are broadband dielectric mirrors, LR is the Ti:Sapphire laser rod, PC1 and PC2 are the input and output Pockels cells, QWP is the quarter wave plate, and OP is the thin film polarizer.

The schematic of the regenerative amplifier cavity in Spitfire is shown in Fig. 3.2. The pulse from the stretcher is reflected into the cavity on the right surface of the laser rod. If both Pockels cells are off, the pulse makes a round trip in the cavity and is reflected out by the thin film polarizer (OP). When a pulse is selected to be amplified, the input Pockels cell (PC1) is activated by a quarter-wave voltage (typically 3500 volts) after the pulse passes it the first time. As the incident angle on the surface of the laser rod is close to the Brewster angle, the reflected pulse has a vertical polarization. After it is reflected by M1 and goes through PC1 (not activated yet) and the quarter-wave plate twice, the polarization is rotated to be horizontal. When the pulse travels through the rest of the cavity and comes back, PC1 has been activated and acts like a quarter-wave plate, which cancels the polarization rotation invoked by the real quarter-wave plate. The polarization of the pulse stays horizontal and the pulse is trapped in the cavity and amplified. After about 20 round

trips, the output Pockels cell (PC2) is activated also by a quarter-wave voltage. As the now amplified pulse double-passes PC2, the polarization is rotated to be vertical and the pulse is reflected out of the cavity by the output polarizer (OP) [123]. The polarization of the pulse and voltages on the Pockels cells at each optical element in the amplifier cavity are listed in Table 3.1. The activation of the Pockels cells in middle and lower tables is labeled right before the pulse arrives. In practice, they can be activated any time before the pulse arrives and after the pulse leaves the last time. The electronic controller of the Pockels cells is synchronized with the oscillator. The Pockels cells are activated and deactivated at the right times so that one and only one pulse is allowed to circulate in the cavity at a time and only up to 1000 pulses are selected out of the 76 million from the oscillator in each second.

Several important characteristics of the amplified pulse have been determined in the experiments. They are pulse width, power stability, and beam divergence.

The pulse width of Tsunami and Spitfire can be measured by a home-built single-shot autocorrelater. The schematic is shown in Fig. 3.3. The pulse from the laser is split into two identical copies by the beamsplitter. One is reflected by the mirrors M3, M5 and M6, and the other by M1, M2, M4 and M6. The two pulses cross each other at the BBO crystal with a small angle (about 7°). The optical paths in the two arms are set to be the same so that the two pulses arrive at the BBO crystal at the same time to generate second harmonic signal, which bisects the angle between the two original beams and detected by a CCD (Charge-Coupled Device) camera. Mirrors M1 and M2 are mounted on a translation stage so that the relative delay between the two pulses can be adjusted.

Table 3.1: Polarization (POL) of the pulse and voltages on the Pockels cells (PC1 and PC2) at each optical element in the amplifier cavity. The labels of the elements are the same as in Fig. 3.2. The polarization states and the voltages (0 or $\lambda/4$ voltage) are the ones AFTER the pulse passes through the element. The pulse is running from left to right. The upper table is the trip with both Pockels cells off. It starts as the pulse is reflected into the cavity by the right surface of the laser rod (Fig. 3.2). At the end, the vertically polarized pulse is reflected out by the thin film polarizer (OP). The middle table is the trip when the pulse is trapped. It also starts as the pulse is reflected into the cavity by the laser rod. After this trip, the pulse stays in the cavity as PC1 stays activated. The lower table is the last round trip a pulse makes in the cavity. It starts as the pulse goes through the laser rod toward the quarter-wave plate. At the end, the amplified pulse is ejected out by the thin film polarizer. Two mirrors (M2 and M3) are omitted since they do not affect the polarization of the pulse.

	start	QWP	PC1	M1	PC1	QWP	LR	OP	PC2	M4	PC2	OP	LR	QWP	PC1	M1	PC1	QWP
POL	⇳	↺	↺	↻	↻	⇔	⇔	⇔	⇔	⇔	⇔	⇔	⇔	↻	↻	↺	↺	⇳
PC1	0	0	0	0	0	0	0	0	0	0	0	0	0	0	0	0	0	0
PC2	0	0	0	0	0	0	0	0	0	0	0	0	0	0	0	0	0	0

	LR	OP	PC2	M4	PC2	OP
POL	⇳	⇳	⇳	⇳	⇳	⇳
PC1	0	0	0	0	0	0
PC2	0	0	0	0	0	0

	start	QWP	PC1	M1	PC1	QWP	LR	OP	PC2	M4	PC2	OP	LR	QWP	PC1	M1	PC1	QWP
POL	⇳	↺	↺	↻	↻	⇔	⇔	⇔	⇔	⇔	⇔	⇔	⇔	↻	⇳	⇳	↻	⇔
PC1	0	0	0	0	0	0	0	0	0	0	0	0	0	$\lambda/4$	$\lambda/4$	$\lambda/4$	$\lambda/4$	$\lambda/4$
PC2	0	0	0	0	0	0	0	0	0	0	0	0	0	0	0	0	0	0

	start	QWP	PC1	M1	PC1	QWP	LR	OP	PC2	M4	PC2	OP	LR	QWP	PC1	M1	PC1	QWP
POL	⇔	↻	⇳	⇳	↻	⇔	⇔	⇔	↻	↺	⇳	⇳						
PC1	$\lambda/4$	$\lambda/4$	$\lambda/4$	$\lambda/4$	$\lambda/4$	$\lambda/4$	$\lambda/4$	$\lambda/4$	$\lambda/4$	$\lambda/4$	$\lambda/4$	$\lambda/4$						
PC2	0	0	0	0	0	0	0	$\lambda/4$	$\lambda/4$	$\lambda/4$	$\lambda/4$	$\lambda/4$						

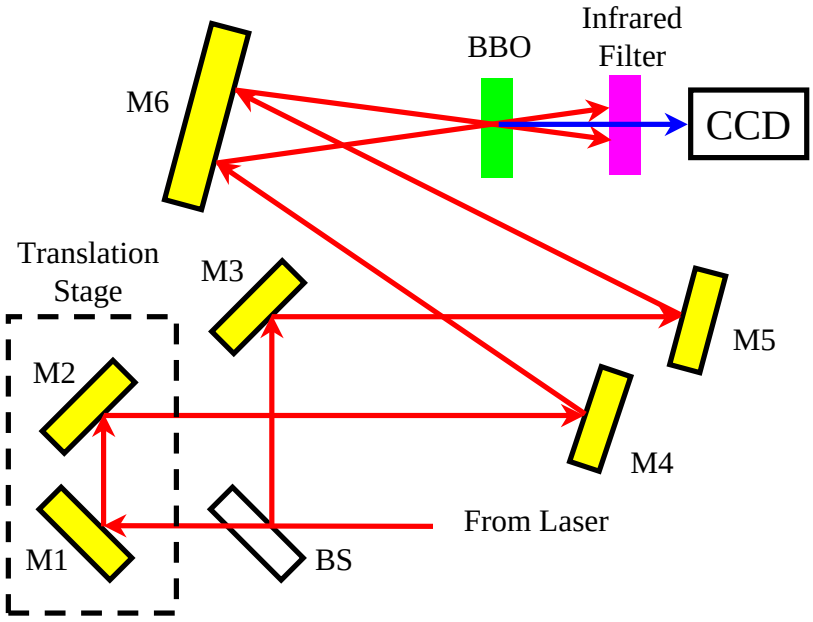

Figure 3.3: Schematic of a single-shot second-harmonic autocorrelater. Mirrors M1 and M2 are gold-coated broadband, while mirrors M3 – M6 are aluminum-coated broadband. BS is 50-50 beamsplitter. The distance that the translation stage moves is measured by a micrometer with an accuracy of 20 μm. BBO (beta barium borate) is the doubling-frequency crystal. All the reflected beams are kept in the same plane, and both pulses arrive at the crystal with the same incident angle. The second harmonic signal bisects the angle between the two fundamental beams and detected by a CCD camera. The transmitted fundamental beams are filtered out by the infrared filter (Schott BG series, more than 70% transmission at 400 nm and less than 1% at 800 nm). The crystal is mounted on a rotary holder in order to be rotated to get phase-match when the polarization of the incident beam changes.

The principle of a single-shot autocorrelater is to transform the temporal profile of the pulse into a spatial signal, which can be detected easily with a CCD array or camera [124]. This transformation is realized by the second harmonic (SH) generation in the BBO crystal (Fig. 3.4). The SH signal is only present when the two pulses overlap both spatially and temporally; its spatial profile can be expressed as $\mathrm{SH}(x) \propto \int_{-\infty}^{\infty} I(t+\delta t)I(t-\delta t)\mathrm{d}t$, where $2\delta t$ is the time delay between the two pulses as a function of position x (Fig. 3.4). The FWHM (D) of the SH(x) signal can

be measured with the CCD camera. It is proportional to the autocorrelation pulse width τ_{auto}. In order to obtain the coefficient between D and τ_{auto}, the autocorrelater needs to be calibrated by changing the delay between the two pulses. This can be done by moving the translation stage. When the stage is moved by a distance Δ, the optical paths in the two arms differ by 2Δ. Thus the delay time is 2Δ/c, where c is the speed of light. The SH signal also moves along the x direction accordingly, and the shift d corresponds to 2Δ/c. Then the autocorrelation pulse width can be calculated as $\tau_{auto} = 2\Delta \cdot D/(c \cdot d)$. It is not possible to retrieve the pulse shape $I(t)$ from SH(x) or pulse width τ from τ_{auto} directly because SH(x) is an integral convolution of $I(t)$. However, since the function of $I(t)$ is normally well defined by the characteristics of the laser system, the ratio between τ and τ_{auto} is easily obtained. For Ti:Sapphire oscillator and amplifier, the pulse shape is a hyperbolic secant squared function [116] so that

$$\tau = \frac{\tau_{auto}}{1.55} = \frac{2\Delta \cdot D}{1.55c \cdot d}. \tag{3.1}$$

The pulse width of the oscillator is measured to be 60 to 80 fs, while that for the amplified pulse is 90 to 120 fs.

The long-term stability of the average power from Spitfire was monitored by a Scientech power meter. In daily operation, the variation of the average power within 4 – 8 hours after the whole system is warmed up, which takes up to 3 hours, is less than 3%, and normally no more than 5%. The short-term energy variation is determined by a photodiode. After the pulse is focused by a concave mirror inside the vacuum chamber, it diverges very quickly and part of the beam goes out of the

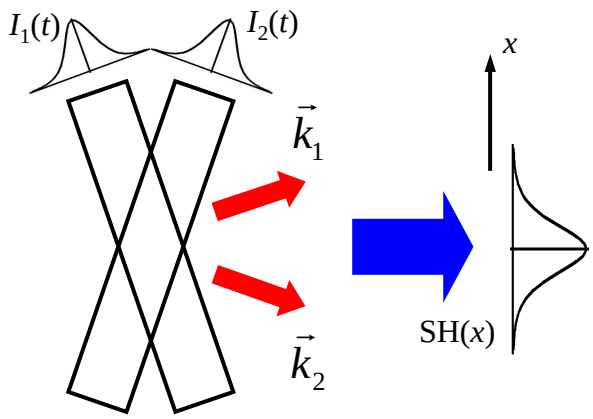

Figure 3.4: Second harmonic (SH) generation in the BBO crystal. This plot is in the same plane as in Fig. 3.3. The SH signal is only generated where the two pulses overlap both spatially and temporally. The fundamental pulses propagate in the directions of $\vec{k_1}$ and $\vec{k_2}$. Their temporal profiles are $I_1(t)$ and $I_2(t)$ with $I_1(t) = I_2(t) = I(t)$. The SH signal from the overlap of the pulses is SH(x), where x direction is parallel to the face of the crystal.

chamber through the viewport. A photodiode is located outside of the viewport to detect it. Since the beam is diverging, the input intensity on the photodiode decreases as it is moved away from the viewport. The location of the phototdiode is set so that the intensity is low enough for the photodiode to operate in linear range. The signal from the photodiode is collected by a digital oscilloscope (LeCroy 9350AM) and the waveforms of roughly every 15,000 pulses (15 seconds), which fit onto a floppy disk, are transfered to a computer to be analyzed. The peak amplitude of the signal on the photodiode is assumed to represent the peak intensity of the laser pulse. The standard deviation of the signals for 15,000 pulses is about 10 – 20% (Fig. 3.5).

The divergence of the amplified pulse was determined by measuring the smallest spot size after the beam was focused by a concave mirror and comparing the

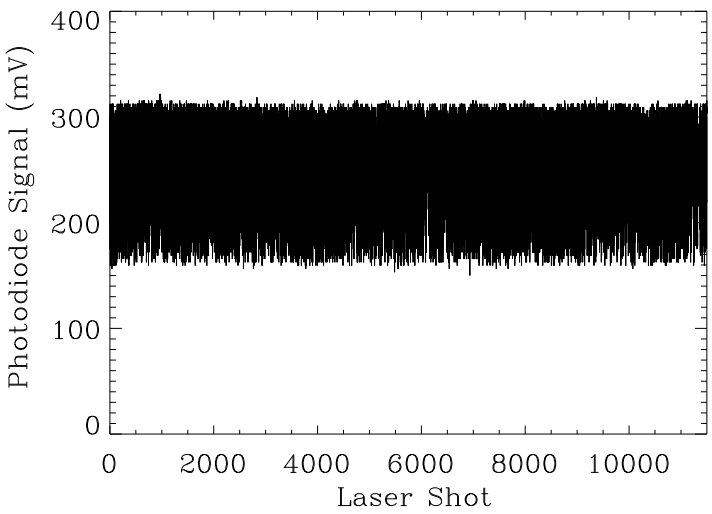

Figure 3.5: Measured variation of the peak amplitude of the signal on the photodiode, which is assumed to represent the peak intensity of the laser pulse. The photodiode is connected to the digital oscilloscope (LeCroy 9350AM) with 50 Ω impedance. In this particular run, 13,000 laser pulses were recorded and the standard deviation of the signal is 18%.

result to theory. For a focused Gaussian beam at the diffraction limit, assuming the incident beam diameter is πw_m that contains 99% of the total energy, the waist at the focal point is [12]

$$w_f^{DL} = \frac{f\lambda}{\pi w_m}, \tag{3.2}$$

where f is the focal length, λ the wavelength, and w_m the beam waist at the lens or concave mirror. After being reflected by three uncoated windows (roughly 4% reflectivity each, to reduce the beam intensity) and two aluminum mirrors, the pulse from Spitfire was focused by a 3-meter concave spherical aluminum mirror ($f = 1.5$ m). A CCD camera was set at the focal point with a few neutral density filters to reduce the beam intensity further so as not to damage or saturate the camera. The minimum size of the focused beam was found at 1.6 m away from the mirror

by moving the camera along the propagation direction. The radius from the center of the beam to where the intensity drops to $1/e$ of the peak value was 18 camera pixels in the horizontal direction. The pixel size of the camera in this direction is 8.4 μm, so r = 151 μm. Since the intensity of a Gaussian beam drops to $1/e$ at $r = w/\sqrt{2}$ (i.e. w defined as $1/e^2$ point of the intensity), the waist of the focused beam is $w_f = \sqrt{2}r \approx 210$ μm. As the camera was placed in front of the concave mirror, the unfocused beam size was bigger than the CCD and only a portion of the beam was detected by the camera. Fortunately, this portion was larger than a half of the beam, so the radius at the $1/e$ point could still be measured as roughly 450 pixels. Thus, the unfocused beam size at the mirror was $w_m = \sqrt{2} \times 450 \times$ 8.4 μm $\approx$ 5.3 mm. According to Eq. 3.2, the beam size at diffraction limit should be w_f^{DL} = 72 μm with f = 1.5 m, λ = 800 nm, and w_m = 5.3 mm. Thus, the divergence of the beam was about three times ($\mathscr{R} = w_f/w_f^{DL} \approx 3$) the diffraction limit. Since the relative divergence ($\mathscr{R}$) is proportional to $1/f$ (Eq. 3.2), the uncertainty ($\frac{\Delta\mathscr{R}}{\mathscr{R}}$) is also proportional to the uncertainty of the focal length. A 10% uncertainty of f would cause a 10% uncertainty of $\mathscr{R}$.

3.2 Image Spectrometer and Vacuum System

The spectrometer (Fig. 3.6) used to study strong-field dissociative ionization of molecular gases consists of an image and a TOF detector [22, 100], allowing images and TOF waveforms to be obtained from the same focal point by reversing the electric field used to sweep the ions to the detectors. The image detector, which

is able to collect all ions ejected into 4π sr simultaneously, consists of a region of space with a uniform static electric field and an image quality microchannel plate (MCP) with a phosphor screen at its back end. The potential and spacing between the electrode rings are set as shown in Fig. 3.6 in order to generate the uniform static field between the image MCP and the flight tube. The typical static field ($\sim$ 260 volts/cm) leads to a maximum detectable energy of doubly charged ions as about 95 eV. The MCP has a diameter of 50 mm with a 40-mm active area to detect charges. Laser pulses are brought to focus at a distance l from the center of the MCP. Charges ($\pm qe$) are swept toward the MCP by the static electric field after they are ejected from the focal point. Upon striking the surface of the MCP, the ions generate electrons that are amplified in the MCP and then converted to light by the phosphor screen. The light is digitized by a digital CCD camera and recorded to disk in real time at up to 735 Hz. The camera frame rate is synchronized with the laser repetition rate so that each captured frame corresponds to one laser pulse. The camera exposure time and the MCP/phosphor gain are adjusted to produce a zero background while allowing near single-charge detection. The center of mass of the ejection dynamics coincides with the lab frame with its origin at the center of the image. The TOF detector (Fig. 3.6) consists of an acceleration region (the same static electric field as in the image detector between ER_3 and ER_4), a field-free drift region (inside the flight tube), a second acceleration region just prior to an MCP, while a digital oscilloscope (LeCroy 9350AM), also synchronized with laser repetition rate, is used to capture and analyze the waveforms.

The spectrometer is housed in an ultra-high vacuum chamber constructed

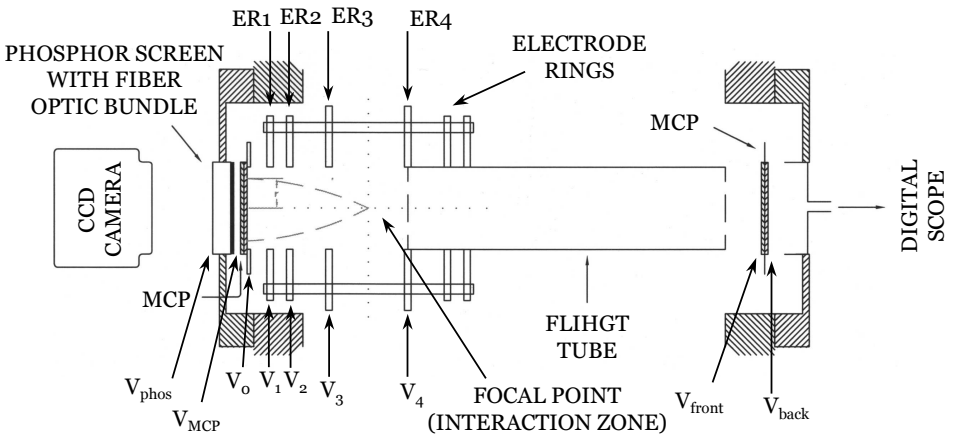

Figure 3.6: Structure of the image-TOF spectrometer. There are six electrode rings in the spectrometer. The two close to the TOF detector are not being used. The other four (ER_1 to ER_4) are used to generate a static electric field between the image MCP and the flight tube. Their inner diameters are 40 mm to match the size of the active area of the image MCP. The voltages on the electrodes are $V_4 = 2V_3 = 4V_2 = 8V_1$. Positive or negative voltages (normally 2000 volts) are applied to take ion images or TOF waveforms, separately. The front side of the image MCP is grounded ($V_0 = 0$). The distances between the electrodes and MCP are $D_4 = 2D_3 = 4D_2 = 8D_1 = 76.2$ mm (3 inches) to ensure a uniform field. The focal point of the pulse is between ER_3 and ER_4 so that the distance between the interaction zone and MCP is $l = 3D_4/4 = 57.15$ mm and the potential $V_{int} = 3V_4/4$. The potential across MCP V_{MCP} is up to 2000 volts. The front side of the phosphor screen is connected to the back of MCP, while the potential between the back side and the ground is $V_{phos} =$ 4800 volts. The voltages on the front and back sides of the TOF MCP are V_{front} $= -2300$ volts and $V_{back} = -300$ volts. The 140-mm-long flight tube is connected with ER_4 on one end and the other end is 30 mm away from the front side of the TOF MCP. The diameter of the tube is 40 mm and there is no field in the tube.

from non-magnetic stainless steel with a base pressure of about 4×10^{-10} Torr and pumped by a turbo molecular pump. The turbo pump is a Pfeifer TMH 260 with a TCP 380 pump controller and its pumping speed is 260 liters/s at 1000 Hz. The turbo pump is backed by a Sargent-Welch 1398 mechanical vacuum pump to keep the pressure in the fore line below 50 mTorr. To perform experiments, gas is introduced into the chambers through a high-precision leak valve (Granville-

Phillips 216 with pressure control ranging from 10^{-11} to 1300 Torr and conductance to vacuum of 10^{-12} liters/s[1]). Typically, experiments are run at pressures between 10^{-9} and 6×10^{-8} Torr to minimize space charge effects.

Laser pulses are introduced into the chamber through a fused-silica viewport at normal incidence. The beam is focused with a spherical mirror (38 mm diameter, 75 mm focal length) mounted inside the chamber and its intensity was determined as the following. In principle, the intensity of a focused Gaussian beam at the diffraction limit is given by

$$I = \frac{P}{2(f\#\lambda)^2}, \tag{3.3}$$

where $f\#\lambda = f\lambda/(\pi w_m) = w_f^{DL}$ (Eq. 3.2) and P is the laser power [12]. For a pulsed laser with an average power P_{avg} at a repetition rate f_{rep} and a pulse width τ, the power of the pulse is $P = P_{avg} \cdot \mathscr{T}/(\tau f_{rep})$, where $\mathscr{T}$ is the power transmission from the laser to the focal point. Thus, the intensity is

$$I = \frac{P_{avg}\mathscr{T}}{2w_f^2 \tau f_{rep}}, \tag{3.4}$$

where the real beam size w_f is used instead of w_f^{DL}. In our system, the unfocused beam size before the concave mirror in the spectrometer is estimated as $w_m = 8$ mm so that the focused beam size at the diffraction limit is $w_f^{DL} = 2.4$ μm with $f = 75$ mm and $\lambda = 800$ nm (Eq. 3.2). Since the divergence of the beam is about three times the diffraction limit (Page 42), the real beam size at the focal point is $w_f = 3 \times w_f^{DL} = 7.2$ μm. For Spitfire, with $P_{avg} = 0.5$ W, $f_{rep} = 1000$ Hz, $\tau = 100$ fs and

[1]Conductance (C) is the flux or throughput (Q) of the gas divided by the pressure difference between the inlet (P_1) and outlet (P_2) of the segment, $C = Q/(P_1 - P_2)$, and measures how well the gas can go through a component of the vacuum system (valve, orifice, etc.). The unit dimensions of C and Q are volume/time and pressure·volume/time.

$\mathscr{T} = 74\%$ (80% from the output of the compressor in Spitfire to the input viewport of the vacuum chamber and estimated 8% loss at the viewport), the intensity at the interaction zone of the spectrometer is 3.7×10^{15} W/cm^2.

This calculation was checked with the measurement of the ion appearance intensities of noble gases, for example, xenon. The TOF spectra of xenon ions generated by the laser radiation with linear polarization were taken under a series of average laser powers. Higher charged xenon ions appear one by one as the laser power increases. The appearance intensity of a certain charge state was calculated by Eq. 3.4 from the lowest average power where xenon ions with this charge state were found in the TOF spectrum. The values of the appearance intensities of Xe^{3+}, Xe^{4+} and Xe^{5+} were measured as 4.4, 7.1 and 12×10^{14} W/cm^2 (Fig. 3.7). These values were found to be consistent with the appearance intensities determined in a previous study (4, 9 and 14×10^{14} W/cm^2) [106] with a difference of only about 15%.

Typically, an experiment is composed of capturing 100,000 to 500,000 camera frames or 1,000 to 10,000 TOF waveforms generated by 100 fs laser pulses focused to intensities between 10^{14} and 10^{16} W/cm^2. Figs. 3.8 and 3.9 show samples of TOF and image spectra, respectively. Each laser pulse produces tens of ions in a variety of charge and energy states. For molecular systems, a significant number of near-zero energy ions are generated with each pulse. These ions, molecular and atomic, collect at the center of the image. Since an ion's trajectory depends only on its charge and initial kinetic energy (see App. B.1), ions with different masses but with the same kinetic energy and angular distribution will collect at the same place on the image. To study simple spectra such as single-component photo-electron distributions or

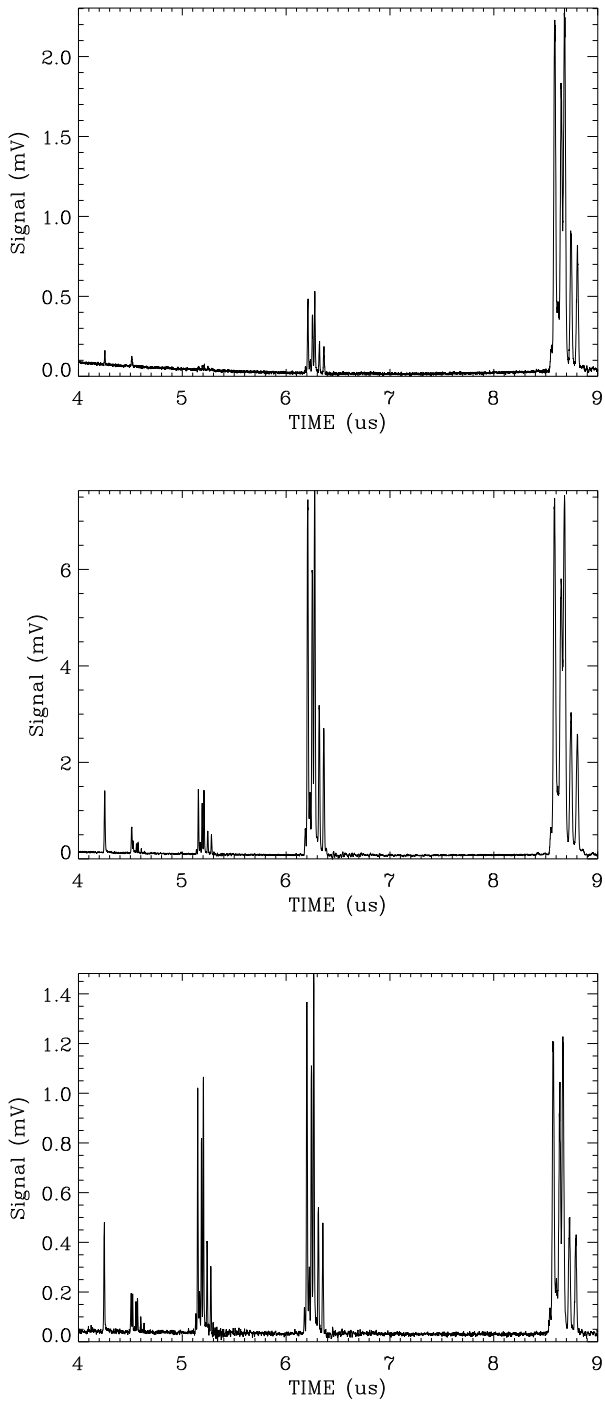

Figure 3.7: TOF spectra of Xe at laser intensities of 4.4 (top), 7.1 (middle) and 12×10^{14} W/cm^2 (bottom) calculated by Eq. 3.4. The ions are Xe^+ (8.6μs), Xe^{2+} (6.3μs), Xe^{3+} (5.2μs), Xe^{4+} (4.6μs) and Xe^{5+} (4.1μs). The sharp single peaks at 4.2 and 4.5μs are N_2^+ and O_2^+ from the background. The signal of Xe^{3+} (Xe^{4+}, Xe^{5+}) can be barely seen in the top (middle, bottom) plot.

the two-component proton distribution of H_2 dissociative-ionization, this is not a major issue. However, for systems with multiple explosion channels (such as N_2, O_2, NO_2 or CO_2), there can be great confusion from overlapping spectra of the various atomic and molecular ions. To reduce this confusion, the fact that ions with different masses and at different charge states arrive at the image detector at different times is exploited to gate the potential across the MCP [100]. The potential (V_{MCP}) is only brought up to 2000 volts when the interested ions arrive at the MCP, and is kept at 1000 volts otherwise so that electron amplification does not occur in the MCP. We note that, since only V_{MCP} is changed and V_0 stays fixed (Fig. 3.6) when the MCP is gated, the static field in the interaction region is not affected. At the same time, although the potential across the phosphor screen ($V_{phos} - V_{MCP}$) is higher when V_{MCP} is kept low than when V_{MCP} is brought up, no ion images appear on the screen since electron amplification does not occur in the MCP when V_{MCP} is kept low.

Using the structure of the spectrometer and potentials on the electrodes (Fig. 3.6), it is possible to calculate when and where an ejected ion will strike either the image or TOF MCP. Arrival time for an ion with zero initial momentum or ejected parallel to the MCP to fly from the interaction zone to the image detector is given by

$$t = \sqrt{\frac{2ml}{qeE}} = l\sqrt{\frac{2m}{qeV_{int}}}, \tag{3.5}$$

where m and qe are the mass and charge of the ion, l and V_{int} are the distance and potential between the focal point and the detector (Fig. 3.6), and $E = V_{int}/l$

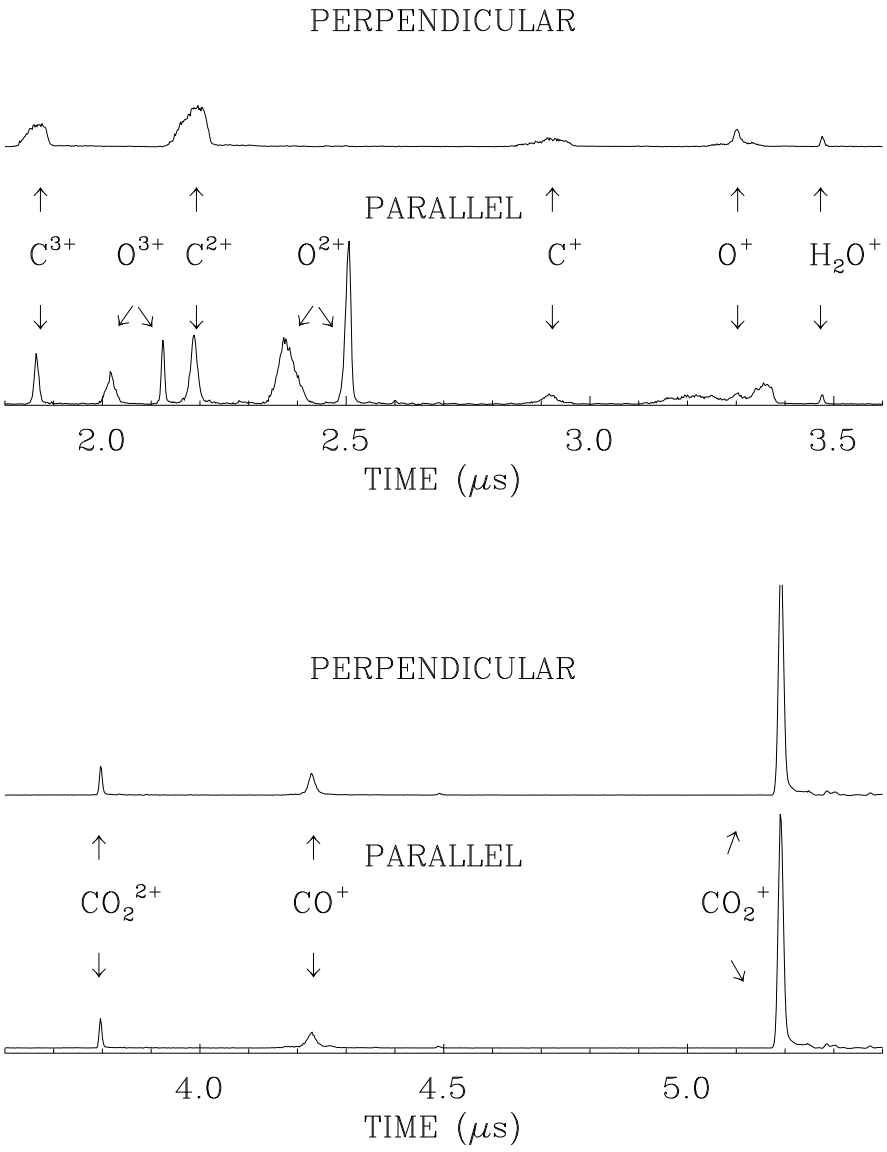

Figure 3.8: TOF waveforms resulting from CO_2 Coulomb explosions obtained with 100 fs pulses focused to 2×10^{15} W/cm^2 when the polarization axis is parallel and perpendicular to the TOF axis. The upper traces are rescaled by a factor of two. Note, the C structure is different in the parallel and perpendicular traces while some O components are missing altogether from the perpendicular trace. Each trace is an average of 1000 laser shots.

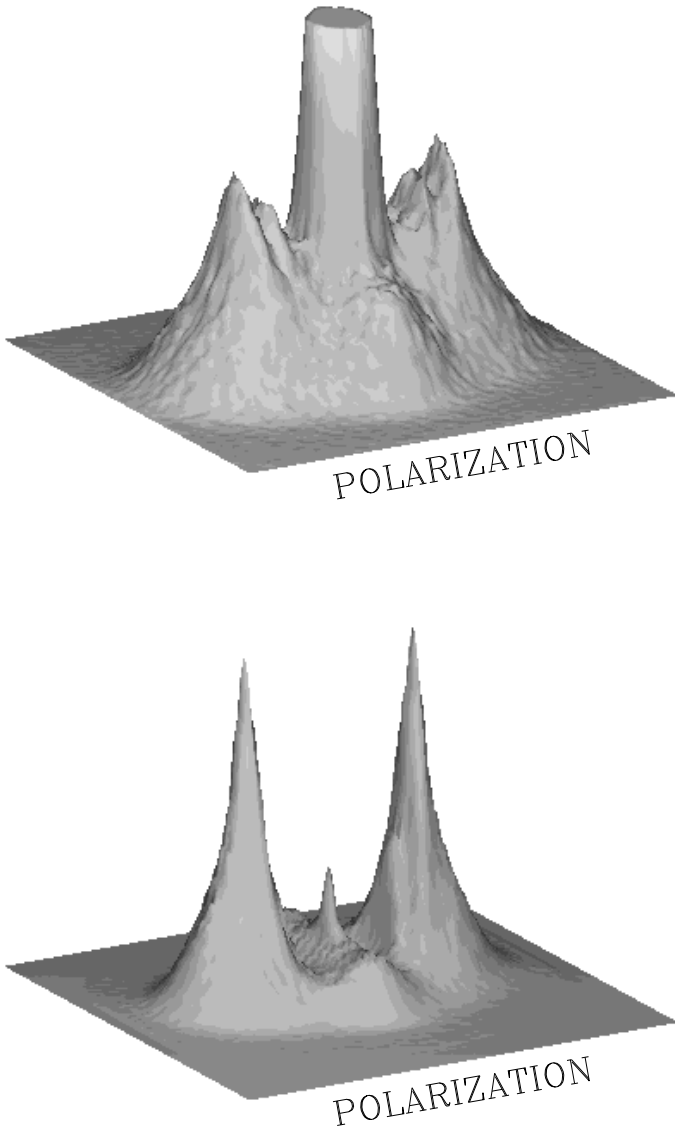

Figure 3.9: Surface plots of ion images resulting from NO_2 Coulomb explosions obtained with linearly polarized 100 fs pulses focused to 2×10^{15} W/cm^2 when the polarization axis is parallel to the image MCP. The upper plot was taken with no gate on the MCP, all the molecular and atomic ions were collected; the large peak at the center was formed by near zero-energy ions, the top of which had to be truncated in order to show other structures on the image. The lower plot was taken while the MCP was gated; only doubly- and triply-charged atomic ions were collected. Each plot is an average of 500,000 laser shots.

Table 3.2: Arrival time in the unit of ns for atomic and molecular ions which have zero initial momentum or are ejected parallel to the image MCP calculated by Eq. 3.5 with $V_{int} = 1500$ volts. The charge states marked as N/A either does not exist or is never detected. The arrival time for an electron is 5 ns.

	+1	+2	+3
H	212	N/A	N/A
H_2	300	N/A	N/A
C	736	520	425
N	795	562	459
O	850	601	491
OH	876	N/A	N/A
H_2O	901	N/A	N/A
N_2/CO	1124	795	N/A
NO	1163	823	N/A
O_2	1202	850	N/A
CO_2	1409	996	N/A
NO_2	1441	1019	N/A

is the static field strength. Table 3.2 lists the arrival times for relevant atomic and molecular ions. The ions with nonzero momentum will arrive earlier or later and this table only serves as a guideline for setting up the MCP gate to detect a particular ion. Detailed calculations for nonzero-momentum ions as well as the flight time to TOF MCP are given in Appendix B. Typically, gate widths of a few hundred nanoseconds are sufficient to isolate the first few atomic charge states. Figure 3.10 displays a series of gated images for the dissociative ionization of NO_2 at 2×10^{15} W/cm^2, and shows clearly that ions with different masses and charges arrive at the MCP at different times. Details of the image spectrum will be discussed in the next chapter.

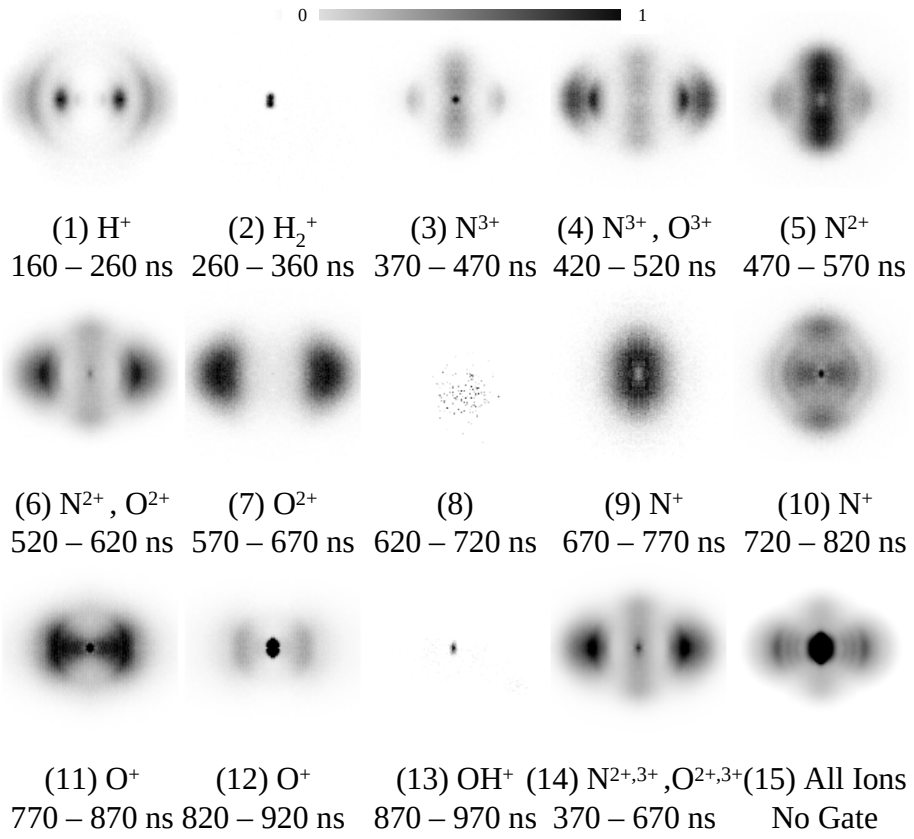

Figure 3.10: Gated images of the dissociative-ionization spectrum of NO_2 generated with 100 fs, 2×10^{15} W/cm^2 pulses. The times under each image indicate when the MCP gate opens and closes and are relative to the arrival time of the laser pulse to the focal point. Images (1) – (13) were taken under the same conditions (gas pressure, laser intensity and gate width), but have been re-scaled relative to (6) by the following factors: (1) 1.7×, (2) 10×, (3) 4.3×, (4) 4.3×, (5) 3×, (6) 1×, (7) 6×, (8) 95×, (9) 10×, (10) 4.3×, (11) 1.5×, (12) 1.5× and (13) 19×. Few ions were detected in image (8). Image (14) is a composite image of all the doubly and triply charged atomic ions (i.e., N^{2+}, O^{2+}, N^{3+} and O^{3+}, same as the lower plot in Fig. 3.9) and image (15) is the composite image taken with no gate (same as the upper plot in Fig. 3.9).

3.3 Digital Camera for Imaging

The system for image acquisition is composed of a high frame-rate digital CCD camera, a frame grabber, a computer and a digital delay generator (DDG). The digital camera is a Dalsa model CA-D1 with 128×128 pixels, up to 735 frame-per-second acquisition rate, and a standard C-mount lens adapter. The pixels of the CCD sensor are squares with a 16-μm^2 size. The intensity output is 8-bit digital. The value runs from 0 to 255 (2^8-1), and the noise (random noise and fixed pattern noise) is no greater than 3 [125]. In the test runs of the camera without the laser, there are 1% of the pixels with a value of 0, 78% with a value of 1, 21% with a value of 2, and only 5 pixels with a value of 3, out of 3.3×10^9 pixels (total 200,000 frames). Therefore, the threshold for the frames is set at 3. Any pixel with a value lower than 3 is treated as background and set to be zero. The Bitflow Road Runner frame grabber transfers the captured frames from the camera to a computer with an 800-Hz Pentium III CPU. The frames are stored directly onto an external SCSI drive attached to the computer to keep up with the high frame rate of the camera. Two 160-GB (gigabytes) SCSI drives can store up to 10 million frames each. The Video Savant software is run under the Windows NT operating system to control the frame grabber and the digital camera. Some sample frames taken by the camera are shown in Fig. 4.1.

A trigger signal at the laser repetition rate from the Spitfire controller is fed to the digital delay generator (DG535, Stanford Research Systems, Inc.). Two of its output channels are used to form a square wave to trigger a GRX high-voltage

pulse generator (Directed Energy, Inc.) to gate the MCP. The high-voltage pulse generator takes two high-voltage inputs (V_+ and V_-) and forms a square wave following the trigger signal from the DDG. In our case, V_+ = 2000 volts and V_- = 1000 volts. The timing relative to the laser pulse and the width of the gate are controlled by varying the delays on the DDG channels to detect ions with different charge and mass. A third channel with a 50-μs fixed delay synchronizes the digital camera. Since the maximum frame rate of the camera is 735 Hz, the laser is set to run at 500 Hz instead of 1000 Hz for the camera to keep up. Even at this rate, a half million frames (a typical experiment) can be taken within 20 minutes.

Chapter 4

CORRELATION DETECTION

Correlation detection employed in this study is a type of statistical approach to identify the ions ejected from the same explosion event so that the pre-explosion geometry of the parent molecule or molecular ion can be determined. In order to apply correlation detection, three requirements have to be met by the spectrometer and data acquisition device. The first requirement is simultaneous collection of all explosion partners ejected into 4π sr, which is fulfilled by the image spectrometer described in Sec. 3.2. The second and third are that each single frame contains ejected ions from one and only one laser pulse and a large number of frames need to be collected to reduce statistical errors. The high frame-rate digital camera synchronized to the laser repetition rate described in Sec. 3.3 meets these requirements and is able to achieve this kind of data acquisition in a reasonable time (half million frames in less than 20 minutes). Although correlation detection is able to handle multiple events in each frame, there are two constraints on the number of events. The first is concerned with ions from different channels landing at the same place on the MCP, which can be minimized by keeping the sample pressure low and by gating the MCP so that only a subset of all the ejected ions are detected (Sec. 3.2). The second involves saturation of a specific explosion channel which exists in too many frames. False correlation introduced by this channel needs to be eliminated

or minimized before real results can be extracted. The techniques of correlation detection discussed in this chapter are *image labeling* [99] (Sec. 4.2), *coincidence imaging* [63] (Sec. 4.3), and *joint variance* [103] (Sec. 4.4).

4.1 Image Spectrum

We begin our discussion by describing the characteristics of the image spectrum. As each laser pulse is focused at the interaction zone, a number of molecules are ionized and subsequently explode. Depending on the timing of the MCP gate (Page 51), tens of ions with specified charge and mass will generate bright spots on the phosphor screen. As these bright spots are captured by the digital camera in a single frame, up to about a hundred pixels will have values beyond the background.

The camera frames streamed to the SCSI drive from the digital camera are stored by recording the value of each pixel. Since each frame has 128×128 pixels and each pixel occupies one byte (8 bits), each frame takes 16 kilobytes (kB) of disk space and a typical experiment of 500,000 frames occupies about 8 gigabytes (GB). This huge size makes the data file extremely hard to be transfered and analyzed. Fortunately, since only a few percent of the pixels (100 out of 16 thousand) have values higher than the background (Page 53), these frames can be compressed dramatically into much smaller files [126]. The procedure of image compression and recovery is given in Appendix C.1. Only the pixels with values higher than the background (nonzero pixels) are recorded in the compressed image file. A typical compressed image file containing 100,000 to 500,000 frames only occupies several to

a few hundred megabytes (MB) of disk space and can be stored or transfered easily. In general, each ion striking the MCP illuminates a cluster of adjacent pixels on the camera. The number of pixels within a cluster is typically between 1 and 5. The procedure to group the adjacent pixels into a cluster and to determine the centroid of each cluster is given in Appendix C.2. The information of the clusters was stored in a separate file.

Since there are fewer than 100 nonzero pixels on each camera frame that have more than 16 thousand pixels, the single frame looks rather like a collection of random bright spots (upper three and lower left images in Fig. 4.1). However, if thousands of single frames are added together to form a composite or average image, structures corresponding to the molecular dynamics induced by the intense laser field emerge. The lower right image in Fig. 4.1 is a composite of 500,000 frames (synchronized to 500,000 laser pulses) and displays the momentum distribution of doubly and triply charged N and O ions originating from the Coulomb explosion of NO_2. As the center of the image coincides with the center of mass of the explosion, the radius R, where a charge appears on the image, is proportional to the momentum of this charge,

$$p = \sqrt{\frac{qeEm}{2l}}R, \qquad \mathcal{E} = \frac{qeE}{4l}R^2, \tag{4.1}$$

where $\mathcal{E} = p^2/(2m)$ is the kinetic energy, m and qe are the mass and charge of the ion, l is the distance from the laser focal point to the image MCP (Fig. 3.6), and E is the static field strength. (Detailed discussion about Eq. 4.1 is given in Appendix B.1.) Thus, the image is called the momentum distribution or momentum

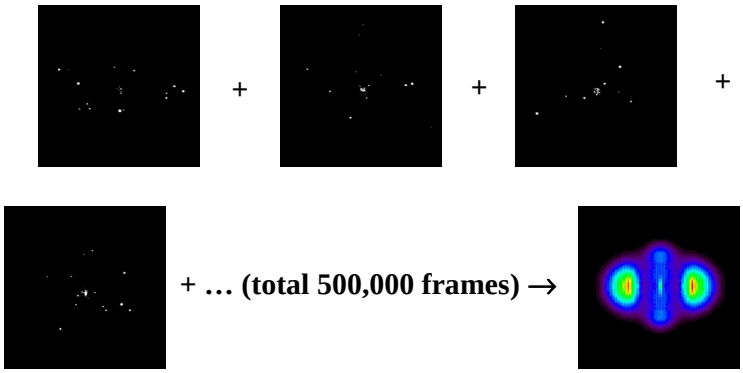

Figure 4.1: The composite image of NO_2 Coulomb explosions (lower right image) showing the momentum distribution of N^{q+} and O^{q+} ions (75% $q = 2$ and 25% $q = 3$). This distribution contains 500,000 camera frames, i.e., 500,000 laser shots, each centered at 800 nm, with a pulse width of 100 fs and linearly polarized (horizontal in the images) with a peak intensity of 2×10^{15} W/cm^2. The vertical peak near the center is composed of N^{q+} ions while the distribution parallel to the polarization axis is a mixture of both N^{q+} and O^{q+} ions. Four samples of single frames (upper three and lower left) are displayed.

spectrum. However, this is only true for the ions ejected approximately parallel to the MCP with no perpendicular momentum component ($p \simeq p_{\parallel}$ and $p_{\perp} \simeq 0$). In general, the momentum distribution on the image is distorted by the ion trajectories with $p_{\perp} \neq 0$. Although the ions with $p_{\perp} \neq 0$ can be eliminated and the correct momentum and angular distributions can be extracted by image deconvolution techniques [100, 127] – [130], the deconvolved images cannot be utilized to identify decay partners.

It is important to understand that deconvolution is not required for correlation images generated by the techniques described later in this chapter. This is because the peak correlation signals are due to the highest concentration of ions per unit area on the image [100, 103]. The concentration depends on the initial direction of

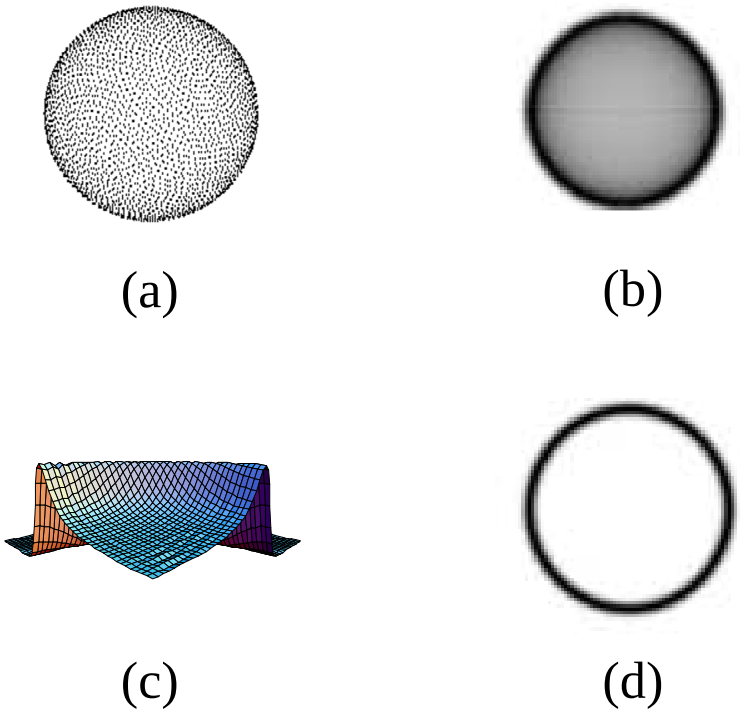

Figure 4.2: Locations where charges ejected isotropically into 4π sr with the same energy and a Gaussian energy spread will accumulate on a 2D image: (a) an isotropic distribution of charges in the absence of the static electric field form a sphere; (b) a simulated 2D image when all trajectories are collected on the MCP; (c) a surface plot of a quarter of the upper right image, the charge signal peaks at the edge of this bowl-shaped distribution where land the trajectories initially ejected parallel to the MCP ($p_\perp \simeq 0$); (d) a corral-shaped distribution formed when only the trajectories with $p_\perp \simeq 0$ are collected.

the explosion trajectories. As shown in Fig. 4.2, the highest concentration of ions for a given momentum corresponds to the trajectories with $p_\perp \simeq 0$. As a small region around the peak is isolated in correlation detection, the explosion events with $p_\perp \simeq 0$ are extracted. In general, ions ejected from these events ($p_\perp \simeq 0$) will land on the detector at the largest distance from the center of the image, which is proportional to the momenta of these charges (Eq. 4.1).

4.2 Image Labeling

Image labeling [99] is the 2-dimensional analog of *covariance mapping* [98] that has been employed successfully to analyze 2-atom Coulomb explosions. The technique allows all the correlated partners to be visualized with a family of momentum images similar to the total momentum distribution image but with only the correlated partners displayed. Each of these images is called a *correlation image*.

Covariance mapping, introduced by Frasinski *et al.* [98], is capable of reducing the ambiguity for correlating explosion partners in TOF waveforms. The covariance matrix, which identifies the explosion partners in the waveform at times t_α and t_β, is defined as

$$\xi_{\alpha\beta} = \langle S(t_\alpha)S(t_\beta)\rangle - \langle S(t_\alpha)\rangle\langle S(t_\beta)\rangle, \tag{4.2}$$

where $\langle\rangle$ means the average over N laser shots,

$$\begin{aligned} \langle S(t_\alpha)\rangle &= \frac{1}{N}\sum_{k=1}^{N} S_k(t_\alpha), \\ \langle S(t_\alpha)S(t_\beta)\rangle &= \frac{1}{N}\sum_{k=1}^{N} S_k(t_\alpha)S_k(t_\beta). \end{aligned} \tag{4.3}$$

The correlation coefficient is given by,

$$C_{\alpha\beta} \equiv \frac{\xi_{\alpha\beta}}{\sigma_\alpha\sigma_\beta}, \tag{4.4}$$

where

$$\sigma_\alpha = \sqrt{\frac{1}{N}\sum_{k=1}^{N}\left[S_k(t_\alpha) - \langle S(t_\alpha)\rangle\right]^2}. \tag{4.5}$$

Zhu and Hill [22] were the first to extend this technique to two-dimensional images. To produce a correlation image, the composite momentum distribution

image in Fig. 4.1 is divided into sectors, $\mathcal{S}(R,\theta)$. The size of each sector is chosen such that $\Delta\mathcal{E}(\propto R\Delta R$, see Eq. 4.1) and $\Delta\theta$ are the same for all sectors. This is shown in Fig. 4.3. The correlation coefficient, C_{ij}, between sectors i and j that are actually two-dimensional indices representing (R_i,θ_i) and (R_j,θ_j), is given by [99]

$$\begin{aligned} C_{ij} &= \frac{\xi_{ij}}{\sigma_{S_i}\sigma_{S_j}}, \\ \xi_{ij} &= \langle (S_i - \langle S_i\rangle)(S_j - \langle S_j\rangle)\rangle = \langle S_iS_j\rangle - \langle S_i\rangle\langle S_j\rangle, \\ \sigma_{S_i} &= \sqrt{\langle (S_i - \langle S_i\rangle)^2\rangle}, \end{aligned} \tag{4.6}$$

where ξ_{ij} is the covariance between sectors i and j, σ_{S_i} is the square root of the variance in the counts for sector i with laser shots, and $\langle\rangle$ means the average over N laser shots,

$$\begin{aligned} \langle S_i\rangle &= \frac{1}{N}\sum_{k=1}^{N} S_i(k), \\ \langle S_iS_j\rangle &= \frac{1}{N}\sum_{k=1}^{N} S_i(k)S_j(k). \end{aligned} \tag{4.7}$$

Typically, about 500 sectors are employed and there are about 10 – 25 pixels in each sector. For C_{ij} to be meaningful, it is critical that the average number of ions generated per sector per laser shot be less than one and that the image for each laser shot be stored individually. This matrix identifies explosion partners at locations i and j. With two-dimensional images, i and j are two-dimensional indices and C_{ij}, or ξ_{ij}, is four-dimensional, which is impossible to display. It is not necessary, however, to display or even calculate all the elements because useful correlations can be obtained from a judicious subset of two-dimensional projections [22]. In particular, the i^{th} correlation image is assembled by replacing the ion counts at

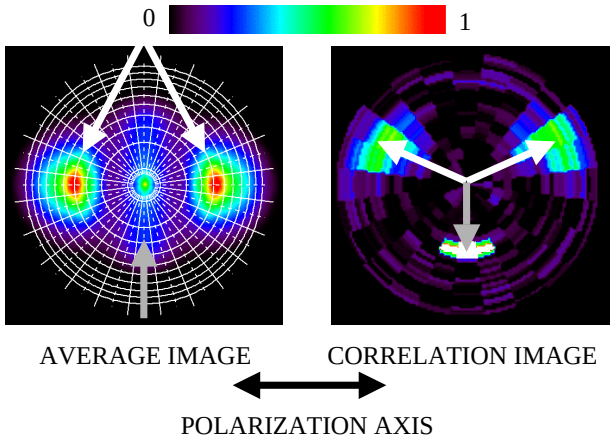

Figure 4.3: Correlation images. The concentric circles and spokes in the left panel divide the momentum distribution image (the same as that displayed in Fig. 4.1) into sectors. The gray arrow indicates labeled ions (i.e., a subset of ions with a narrow momentum distribution moving downward, 6 o'clock); the white arrows indicate the correlated sectors (ions moving toward 2 and 10 o'clock). The right panel shows the correlation image for the Coulomb explosion where all three atomic ions are ejected simultaneously. The gray (white) arrows indicate the final momenta of the labeled (correlated) charges.

the pixels of the j^{th} sector in the composite image (i.e., the left panel in Fig. 4.3) with the correlation coefficient C_{ij}. This is actually a two-dimensional projection from the four-dimensional correlation matrix, which is labeled or selected by the i^{th} sector. The right panel in Fig. 4.3 shows one correlation image of a 3-body Coulomb explosion of NO_2. There are as many correlation images (two-dimensional projections) as there are sectors.

The advantage provided by the correlation images is that they not only tell us which ions are ejected simultaneously as *covariance mapping* of TOF spectrum does, they offer clear pictures of both linear and bent Coulomb explosions which can be viewed easily. Figure 4.4 shows how linear and bent three-body channels can be isolated for Coulomb explosions of CO_2 as the ions ejected together are clearly

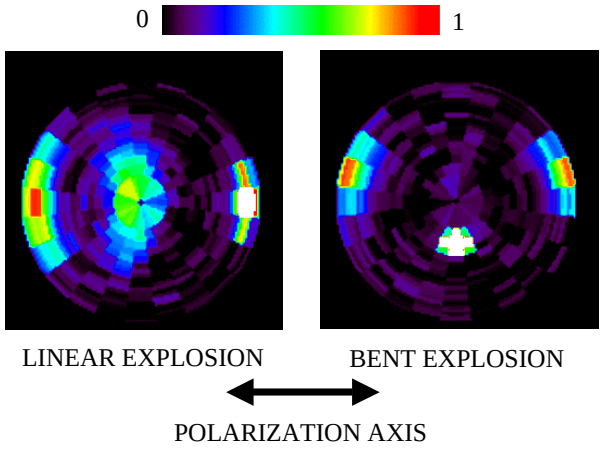

Figure 4.4: Two correlation images for the Coulomb explosion of CO_2 taken under the same conditions as in Fig. 4.1. Ions moving toward 3 o'clock in the left image and those moving toward 6 o'clock in the right image are labeled. As the correlated ions show up on the same correlation images, linear explosion events on the left and bent events on the right are displayed and isolated.

displayed, while linear two-body and bent three-body explosion channels of NO_2 are distinguished in Fig. 4.5.

Although the C_{ij} values for the sectors can be used to determine the degree of correlation, it is more flexible and visual to work directly with the pixels, as shown in Fig. 4.6. The image on the right was generated by taking the difference between the average distribution shown on the left (all 500,000 frames) and an average distribution composed only of frames that have nonzero counts in the i^{th} sector – a selective average [99] (Fig. 4.7). The selective average and correlation image projected from the four-dimensional C_{ij} matrix give about the same result but the selective average approach provides higher resolution, better control over the size and location of the labeled sector, and an easier visualization without projection or dimensionality reduction. As the momentum (location) of the labeled sector is

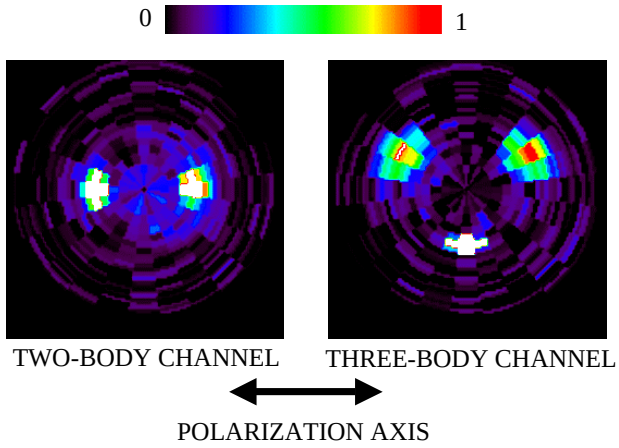

Figure 4.5: Two correlation images for NO_2 taken from the same data set as in Fig. 4.1 showing a two-body dissociation channel (left) and a three-body channel (right). Ions moving to the left along the polarization axis in the left image and those moving in the direction perpendicular to the polarization axis in the right image are labeled so that two-body and three-body events are isolated.

being varied, the ejection dynamics as a function of the momentum of a particular partner can be studied. While the momentum of the selected charge (gray arrow in Fig. 4.6) is predefined, the momenta of the correlated ions (white arrows in Fig. 4.6) are found at the peaks of the selective average image. With the momenta of all three charges ejected from the same explosion event relative to the center of mass of the dynamics (the center of the image), the pre-explosion molecular structure (bond length and bond angle) of the triatomics in this study (CO_2 and NO_2) can be determined. Assuming a pure Coulomb interaction between the correlated ions and energy conservation, $\mathcal{E}_k = \mathcal{E}_C$, we have

$$\mathcal{E}_C = \sum_{i>j}^{3} \frac{K q_i q_j e^2}{r_{ij}}, \qquad \mathcal{E}_k = \frac{1}{2} \sum_{i=1}^{3} \frac{p_i^2}{m_i}, \tag{4.8}$$

where i, $j = 1$, 2, 3. The subscripts 1 and 2 represent the two outer ions (oxygen) while 3 represents the center ion (carbon or nitrogen). The mass, charge, initial

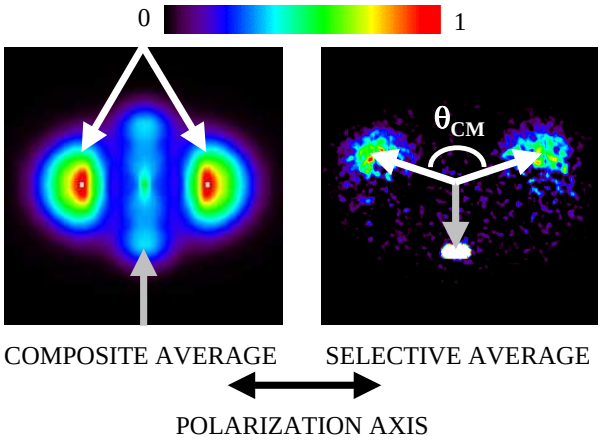

Figure 4.6: Selective average. The image in the left panel and the gray and white arrows are the same as in Fig. 4.3. The correlation image (selective average) in the right panel is the difference between averaging only those frames that have nonzero counts in the labeled sector and all 500,000 frames.

position and final momentum of each ion are given by m_i, $q_i e$, $\vec{r}_i$ and $\vec{p}_i$ respectively. The initial Coulomb potential energy and final kinetic energy are $\mathcal{E}_C$ and $\mathcal{E}_k$. The bond lengths are $r_{13} = |\vec{r_1} - \vec{r_3}|$ and $r_{23} = |\vec{r_2} - \vec{r_3}|$, while the angle between $\vec{r}_{13}$ and $\vec{r}_{23}$ is the bond angle. Detailed calculation is given in Appendix D.

4.3 Coincidence Imaging

While *image labeling* (Sec. 4.2) can isolate specific bond angles, extracting the relative strength of the explosion signal requires a triple-coincidence – *coincidence imaging* [63]. This is because the correlation image (selective average) contains events with a spread in $p_\perp$ about $p_\perp = 0$, as indicated by the width of the correlated spots (Figs. 4.6 and 4.8b). We can reduce this spread by reducing the size of the correlated spots. Using the fact from Fig. 4.2 that the highest concentration

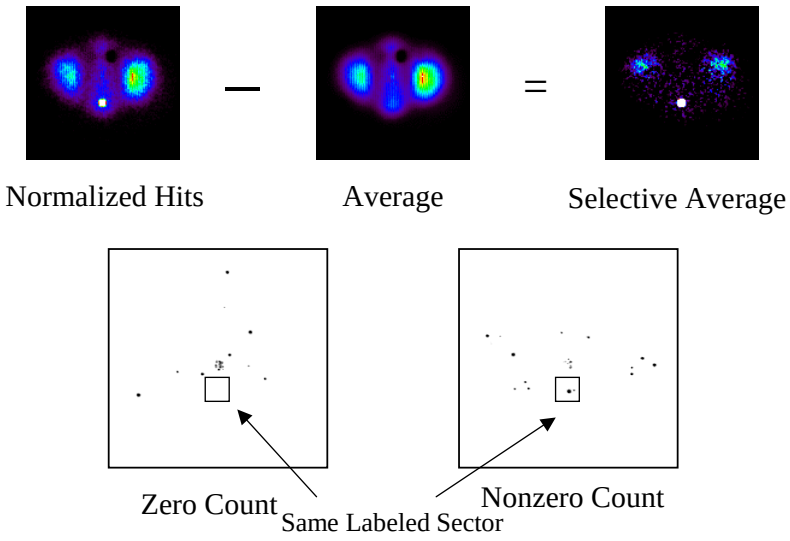

Figure 4.7: Selective average. The images in the upper row shows that a selective average is generated by taking the difference between an average distribution composed only of frames that have nonzero counts in the labeled sector (lower right image) and the average distribution of all 500,000 frames. The lower row shows two single frames with zero and nonzero counts in the same labeled sector.

of charges for a given momentum allows us to extract events with $p_\perp = 0$, if we focus on a narrow region about the peak point. Figure 4.8 shows an example of *coincidence imaging* for the 6-electron explosion channel of CO_2. Figure 4.8a is the momentum distribution of the ejected doubly-charged ions, while a selective average containing only the ions ejected simultaneously is shown in Fig. 4.8b. After the momenta of all three explosion partners ($\vec{p}_{O_{left}}$, $\vec{p}_C$, $\vec{p}_{O_{right}}$) were determined from Fig. 4.8b, a narrow region around each momentum vector is chosen and an image (Fig. 4.8e) can be obtained by integrating only the frames containing ions in all three regions simultaneously. Since the ions are constrained in a very narrow region, they are from the events with $p_\perp = 0$. The strength of the signal or probability for a particular explosion is proportional to the number of frames containing all the

explosion partners.

We determine if a single frame contains all the explosion partners in *coincidence imaging* in the following way. The conditions under which the experiment was run allowed only a few explosion events per laser shot. As the clustered images (Page 57 and App. C.2) are employed to avoid the signal of one charge spreading over several pixels, there are two criteria a cluster must meet to be considered to be part of a *real* triple-coincidence. The first signature is that the location of the centroid of a valid cluster must fall within a circle of radius r_0 around the final momentum of each ion ($\vec{p}_{O_{left}}$, $\vec{p}_C$, and $\vec{p}_{O_{right}}$, Fig. 4.8). The size of r_0 is related to the uncertainty in determining the location of the centroid, which typically is 1 to 3 pixels because the peak number of pixels in a cluster is roughly 1 – 5. It is set that $r_0 = 1.5$ and 2.5 for triple-coincidence measurements for CO_2 and NO_2 respectively; $r_0 = 1.5$ for double-coincidence measurements for H_2. The second requirement for inclusion is that there can only be one centroid (cluster) within each circle. To avoid invalid clusters, each of which is illuminated by two or more ions landing near each other on the MCP, valid clusters are restricted to those having a maximum number of pixels (M). The value of M is typically between four and ten where the occurrence frequency of clusters as a function of number of pixels in a cluster falls to about 10% of its peak value (App. C.2). As shown in Fig. 4.8g, a centroid may be partially enclosed by the circle. Centroids falling entirely within the circle (block 1 in Fig. 4.8g) contribute unity to the count while those that are partially enclosed (block 2 in Fig. 4.8g) contribute fractional counts. The contribution to the signal strength for a specific frame is given by the product of the count from each ion circle

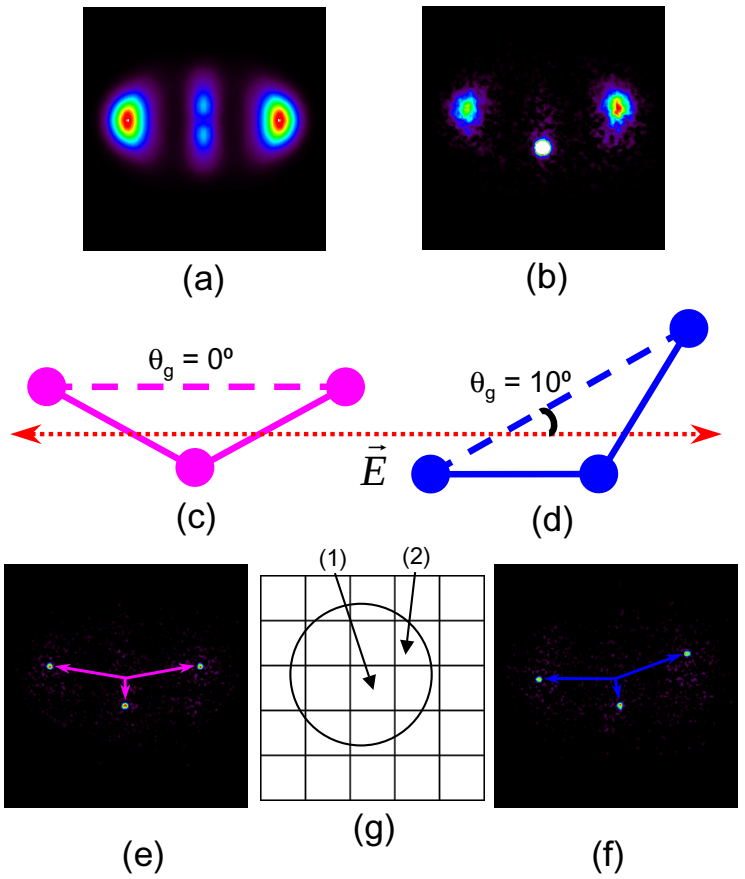

Figure 4.8: Center-of-mass momentum distributions of ejected C^{2+} (center spots) and O^{2+} (outer spots) ions associated with the symmetric CO_2^{6+} Coulomb explosion channel, induced by linearly polarized (horizontal), 100 fs pulses at 800 nm focused to 2×10^{15} W/cm^2. (a) Average distribution composed of 500,000 frames. (b) Selective average showing only the momenta of the three charges ejected simultaneously from a CO_2^{6+} precursor with a bond angle of 163°. (c) A ball-and-stick diagram of CO_2 defining the molecular axis (dashed line) and the geometric angle, $\theta_g = 0°$, which is the angle between the laser polarization and the molecular axis (the line connecting two outer ions). (d) The same as (c) for $\theta_g = 10°$. (e) Triple-coincidence image (see text) corresponding to (c). (f) The same as (e) but corresponding to (d). The arrows in (e) and (f) represent the final momenta of the ejected ions ($\vec{p}_{O_{left}}$, $\vec{p}_C$, $\vec{p}_{O_{right}}$). The angle between $\vec{p}_{O_{left}}$ and $\vec{p}_{O_{right}}$ defines the center-of-mass angle θ_{CM}. (g) Grid illustrating how contributions to the signal strength are determined. Block 1 makes a unit contribution while block 2 contributes only 0.6, corresponding to the area enclosed by the circle.

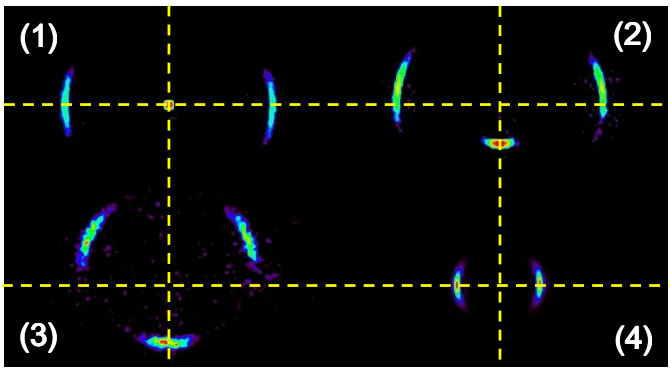

Figure 4.9: Images showing the anisotropies in the ejection angular distribution of Coulomb explosions for selected bond angles: (1) CO_2^{6+} at 180°, (2) CO_2^{6+} at 163°, (3) NO_2^{6+} at 132° and (4) H_2^+. These images were constructed by adding a series of coincidence images similar to those shown in Figs. 4.8e and 4.8f. The dashed lines represent the axes, parallel and perpendicular to the laser polarization, which cross at the center-of-mass. In (1) – (3), the largest arcs correspond to O^{2+} ions.

– if each centroid were only 50% enclosed, this frame would contribute 0.125 to the total count.

By keeping the magnitudes of the momenta along with the relative angles between them constant (compare the stick figures in Figs. 4.8c and 4.8d), the probability for strong-field induced Coulomb explosion as a function of the *geometric* orientation angle (θ_g, defined as the angle between the molecular axis and the polarization axis) for specific bond angles can be determined from the relative strength of the explosion signal on triple-coincidence images like Figs. 4.8e and 4.8f, and an image can be generated to reveal the anisotropic angular distribution graphically. Figure 4.9 shows the probability for Coulomb explosion as a function of θ_g for several bond angles as well as for H_2.

4.4 Joint Variance

When selective averages and coincidence images are contaminated with false correlation because of saturation of one or more very strong channels, covariance matrix (ξ_{ij} in Eq. 4.6) does a better job of determining true ejection partners. Correlating three or more components, however, requires higher order variance calculations. Frasinski, *et al.* [64] have explored this approach and suggested

$$\begin{aligned}\xi_{\alpha\beta\gamma} &= \langle S(t_\alpha)S(t_\beta)S(t_\gamma)\rangle - \langle S(t_\alpha)S(t_\beta)\rangle\langle S(t_\gamma)\rangle \\ &\quad -\langle S(t_\alpha)S(t_\gamma)\rangle\langle S(t_\beta)\rangle - \langle S(t_\alpha)\rangle\langle S(t_\gamma)S(t_\gamma)\rangle \\ &\quad +2\langle S(t_\alpha)\rangle\langle S(t_\beta)\rangle\langle S(t_\gamma)\rangle, \end{aligned} \tag{4.9}$$

as the appropriate triple variance of TOF spectrum to be calculated. However, the image analogue to $\xi_{\alpha\beta\gamma}$ is found to be quite noisy, making it difficult to extract useful information. As an alternative, a product of pairwise-determined covariances, or *joint variance* [103], has been employed successfully to reduce the effects of the contaminating channel.

Following the definition of the regular covariance (ξ_{ij}) in Eq. 4.6, *joint variance* ξ^J of B with A and C, which is actually a measure of triple-correlation of all three charges, is given by

$$\begin{aligned}\xi^J_{A\bar{B}C} &= \xi_{AB}\cdot\xi_{BC}, \\ &= \left(\langle S_A S_B\rangle - \langle S_A\rangle\langle S_B\rangle\right)\cdot\left(\langle S_B S_C\rangle - \langle S_B\rangle\langle S_C\rangle\right), \end{aligned} \tag{4.10}$$

where the bar over B indicates the common entity in the calculation. Let us assume an explosion channel $ABC \rightarrow A{+}B{+}C$, which is the target of the correlated-partner

search, is contaminated by a very strong channel $AC \rightarrow A{+}C$. Even though ξ_{AC} may be significant, it does not reflect the *real* 3-body correlation appropriately. However, it plays a primary, or at least, the same role as ξ_{AB} and ξ_{BC} in the triple coincidence approach, skewing the results to higher values. By contrast, in *joint variance*, ξ_{AC} is forced to play only a secondary role at best to reduce the contamination as we will show in the next chapter.

Chapter 5

EXPERIMENTAL RESULTS AND ANALYSIS

Exploiting the ability of the image spectrometer [22, 100] to collect all the ejected charges over 4π sr (Chap. 3) and correlation techniques [63, 99, 103] to identify ejections at different bond and orientation angles (Chap. 4), Coulomb explosions of small molecules were investigated with 800 nm, 100 fs laser pulses at intensities of $0.1 \sim 5 \times 10^{15}$ W/cm^2. The explosion dependence on the bond angle of triatomic molecules and orientation angle of diatomic and triatomic molecules was studied.

In the bond-angle studies (Sec. 5.1), CO_2 [62] and NO_2 (with equilibrium bond angles of 180° and 134°, respectively) were the targets. This allowed us to compare and contrast the dynamics in nominally linear and bent systems. Energies, momenta and signal strengths of the fragment ions from Coulomb explosions were measured as functions of bond angle with correlation detection techniques (Secs. 5.1.1.1 and 5.1.1.2). Large-amplitude vibrations were observed in explosion signals of both CO_2 and NO_2 and analyzed with the bending vibrational amplitude of the molecules (Sec. 5.1.1.3). The measured explosion energies were compared with predictions from the enhanced-ionization (R_C) and electron-screening models (Sec. 5.1.2).

In the orientation-angle studies (Sec. 5.2), the ejection anisotropy of triatomic (CO_2 and NO_2) [63] and diatomic (H_2, N_2, and O_2) Coulomb explosions were investigated with correlation detection techniques and by comparing image spectra

obtained with linearly and circularly polarized fields. The results are discussed in Sec. 5.2.1. The different behavior (ejection angular spreads and degrees of dynamic alignment) of the tested molecules was explained in terms of their ionization stages, induced dipole moments, rotational constants as well as the time that the precursor molecular ions spend in the field prior to the Coulomb explosions (Sec. 5.2.2).

5.1 Explosion Energy Measurement

5.1.1 Experimental Results

The focus of this study was the symmetric 6-electron explosion channel where CO_2 or NO_2 was ionized six times prior to the Coulomb explosion into energetic O^{2+} + C^{2+} + O^{2+} or O^{2+} + N^{2+} + O^{2+} ions. The experiments were taken at peak laser intensities (I_0) $\sim 2 \times 10^{15}$ W/cm^2, pulse widths (τ) $\sim$ 100 fs, and center wavelength (λ) $\sim$ 800 nm. Each experiment consisted of 500,000 camera frames corresponding to the same number of laser pulses. The sample gas pressures were 5 and 30×10^{-9} Torr for CO_2 and NO_2, respectively. The NO_2 signal was roughly six times weaker than the CO_2 signal. The potential between the laser focal point and the MCP in the image spectrometer was V_{int} = 1500 volts, so that the static field pushing the ions to the MCP was 262 V/cm (see Fig. 3.6). The image calibration was κ = 0.293 mm/pixel (Page 146 in App. B.1) – one pixel on the image (camera frame) corresponded to a distance of 0.293 mm on the image MCP. Therefore, the momentum and energy of the ion at radius r (in the unit of pixel) on the image spectrum were $p = 1.15\sqrt{qmr}$ and $\mathcal{E} = 0.00986qr^2$, where q and m are the charge

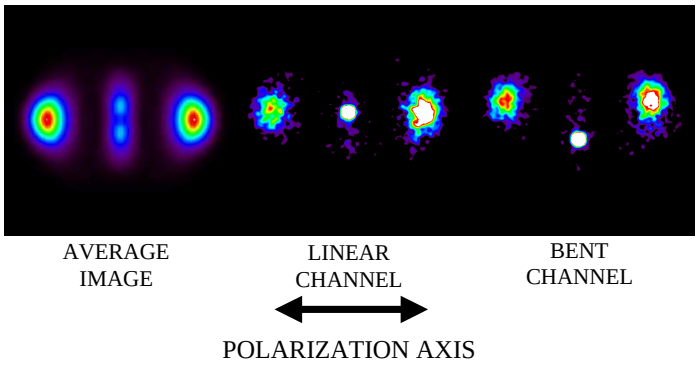

Figure 5.1: Momentum distributions of the C^{2+} and O^{2+} ions associated with the symmetric CO_2^{6+} Coulomb explosions: average image composed of 500,000 laser pulses (left); correlation images (selective averages, Sec. 4.2) showing only the momenta of the three charges ejected simultaneously from a CO_2^{6+} parent that is linear and parallel to the polarization axis (center) and bent at a bond angle of $\sim 165°$ with the plane of the molecule parallel to the MCP face (right). The geometric center of each image is the center of mass of the explosion and the arrow indicates the polarization axis. The width of the MCP gate (Sec. 3.2) was 320 ns, which covers all C^{2+} and O^{2+} ions and a small amount of C^{3+} and O^{3+} ions (less than 20% of the total signal) due to the overlap of signals in time.

and mass of the ion in the units of elementary charge and atomic mass, respectively. The momentum p and energy $\mathcal{E}$ are in atomic units (a.u.) and electron volts (eV), respectively.

5.1.1.1 CO_2 Results

The momentum distribution of the doubly charged atomic ions from CO_2 explosions is shown in the left image in Fig. 5.1. The distribution is composed of O^{2+} ions with momenta of 160 to 350 a.u. (10% of peak) and directed parallel (within a small angular spread) to the polarization axis (p_X) and C^{2+} ions with momenta of 0 to 200 a.u. and directed perpendicular (within a small angular spread, too) to the polarization axis (p_Y). The ratio of the signals of the middle peak (C^{2+}) and

peaks on both sides (O^{2+}) is about 1:2.5; the small deviation from the expected 1:2 (one carbon and two oxygen ions from CO_2) is due primarily to the gain variation on the MCP. The center and right images in Fig. 5.1 are two examples where *image labeling* (Sec. 4.2) was employed to isolate explosion events that occurred at two different bond angles (θ_b). When C^{2+} ions (the white spots in the middle of center and right images in Fig. 5.1) with specific p_Y ($p_X \equiv 0$ in this case) are selected, the correlated O^{2+} ions exist in these images as well, which allows the momenta of all the ions ejected simultaneously to be determined. While the momentum of the selected C^{2+} ions is predefined, the momenta of the O^{2+} ions are taken to be at the peaks of the correlated ions (the left and right spots in the center and right images in Fig. 5.1). At the same time, the center-of-mass angle (θ_{CM}, the angle between the momenta of two oxygen ions) is calculated from p_X and p_Y of the oxygen ions – $\theta_{CM} = 2\tan^{-1}(p_X/p_Y)$. The pre-explosion bond angle (θ_b) and bond length can be determined from the momenta and θ_{CM}, as described in the next paragraph. Simultaneous ejection means that the correlated ions must obey energy and momentum conservation. Thus, p_X for the two groups of O^{2+} ions in the center and right images are equal and opposite while p_Y for C^{2+} are equal and opposite to the sum of p_Y for the two groups of O^{2+} ions. We note that this measurement does not assume momentum conservation. In stead, the result – data points of $|p_Y|$ for C^{2+} and $2|p_Y|$ for O^{2+} are consistent with each other within their standard deviations – confirms that the momenta are actually conserved in Fig. 5.2, which shows how $|p_X|$ and $|p_Y|$ for the correlated ions depend on the bond angle of the parent molecule at the time of the explosion. At the same time, Fig. 5.2 also shows

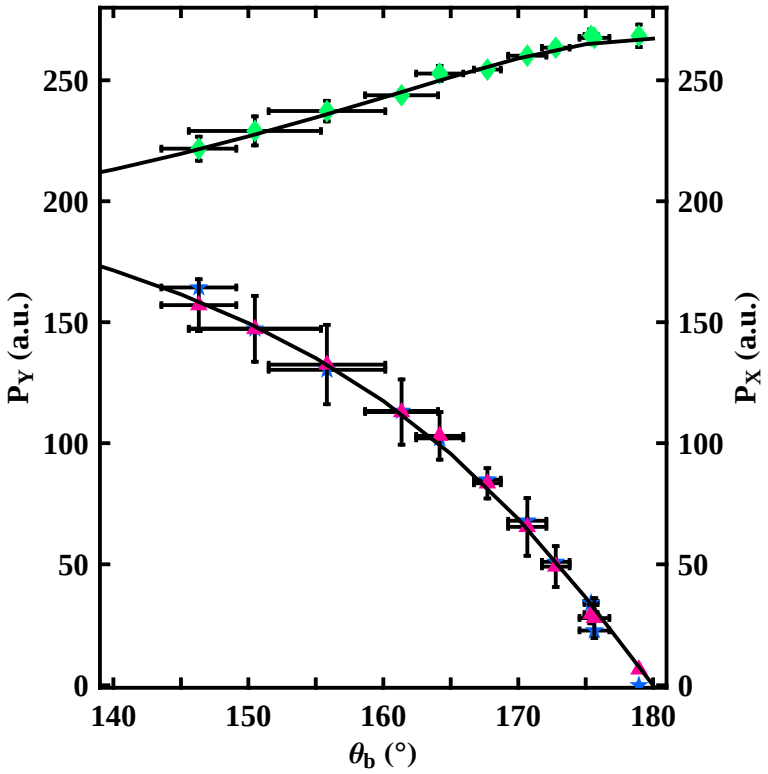

Figure 5.2: Momenta of the three charges ejected simultaneously as a function of the bond angle (θ_b) in the symmetric CO_2^{6+} Coulomb explosion channel. Each data point represents the momentum measured from the center-of-mass of the charge distribution in a correlation image similar to the two right images in Fig. 5.1; the error bars represent the standard deviation in this determination over four runs. The upper series of points (green diamonds) correspond to $|p_X|$ for O^{2+}; $|p_X|$ is virtually the same for the two groups of ions so only one point is plotted for each angle. The lower trace is $|p_Y|$ for C^{2+} (blue stars) and $2|p_Y|$ for O^{2+} (red triangles); p_Y is also the same for the two groups of O^{2+} ions. The solid curves represent the calculated momenta assuming R_C equals 0.215 nm (see App. D for details of this calculation).

that the data points are consistent with the calculated momenta assuming a constant bond length, indicating that R_C of CO_2^{6+} explosions is nearly independent of θ_b over the observed range [62].

The explosion energy ($\mathcal{E}_k$), which is assumed to be equal to the initial Coulomb

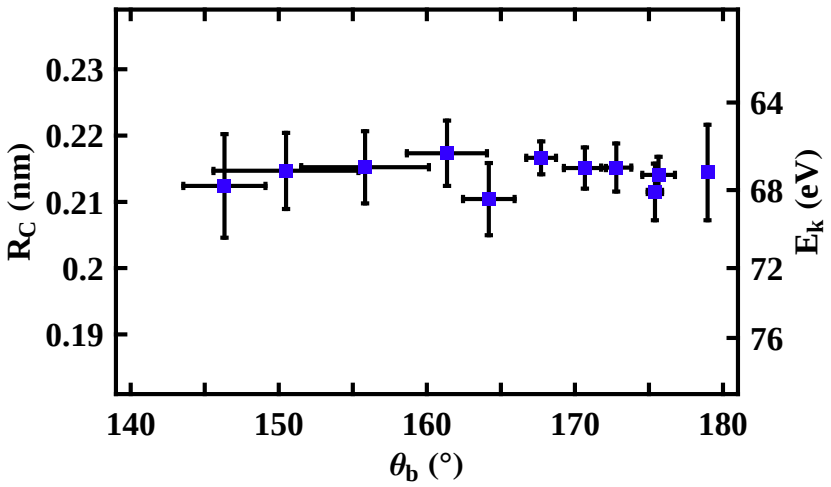

Figure 5.3: Bond length (left axis) and explosion energy (right axis) as functions of bond angle for CO_2^{6+} symmetric explosions with $q_O = q_C = 2$ measured by *image labeling* (Sec. 4.2). The error bars are the standard deviation of four experiments under the same conditions.

potential energy ($\mathcal{E}_C$), can be calculated from the momenta of all three charges by,

$$\mathcal{E}_k = \frac{1}{2}\sum_{i=1}^{3}\frac{p_i^2}{m_i}, \tag{5.1}$$

where $i = 1, 2, 3$. The mass and final momentum of each ion are given by m_i and $\vec{p}_i$ respectively (see Eq. D.8). The initial molecular structure prior to the explosion, the CO bond length R and bond angle θ_b, was then extracted as described in Appendix D. The bond length ($R = R_C$, assuming the explosion occurs at R_C of the enhanced ionization, see Sec. 2.1.1) and explosion energy ($\mathcal{E}_k$) as functions of bond angle are plotted in Fig. 5.3. The measured R_C for CO_2^{6+} explosions is constant (0.215 nm) and varies by less than 0.1% for the observed θ_b between 145° and 180°.

The explosion signal strength was measured at each bond angle by *coincidence imaging* (Sec. 4.3), where a narrow region around each of the three momenta determined by *image labeling*, as mentioned above, was chosen and the signal strength

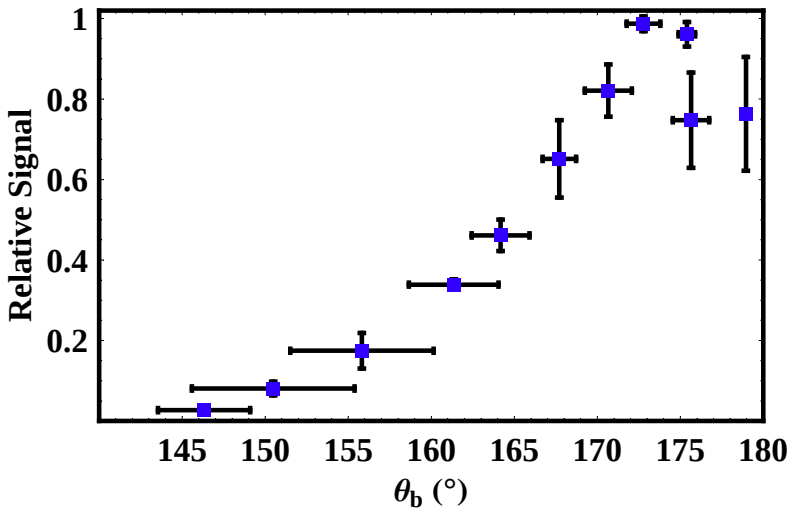

Figure 5.4: Explosion signal strength as a function of bond angle for CO_2^{6+} symmetric explosions initiate with $q_O = q_C = 2$ measured by *coincidence imaging* (Sec. 4.3) at the momenta of the three charges determined by selective averages. The error bars are the standard deviation of four experiments under the same conditions.

was determined by the number of frames containing ions in all three regions simultaneously. The measured distribution is shown in Fig. 5.4 and peaks near $\theta_b = 173°$. This observation will be discussed later in Sec. 5.1.1.3.

5.1.1.2 NO_2 Results

While the measured momenta and energies of CO_2 explosions are consistent with a constant R_C, that for NO_2 is totally different. The momentum distribution for the doubly charged atomic ions of NO_2 is shown in the left image in Fig. 5.5. The distribution is composed of O^{2+} and N^{2+} ions with momenta of 90 to 300 a.u. (10% of peak) and directed parallel (within a small angular spread) to the polarization axis (p_X) and N^{2+} ions with momenta of 0 to 220 a.u. and directed perpendicular (within a small angular spread) to the polarization axis (p_Y). The ratio of the signals of the

middle peak (N^{2+}) and peaks on both sides (O^{2+} and N^{2+}) is about 1:4.5. This large deviation from the expected 1:2 (one nitrogen and two oxygen ions from NO_2) is due primarily to a two-body explosion channel, as will be discussed later. Similar to the CO_2 case, Fig. 5.6 shows how $|p_X|$ and $|p_Y|$ for the correlated ions depend on the pre-explosion bond angle of the parent molecule. Although the consistency between data points of $|p_Y|$ for N^{2+} and $2|p_Y|$ for O^{2+} confirms momentum conservation, data points of both $|p_X|$ and $|p_Y|$ deviate from the constant-R_C curves. Especially, $|p_X|$ points deviate further as the bond angle increases. It is clear that R_C for NO_2 explosions is not constant. The bond length ($R = R_C$) and explosion energy ($\mathcal{E}_k$) as functions of bond angle, derived from the measured momenta with the same method as in the CO_2 case, are plotted in Fig. 5.7, which confirms that R_C for NO_2 explosions is not constant. The curve of R_C ($\mathcal{E}_k$) shows a monotonic increase (decrease) as θ_b approaches 180°.

Structurally, the momentum distribution of NO_2 looks similar to that of CO_2, but the dynamics are quite different. As shown in the center plot of Fig. 5.5, a very strong two-body correlation along the polarization axis was revealed by *image labeling*, which was not observed in the CO_2 spectrum. The fact that the ratio of signals in the middle and side peaks in the momentum distribution (about 1:4.5, left image in Fig. 5.5) deviates from the expected 1:2 confirms that there are ions from channels other than three-body explosions in the side peaks. This channel probably involves an N–O explosion because there is a strong 2-photon dissociation for $NO_2 \rightarrow O + NO$ with little kinetic energy. As one oxygen leaves the molecule, $NO \rightarrow N^{2+} + O^{2+}$ explodes as a diatomic. The second possibility is an $O^{2+}-O^{2+}$

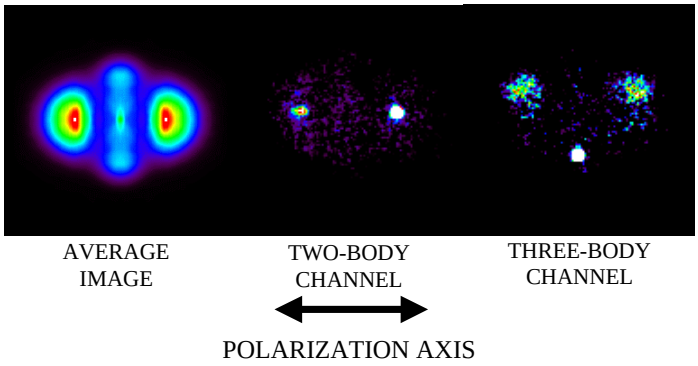

Figure 5.5: Two- and three-body explosion channels of NO_2. Left: average of N^{2+} and O^{2+} ions over 500,000 laser shots; center: selective average of two-body correlation channel where the bright spot to the right is the selected sector; right: selective average of three-body correlation channel where the bright spot in the middle is the selected sector. Polarization axis is horizontal. The width of the MCP gate (Sec. 3.2) was 330 ns, which covers all N^{2+} and O^{2+} ions and a small amount of N^{3+} and O^{3+} ions (less than 20% of the total signal) due to the overlap of signals in time.

explosion with the nitrogen atom dropped as a neutral. The impurity of NO and O_2 in the NO_2 gas cylinder (less than 0.5%) is not enough to explain the observed two-body explosion signal. However, due to the fact that the ejection energy (about 10 eV) and mass of N and O are very close to each other, correlation imaging (Sec. 4.2) could not discriminate N–O and O–O explosions on the image spectrum. At the same time, due to the overlap of signals from two- and three-body channels, covariance mapping of TOF spectrum (Sec. 4.2) could not produce definite results to reveal which explosion, N–O or O–O, was more dominate, either. Discriminating N–O from O–O explosion could have interesting consequences for laser control and should be further pursued. This two-body channel was treated as noise for the current study.

As verified by *coincidence imaging* measurements (Sec. 4.3), the strength of the

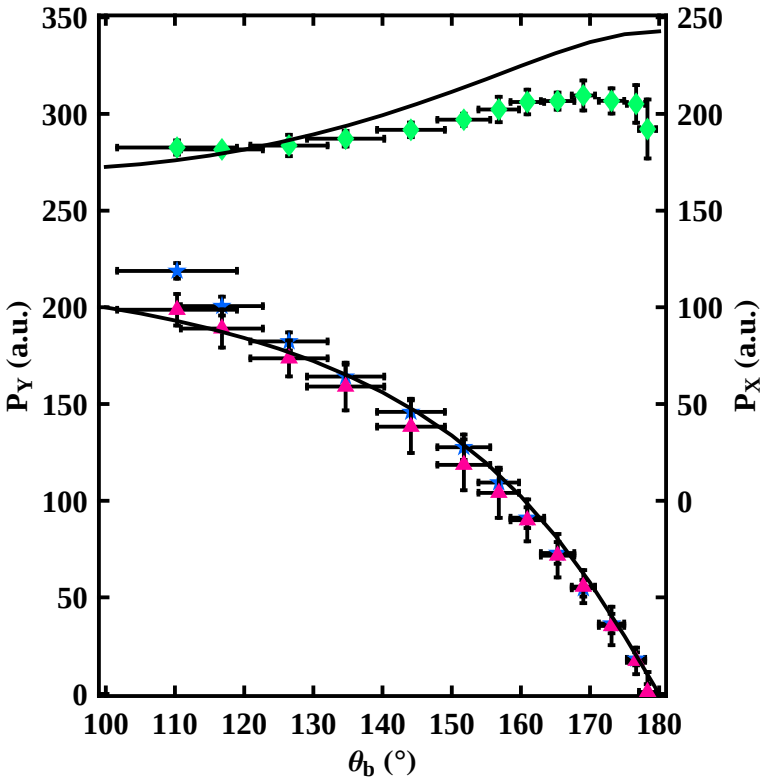

Figure 5.6: Momenta of the three charges ejected simultaneously as a function of the bond angle (θ_b) in the symmetric NO_2^{6+} Coulomb explosion channel determined by *image labeling*. The error bars represent the standard deviation in this determination over seven runs. The upper series of points (green diamonds) correspond to $|p_X|$ for O^{2+}; $|p_X|$ is virtually the same for the two groups of ions so only one point is plotted for each angle. The lower trace is $|p_Y|$ for N^{2+} (blue stars) and $2|p_Y|$ for O^{2+} (red triangles); p_Y is also the same for the two groups of O^{2+} ions. The solid curves represent the calculated momenta assuming R_C equals 0.26 nm (see App. D).

two-body channel (double-coincidence) is more than 10 times stronger than linear three-body explosions (triple-coincidence). The momenta of the ejected ions for the three-body Coulomb explosion obtained by image labeling and the signal strength obtained by coincidence imaging could be distorted, especially near θ_{CM} (as well as θ_b) close to 180°, where the spectra of these two channels overlap (Fig. 5.8).

As shown in the top plot of Fig. 5.8, the O^{2+} momentum increases smoothly as C^{2+} momentum decreases from the edge of the selected group to the image

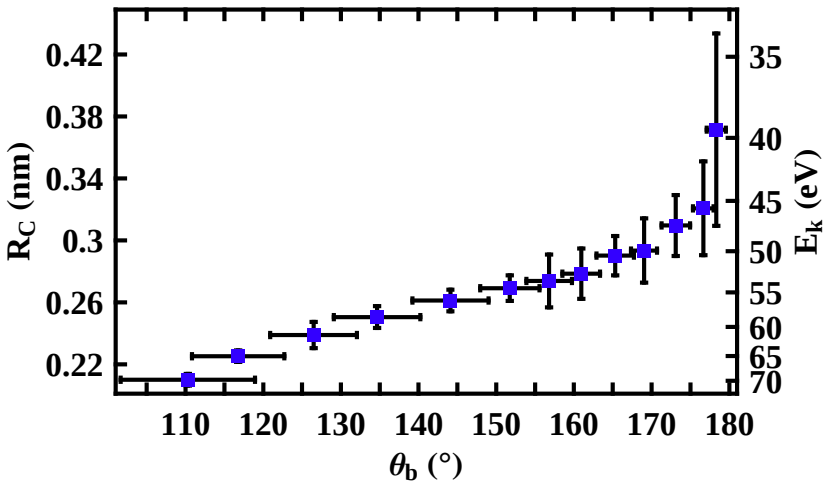

Figure 5.7: Bond length (left axis) and explosion energy (right axis) as functions of bond angle for NO_2^{6+} symmetric explosions initiate with $q_O = q_C = 2$ measured by *image labeling* (Sec. 4.2). The error bars are the standard deviation of seven experiments under the same conditions.

center (center of mass) and peaks at linear configuration ($\theta_{CM} = 180°$) for CO_2 3-body explosions. By contrast, the O^{2+} momentum from NO_2 explosions determined by selective average (center plot of Fig. 5.8) has an abrupt change near $\theta_{CM} \sim 180°$. As will be shown, this distortion is caused by the strong two-body channel. When an N^{2+} ion near the image center (zero momentum) is selected, the correlated O^{2+} will only appear near the polarization (horizontal) axis as the momentum is constrained by momentum conservation. At the same time, because of its larger signal strength and higher occurrence frequency, O^{2+} ejected from the two-body channel also appears in the selective average along the polarization axis, causing accidental correlations in the three-body image-labeling measurement. This tends to shift the positions of the correlated O^{2+} ions to smaller momenta because O^{2+} from the 2-body channel has a smaller momentum than that from the 3-body channel.

As the selected N^{2+} moves away from the center of the image (larger momentum perpendicular to the polarization axis), the correlated O^{2+} picks up perpendicular momentum as well and the contamination from the two-body channel becomes less significant.

Since the *image labeling* (selective average) measurement was strongly distorted by the 2-body channel, *joint variance* [103], as described in Sec. 4.4, was employed to analyze the signal of the 3-body explosion. *Joint variance* is able to emphasize the existence of the N–O correlation in the triple-correlation and force the correlation between two outer ions to play only a secondary role to reduce the contamination from the two-body channel. As S_A, S_B and S_C in Eq. 4.10 are taken to be $S_{O_{left}}$ (signal of O on the left side of the image), S_N (signal of N in the middle) and $S_{O_{right}}$ (signal of O to the right), *joint variance* (ξ^J) should be calculated as S_N samples along the axis perpendicular to the polarization axis (similar to the selected ions in *image labeling*) and $S_{O_{right}}$ ($S_{O_{left}}$) samples through the right (left) half image to search for the peak position of ξ^J, where the real correlated O^{2+} from the 3-body channel is located, in principle. However, since the selective average already provides the approximate range for the momenta or locations of O^{2+} in the real 3-body correlation and the accidental correlation from the 2-body channel, ξ^J only needs to be calculated as $S_{O_{right}}$ ($S_{O_{left}}$) samples in the neighborhood around the O^{2+} momenta determined by the selective average. As the correlated peaks on selective averages are no larger than 20×20 pixels, ξ^J is calculated as $S_{O_{right}}$ ($S_{O_{left}}$) samples in a 25×25-pixel box around these peaks, which is 50% larger than the largest peak found in selective averages and only occupies less than 8% of the

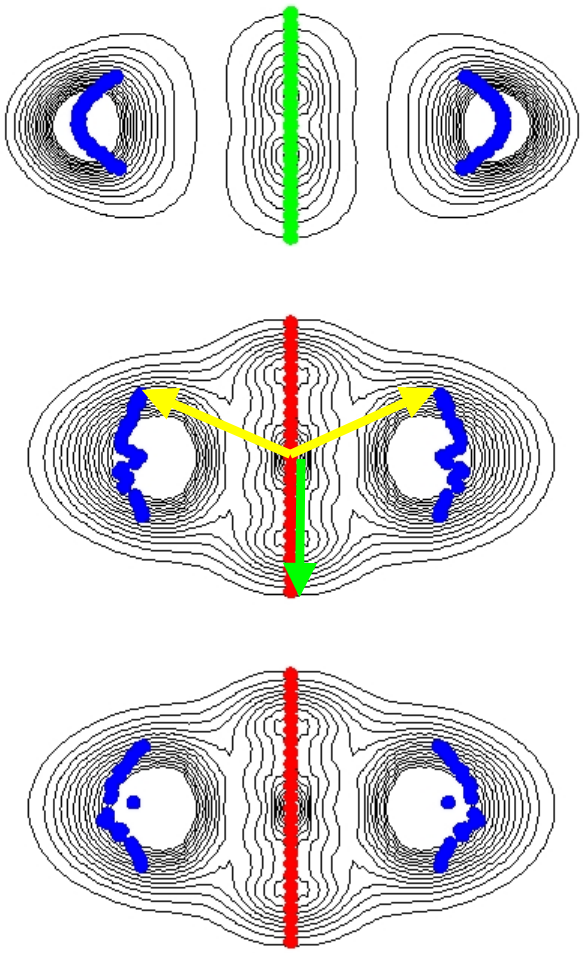

Figure 5.8: Contour plots of average images with both selected (middle group) and correlated (groups on both side) momentum vectors in three-body correlation marked. Top and center: CO_2 and NO_2 images with the locations (momenta) of correlated ions determined by selective average; bottom: NO_2 images with the locations (momenta) of correlated ions determined by joint variance. The green (red) circles mark the selected C^{2+} (N^{2+}) ions while the blue ones mark the correlated O^{2+} ions. The green and yellow arrows in the center plot indicate that the selected N^{2+} at the bottom of the middle group is correlated with O^{2+} at the top of both side groups. As the selected N^{2+} or C^{2+} is moved up along the center group, the corresponding O^{2+} on each side moves down along its arc.

half image, to make sure no 3-body correlation would be missed as well as to save computational time. The O^{2+} momenta of the 3-body channel are determined at the weighted centers of the ξ^J distributions in the 25×25-pixel boxes, and the explosion signal strengths are calculated by integrating ξ^J in a 3×3-pixel area at the weighted centers. These centers of the joint variance distribution are not necessarily at the same locations as the peaks in the selective averages. In fact, the centers of joint variance and peaks of selective average separate more as the bond angle gets closer to 180°, as shown in Fig. 5.8. The momenta of the real 3-body channel are thus taken to be at the weighted centers of joint variance. In the bottom plot of Fig. 5.8, it is obvious that the abrupt change of the momentum near $\theta_{CM} \sim 180°$ is reduced except at one point right at $\theta_{CM} = 180°$, where the signal strength of the 3-body explosion drops to almost zero, as shown in Fig. 5.9. For bond angles smaller than 150°, correlated O^{2+} momenta determined by both selective average and joint variance measurements actually overlap with each other (Fig. 5.8).

Explosion signal strengths measured by joint variance and coincidence imaging (triple-coincidence) at the momenta determined by joint variance along with double-coincidence for the two O^{2+} are shown in Fig. 5.9. While the double-coincidence points increase monotonically and triple-coincidence points stay roughly constant as θ_b approaches 180° from 140°, the joint variance points peak near $\theta_b = 140°$, which is fairly close to the equilibrium bond angle of NO_2 in its ground state ($\theta_{be} = 134°$). At the same time, data points from all three measurements follow similar trends for $\theta_b < 140°$. Since double- and triple-coincidence signals follow the same trend at $\theta_b < 140°$ (Fig. 5.9), this is consistent with that the signals come from the same 3-body channel

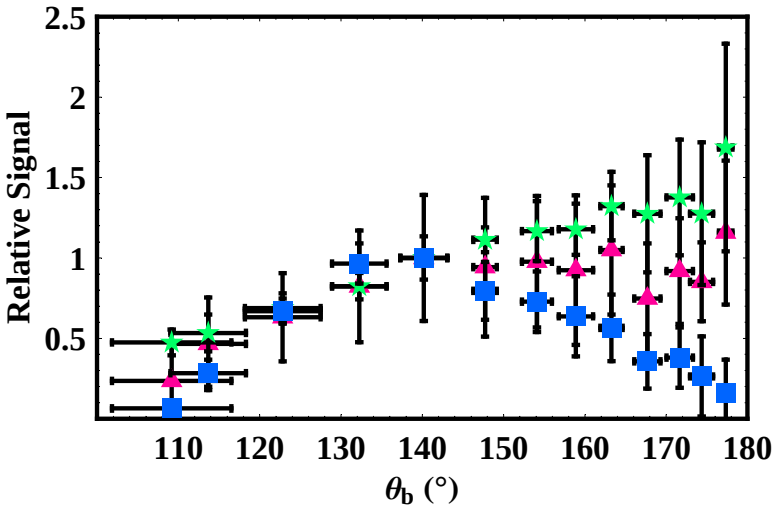

Figure 5.9: Explosion signal strength as a function of bond angle for NO_2^{6+} symmetric explosions initiate with $q_O = q_N = 2$ measured by joint variance (blue square), triple-coincidence (red triangle), at the selected N^{2+} momentum and correlated O^{2+} momenta determined by joint variance, along with double-coincidence (green star) at the O^{2+} momenta. The error bars are the standard deviation of seven experiments under the same conditions.

and there is no excess correlation from the 2-body channel to contaminate the triple-coincidence measurement. Thus, it is believable that the signal strength measured by triple-coincidence (Fig. 5.9) as well as the momenta determined by selective average (Fig. 5.8) for $\theta_b < 140°$ belong to the real 3-body explosion channel. Furthermore, as the momenta and relative signal strength determined by joint variance are essentially the same as those determined by selective average and triple-coincidence for $\theta_b < 140°$ (Figs. 5.8 and 5.9), the joint variance measurement is also believable. As the bond angle approaches 180°, the departure of the signal strength measured by double-coincidence from that measured by triple-coincidence (Fig. 5.9) confirms that there are additional O–O correlations (evidently from the 2-body channel) other than that due to the 3-body channel. The signal measured by triple-coincidence is

enhanced by the accidental coincidence from the 2-body channel as θ_b approaches 180°. The fact that joint variance emphasizes the existence of the N–O correlation in the triple-correlation and reduces the contribution from the false 2-body correlation, along with that the relative probabilities determined by joint variance and triple-coincidence as well as the momenta determined by joint variance and image labeling scale together at smaller bond angles ($< 140°$), gives credence to our believe that the probabilities and momenta determined by joint variance at larger angles are also valid.

Figure 5.10 shows how $|p_X|$ and $|p_Y|$ determined by *joint variance* for the correlated ions depend on the pre-explosion bond angle of the parent molecule. Although the data points still do not follow constant-R_C curves, the deviation near 180° is smaller than that in the result of *image labeling* (Fig. 5.6). In the same fashion as in the CO_2 case, the explosion energy ($\mathcal{E}_k$) and the initial molecular structure (R_C and θ_b) can be determined from the momenta of the ions and θ_{CM}. The bond length (R_C) and explosion energy ($\mathcal{E}_k$) as functions of bond angle are plotted in Fig. 5.11. The average R_C is 0.26 nm while R_C at the peak of explosion signal ($\theta_b = 140°$, Fig. 5.9) is 0.254 nm. As θ_b increases from about 110° to 180°, R_C ($\mathcal{E}_k$) increases (decreases) from 0.211 to 0.315 nm (71.3 to 46.6 eV) monotonically beyond the standard deviation of the measurement (Fig. 5.11), indicating that NO_2 appears to behave differently from CO_2 in the intense laser field even for the same 3-body explosion channel.

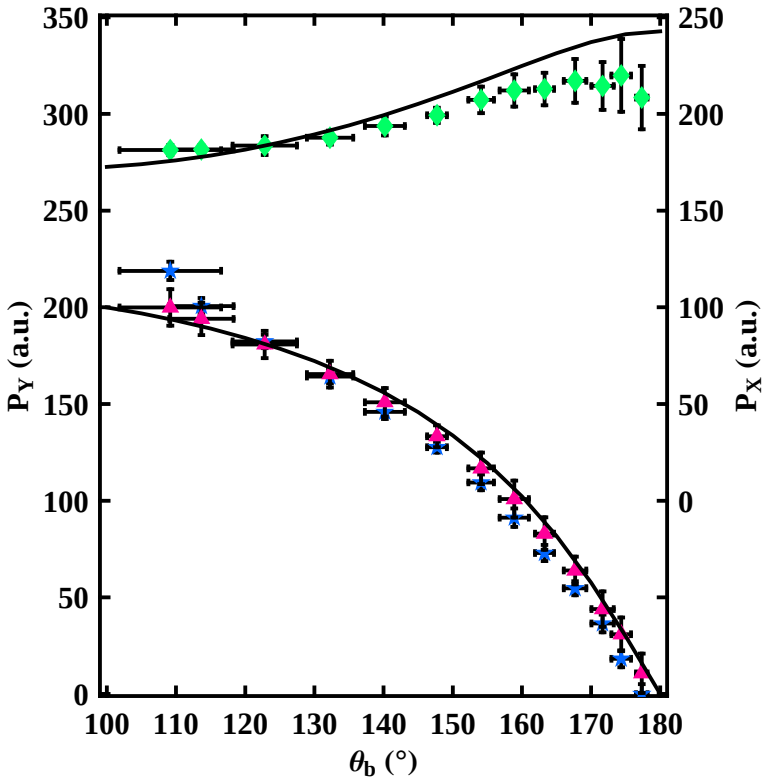

Figure 5.10: Momenta of the three charges ejected simultaneously as a function of the bond angle (θ_b) in the symmetric NO_2^{6+} Coulomb explosion channel determined by *joint variance*. The error bars represent the standard deviation in this determination over seven runs. The upper series of points (green diamonds) correspond to $|p_X|$ for O^{2+}; $|p_X|$ is virtually the same for the two groups of ions so only one point is plotted for each angle. The lower trace is $|p_Y|$ for N^{2+} (blue stars) and $2|p_Y|$ for O^{2+} (red triangles); p_Y is also the same for the two groups of O^{2+} ions. The solid curves represent the calculated momenta assuming R_C equals 0.26 nm (see App. D).

5.1.1.3 Large-Amplitude Vibration

The explosion signal strength (relative probability) of CO_2 and NO_2 (Figs. 5.4 and 5.9) shows large-amplitude vibration. We will compare this observation to the bending vibrational amplitude at R_e of the triatomic molecules. The vibrational amplitude ($\Delta\theta_b$) can be estimated from $kR_e^2\Delta\theta_b^2/2 = (v + 1/2)hc\nu_2$ assuming harmonic oscillation, where v is the quantum number of the energy level, k and ν_2

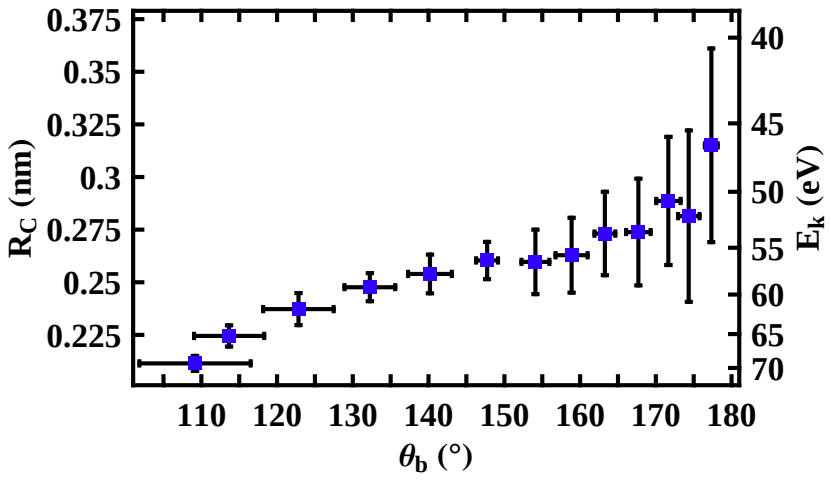

Figure 5.11: Bond length and explosion energy as functions of bond angle for NO_2^{6+} symmetric explosions initiate with $q_O = q_N = 2$ measured by *joint variance*. The error bars are the standard deviation of seven experiments under the same conditions.

are the force and vibrational constants for the bending motion at R_e, h is Plank constant, and c is the speed of light. The constants of CO_2 (NO_2) are $k = 57$ N/m (152 N/m) and $\nu_2 = 667$ cm^{-1} (750 cm^{-1}) at $R_e = 0.116$ nm (0.119 nm) [131].

Therefore, for CO_2 in the ground state ($v = 0$), $\Delta\theta_b$ is 7.5°. In classical harmonic oscillation, the molecule will spend most of its time near the end points or turning points of its oscillation. Thus, the most probable location of the molecule in the bending vibration should be at $\theta_b = 172.5°$. This value is in very good agreement with Fig. 5.4, where the measured signal strength peaks near $\theta_b \simeq 173°$. The maximum observed bending (minimum θ_b at about 145°) corresponds to $v \sim 10$, or $E_v = (v+1/2)hc\nu_2 \sim 0.9$ eV. For NO_2 in the ground state ($v = 0$), $\Delta\theta_b = 4.8°$, thus the peak signal should appear near $\theta_b \simeq 129.2$ and 138.8°, which is in very good agreement with the joint variance measurement – the measured signal strength peaks near $\theta_b \simeq 140°$ (Fig. 5.9). The reason we do not observe two peaks at both 129.2

and 138.8° is probably due to the angular resolution in the measurement is not high enough. The maximum observed bending ($\sim 110°$) at $\theta_b < \theta_{be} = 134°$ corresponds to $v \sim 12$ ($E_v \sim 1.2$ eV), and the maximum bending ($\sim 170°$) at $\theta_b > \theta_{be}$ corresponds to $v \sim 25$ ($E_v \sim 2.4$ eV). There are three possible reasons for this asymmetric vibrational amplitude on the two sides of the equilibrium bond angle (θ_{be}). The first is that the anharmonic term becomes more significant as the bond angle approaches 180° so that this simple model for vibrational energy assuming harmonic oscillation is not valid any more. The second is that the laser field distorted the vibrational motion, which made it easier to increase than to decrease the bond angle. A third reason could be that the distortion on the explosion signal as a function of bond angle caused by the 2-body channel was not corrected completely by joint variance. The real signal at $\theta_b > 150°$ might be smaller than what was measured.

The observed explosion signal as a function of bond angle for both CO_2 and NO_2 shows large-amplitude vibrations ($v \gtrsim 10$ and $E_v \gtrsim 1$ eV) beyond the Maxwell-Boltzmann distribution ($\propto e^{-E/(kT)}$ with E is the energy level, k is the Boltzmann constant and T is the temperature) at the room temperature, which is consistent with previous observations [56, 58, 60, 61]. On the other hand, as shown in Fig. 1 of Ref. [132], the molecular vibrational energy of NO_2 in the ground state shows an asymmetric potential well, where the energies at $\theta_b = 110°$ and 180° are equal and the minimum appears at $\theta_{be} = 134°$. This is consistent with our observed signal distribution of NO_2, which peaks near 140° and extends to 110° and 180°. This evidence, along with the fact that the peaks of the explosion signal distributions for both CO_2 and NO_2 appear near their equilibrium bond angles, shows that the

molecular vibrational energy in the laser field has similar minimum and potential well structure as in the ground state of the neutral molecule, at least for the 6-electron explosion channels of CO_2 and NO_2.

At the same time, the experimental results show that NO_2 explosion energies decrease monotonically by more than 25% from the smallest to the largest bond angles observed (Fig. 5.11), in contrast to CO_2, which exhibits explosion energies that are nearly independent of bond angle (Fig. 5.3). This observation is different from the result of CS_2 measured by a position-sensitive detector [65], where the explosion energy increases as the bond angle increases. The explosion energy as a function of the bond angle will be analyzed with two models in the next section.

5.1.2 Explosion Energy Analysis

In this section, the measured explosion energies of the 6-electron explosion channels for CO_2 and NO_2 are compared to the calculations in the field-ionization (R_C) and electron-screening models.

5.1.2.1 Triatomic 2-D Field Ionization

To compare the experimental results to the field-ionization model, the one-dimensional diatomic field-ionization model (Sec. 2.1.1) is extended to 2-dimension with three charge centers. The coordinate system employed is shown in Fig. 5.12. The center atom (q_3) is set at the origin ($r_3 = 0$), and the line between the outer atoms q_1 and q_2 is parallel to the x-axis as well as the laser field ($\vec{E}$), which is pointing

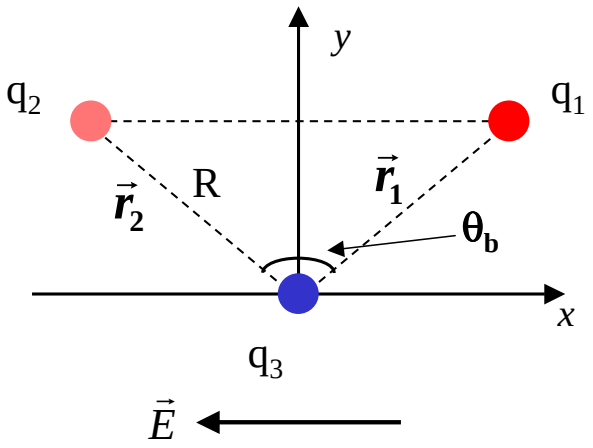

Figure 5.12: Coordinate system employed in triatomic 2-D field ionization calculation.

to the $-x$ direction. The vectors $\vec{r}_1$ and $\vec{r}_2$ are pointing from the origin (center atom) to the outer atoms, and their lengths are the bond length ($r_1 = r_2 = R$), as the symmetric configuration is considered. The angle between the vectors $\vec{r}_1$ and $\vec{r}_2$ is the bond angle (θ_b).

Therefore, the 2-D potential energy (adapted from Eq. 2.3) is given by

$$\begin{aligned} V(x,y) &= -\frac{Kq_1e^2}{\sqrt{(x-R\sin(\theta_b/2))^2+(y-R\cos(\theta_b/2))^2+s^2}} - \frac{Kq_3e^2}{\sqrt{x^2+y^2+s^2}} \\ &\quad -\frac{Kq_2e^2}{\sqrt{(x+R\sin(\theta_b/2))^2+(y-R\cos(\theta_b/2))^2+s^2}} + eEx, \end{aligned} \tag{5.2}$$

where e is the elementary charge, q_ie with i = 1,2,3 are the charges of the three nuclei, E is the laser field strength, and s is the smoothing parameter to remove the singularity of the Coulomb potential and make the two-dimensional calculation agree with measured R_C and ionization potentials [73, 76]. The adapted electron

Table 5.1: Ionization potentials of H and the first two ionization stages of C, N, and O atoms in eV [133], where $I_p^{(q)}$ is the ionization potential from $X^{(q-1)+} \rightarrow X^{q+}$.

q	H	C	N	O
1	13.6	11.262	14.536	13.619
2		24.386	29.604	35.122

energy levels of the charge-resonance states (Eq. 2.4) are given by

$$\begin{aligned}
\varepsilon_+ &= \varepsilon_1 = -I_{p1} - K\left(\frac{q_3e^2}{R} + \frac{q_2e^2}{2R\sin(\theta_b/2)}\right) + \zeta eER\sin(\theta_b/2), \\
\varepsilon_- &= \varepsilon_2 = -I_{p2} - K\left(\frac{q_3e^2}{R} + \frac{q_1e^2}{2R\sin(\theta_b/2)}\right) - \zeta eER\sin(\theta_b/2), \qquad (5.3) \\
\varepsilon_c &= \varepsilon_3 = -I_{p3} - K\left(\frac{q_1e^2}{R} + \frac{q_2e^2}{R}\right),
\end{aligned}$$

where the first term (I_{pi}) is the ionization potential for $X^{(q_i-1)+} \rightarrow X^{q_i+}$ (Table 5.1), the second and third terms lowers the energy levels because of the presence of the other two positive charge centers and the fourth term in ε_+ and ε_- accounts for shifting of the energy level in the presence of the laser field. The $\sin(\theta_b/2)$ in the fourth term accounts for the classical Stark shift in an external field. However, without a detailed quantum calculation, it is not known how this level will shift due to the overlap between the electron wave functions at the three charge centers with the presence of the laser field. Thus, an adjustable parameter, ζ, is employed with values between 0 (no shift) and 1 (charge resonant shift [73, 75, 107]). As a simple and convenient starting point, ζ is assumed to be independent of the bond angle.

As θ_b was changed from 100° to 180°, R_C for enhanced ionization was determined via two different electron pathways. The first, shown in the upper-left panel of Fig. 5.13, is through the saddle points of the potential, which will not be along the

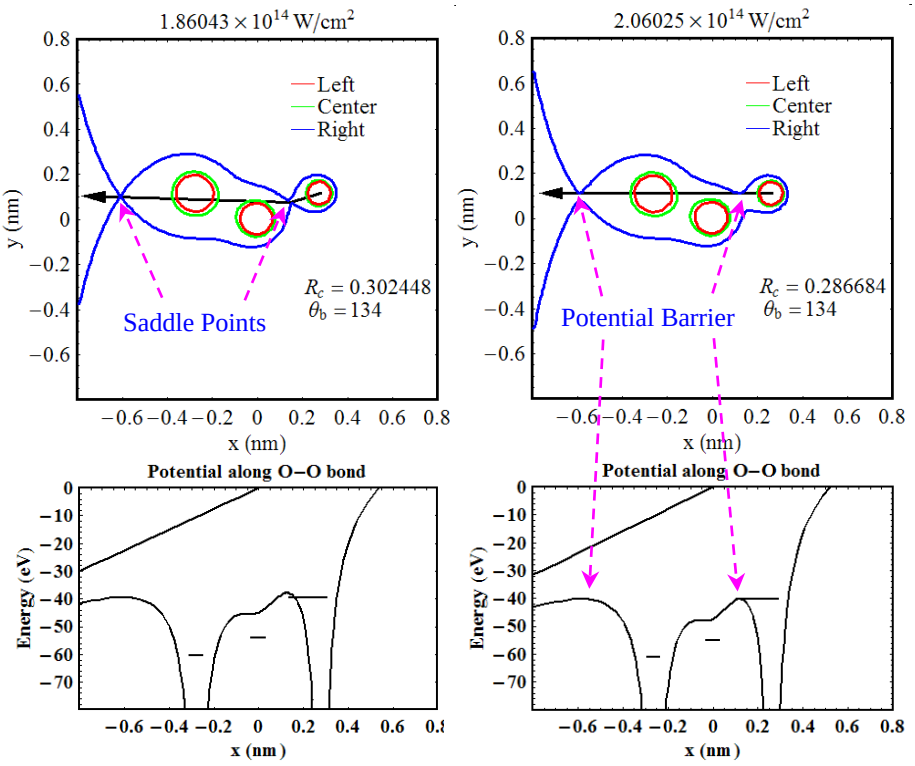

Figure 5.13: Two over-the-barrier ionization pathways for a triatomic ion at $\theta_b = 134°$: saddle-point ionization (upper left) and quasi-diatomic, parallel to the polarization axis and across the O–O barrier (upper right). Arrows in the upper plots indicate the electron pathways. The lower plots are the corresponding potential curves along and centered at the O–O axis. The contours in the upper plots and the short line segments in the lower plots indicate the electron energy levels in three potential wells. The right plots correspond to 5% reduction in R_C relative to the left but at a cost of a 10% increase in ionization intensity. Other parameters in the calculation are $\zeta = 1.0$, $s = 0.01$, $q_1 = q_2 = q_3 = 2$, and $I_p = 35.1$ eV which is the ionization potential for O^+.

polarization axis when $\theta_b \neq 180°$. As the potentials at the inner and outer saddle points equal to the electron energy level (ε_+) in the upper (right) well (blue contour), the ionization takes place and R_C, as well as E_{ia} – the ionization field strength, are found. At this time, ε_+ is still lower than the potential barriers along the O–O bond, as shown in the lower-left panel of Fig. 5.13. The second is across the O–O barrier, parallel to the polarization axis regardless of the value of θ_b (right panels in

Fig. 5.13). The ionization takes place and R_C is found as the potentials at the inner and outer barriers along the O–O axis equal to the electron energy level (ε_+) in the upper (right) well, similar to the diatomic case discussed in Sec. 2.1.1. The latter pathway, a quasi-diatomic pathway, typically requires higher ionization intensities ($I_{ia} = c\epsilon_0 E_{ia}^2/2$) and yields smaller R_C's relative to the saddle-point pathway.

In general, R_C increases as ζ increases, since larger ζ increases the energy shift. Figure 5.14 shows the R_C and the ionization intensity (I_{ia}) curves as functions of θ_b calculated with the quasi-diatomic and saddle-point pathways for a series of ζ's between 0 and 1. The R_C curves are almost equally spaced, and increase (decrease) as θ_b increases for the quasi-diatomic (saddle-point) pathway. The ionization intensity decreases as θ_b increases for both pathways. Both R_C and I_{ia} curves for the quasi-diatomic pathway have a larger curvature than those for the saddle-point pathway.

At the same time, R_C decreases as s increases. A smaller s makes the wells deeper. The curvature, however, is nearly independent of both ζ and s. Figure 5.15 shows R_C and I_{ia} curves as functions of θ_b calculated with the quasi-diatomic and saddle-point pathways at a series of s's between 0 and 0.05 nm. The R_C curves increase (decrease) as θ_b increases for the quasi-diatomic (saddle-point) pathway. The ionization intensity decreases as θ_b increases for both pathways. As $V(x, y)$ (Eq. 5.2) needs to remain physical – the wells must support the bound states, for example – s is restricted to certain values. At the lower end, s is bounded by 0; below about 0.01 nm, however, s no longer influences the value of R_C in both pathways. For an upper limit, $s = s_{\max}$ is determined when one of the three energy levels (Eq.

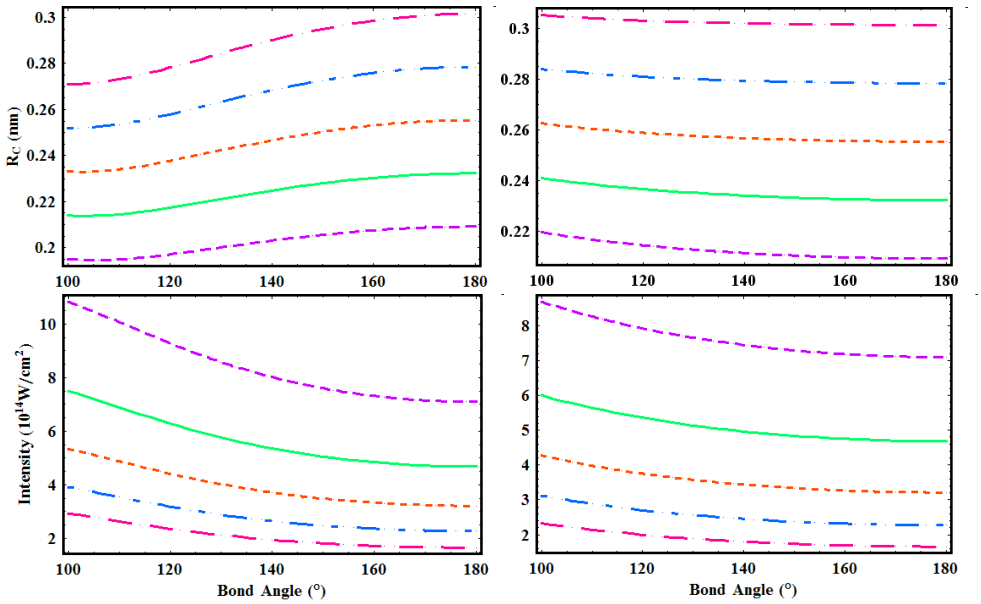

Figure 5.14: Calculated R_C (upper plots) and I_{ia} (lower plots) as functions of θ_b (Eqs. 5.2 and 5.3) with $\zeta = 0$ (violet, dashed), 0.25 (green, solid), 0.5 (orange, short-dashed), 0.75 (blue, dot-dash), 1.0 (red, long-dashed) for the quasi-diatomic (left panels) and the saddle-point (right panels) pathways. Other parameters in the calculation are $s = 0.01$ nm, $q_1 = q_2 = q_3 = 2$, and $I_p = 35.1$ eV which is the ionization potential for O^+.

5.3) is at the bottom of a well as shown in Fig. 5.16; shifts proportional to $\pm ER$ ($\zeta = 1.0$, with the + sign corresponding to the uphill well and the − sign to the downhill well) lead to $s \leq 0.07$ nm for $I_p = 35.1$ eV, the ionization potential for O^+. As ζ decreases, $s_{\max}$ also decreases.

In order to make a quantitative comparison with the experiment results, the adjustable parameters of the model need to be determined first. In the enhanced-ionization model, the transition moment between the charge-resonance states is proportional to $R/2$ for diatomics [107, 108], while this value in linear H_3^{2+} and H_3^+ was calculated to be $\sim 0.4R$ where R is the distance between two outer H [93]. Thus, if the charge-resonance is assumed to account for the shift of the energy levels

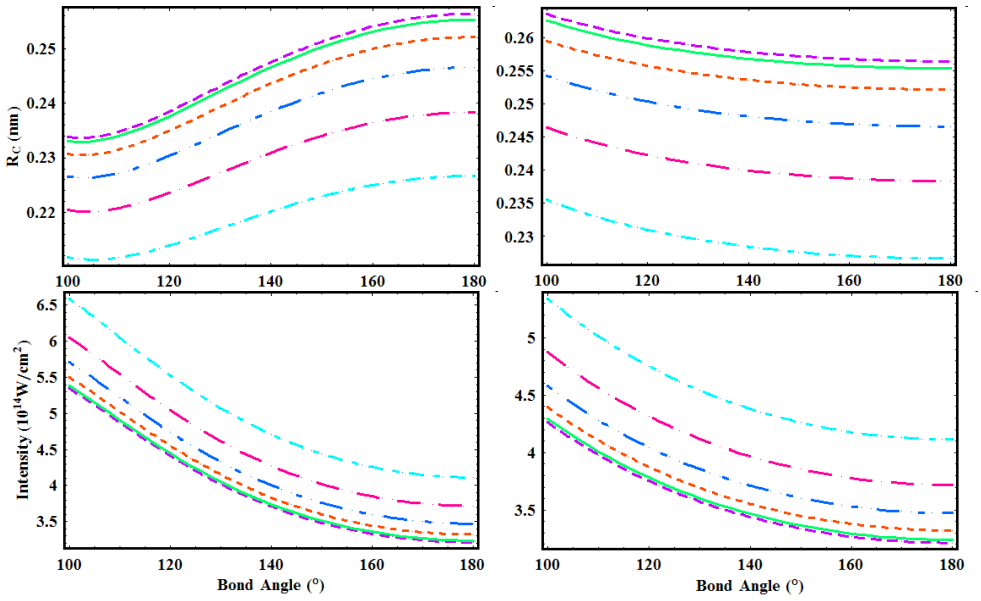

Figure 5.15: Calculated R_C (upper plots) and I_{ia} (lower plots) as functions of θ_b (Eqs. 5.2 and 5.3) with $s = 0$ (violet, dashed), 0.01 (green, solid), 0.02 (orange, short-dashed), 0.03 (blue, dot-long-dash), 0.04 (red, long-dashed), 0.05 (light blue, dot-dash) for the quasi-diatomic (left panels) and the saddle-point (right panels) pathways. Other parameters in the calculation are $\zeta = 0.5$, $q_1 = q_2 = q_3 = 2$, and $I_p = 35.1$ eV which is the ionization potential for O^+.

in Eq. 5.3, ζ should take values between 0.5 and 0.8. The smoothing parameter has been employed in 1-D and 2-D quantum calculations for the enhanced ionization [73, 74, 76, 93, 96], and the value was taken between 0.5 and 2 a.u. (0.03 – 0.1 nm) to match the 3-D results. Therefore, the lower limit of s is taken as 0.03 nm, and the upper limit is the physical limit of s (Fig. 5.16), 0.06 – 0.08 nm depending on ζ and I_p.

For CO_2, in our 2-D field-ionization model, if the ionization potential is assumed to be 13.614 eV for O ($q = 1$, Table 5.1), the lower limit of R_C is calculated to be ~ 0.23 nm at $\theta_b = 180°$ with $\zeta = 0$ and $s = 0.06$ nm for both saddle-point and

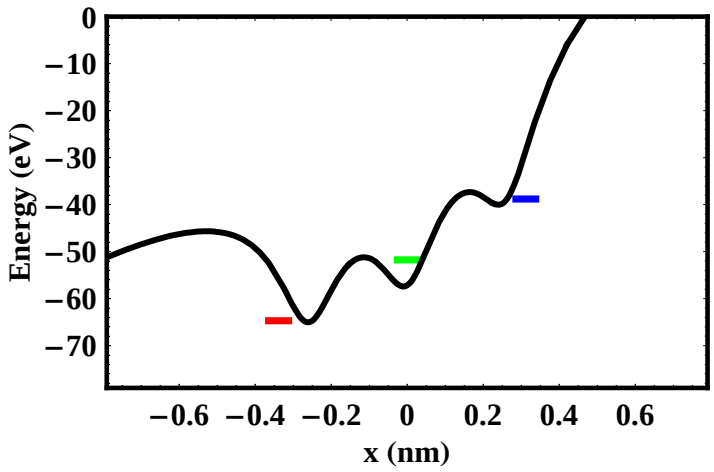

Figure 5.16: Extreme value of the smoothing parameter. The potential structure at the upper limit of s, 0.08 nm for $I_p = 35.1$ eV, $R = 0.26$ nm, and $\zeta = 1.0$ at an intensity of 3.3×10^{14} W/cm^2. The short line segments indicate the energy level of the bound electron in each well. In this example, the bottom of the left potential well coincides with the energy level of the electron.

quasi-diatomic pathways, which is still larger than the experimental value (0.215 nm). At the same time, R_C's predicted with C ($I_p = 11.264$ eV and $q = 1$) and C^+ ($I_p = 24.376$ eV and $q = 2$) are even larger than the one predicted with O. Consequently, the best agreement between theory and experiment for R_C is associated with ionizing O^+ ($I_p = 35.146$ eV), which also agrees with the electron being removed from the upper potential well instead of from the middle well. Evidently, since R_C for CO_2^+ is larger than that for CO_2^{3+}, the first three electrons must be removed before the appropriate R_C is reached or R_C is not determined by this simple one-electron model. Similarly, for NO_2, if the ionization potential is assumed to be 13.614 eV for O, the lower limit of R_C is calculated to be ~ 0.26 and 0.27 nm at $\theta_b = 140°$ with $\zeta = 0.5$ and $s = 0.08$ nm for saddle-point and quasi-diatomic pathways, respectively, which are larger than the experimental value (0.254 nm).

Consequently, the enhanced ionization of NO_2 also appears to be associated with ionizing O^+.

The model curves for both pathways are shown in Fig. 5.17 for the specific values of s and ζ given in the figure caption. These s and ζ produce values for R_C that matched the measured values at $\theta_b = 180°$ for CO_2 and $\theta_b = 140°$ for NO_2. This choice is not unique. While different choices would produce different curves, the new curves would have nearly the same contour as those shown – the slop of the model curve $R_C(\theta_b)$ for either pathway characterized by $\Delta = |R_C(110°) - R_C(180°)|/R_C(180°)$ varies between 0.02 and 0.1 within the allowed range ($0 \leq \zeta \leq 1$ and $0 \leq s \leq s_{\max}$), regardless of the values of R_C predicted. If it is constrained that the predicted R_C needs to match with the measured values, the variation of Δ is only about 0.02.

As shown in Fig. 5.17, the model curves $R_C(\theta_b)$ with the same I_p and ζ give a relatively reasonable match within the standard deviations to both CO_2 and NO_2 data at bond angles larger than 140°. This may be an indication that the enhanced ionization behaves roughly the same way in both systems for large bond angles. However, it is also interesting to note that while the curves generated by both ionization pathways are consistent with CO_2 observations, which is consistent with the fact that these two pathways do not differ from each other much at bond angles close to 180°, neither pathway is consistent with all the NO_2 data points – the curvature is wrong. The saddle-point ionization, which might seem to be the more plausible pathway, predicts R_C should increase slightly as θ_b decreases, but the measured R_C actually decreases as θ_b decreases (Fig. 5.17). Ionization along the

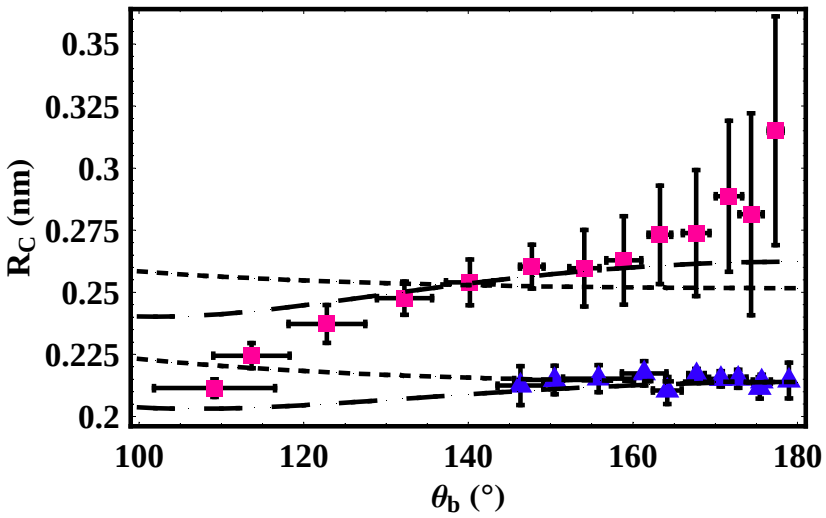

Figure 5.17: Experimental values of $R_C(\theta_b)$ for CO_2^{6+} (blue triangles) and NO_2^{6+} (red squares) explosions taken from Figs. 5.3 and 5.11. The R_C-model curves with I_p = 35.146 eV, $q = 2$, and $\zeta = 0.8$ for both saddle-point and quasi-diatomic pathways are represented by the short-dashed and dashed curves respectively. For saddle-point ionization s = 0.074 nm (0.055 nm) for CO_2 (NO_2) while for quasi-diatomic ionization s = 0.074 (0.046) nm for CO_2 (NO_2).

quasi-diatomic pathway predicts the correct sign of the curvature. Nevertheless, this curve diverges from the data points at small bond angles for NO_2 by more than one standard deviation. It needs to be emphasized that a different choice for ζ and s, or even I_p, in the acceptable range will not change the slop of $R_C(\theta_b)$ (Δ) to more than 10%, which is by no means able to account for the observed variation ($\gtrsim 25\%$) of NO_2 data between 110° and 180°.

In the calculation described above, we assumed ζ to be constant for all the bond angles. However, the energy shift of the electron's state due to the overlap between the electrons' wave functions at the three charge centers could change as the bond angle changes. In the charge-resonance point of view, this shift corresponds to the energy difference between the charge-resonance states in a laser field. The

charge-resonance states and their energy levels in a triatomic ion could very well depend on the bond angle. As shown in Figs. 5.11 and 5.17, R_C decreases as θ_b decreases for NO_2 data points. A smaller R_C indicates a smaller ζ, as we mentioned before (Fig. 5.14). Thus, it appears to be that, at least for NO_2, the energy shift between the charge-resonance states (ζ) decreases as θ_b decreases. We recall that the value of ζ for H_2 from quantum calculations [107, 108] as well as other diatomics [70] from classical calculations (see Sec. 2.1.1) is $\zeta_{di} = 0.5$, which is smaller than that calculated for linear H_3 molecular ion ($\zeta_{tri} = 0.8$) [93] – the only triatomic charge-resonance calculation of which we are aware. Therefore, one might imagine that the smaller ζ (than $\zeta_{tri} = 0.8$) at small bond angles for NO_2 could be related to a tendency for the charge-resonance states to become diatomic-like as θ_b decreases to 110° and as R_C approaches 0.21 nm – the value of NO diatomic explosions [47]. A possible explanation of this tendency is that the triatomic charge-resonance states (including the electron wave functions at all three charge centers) becomes spatially restricted (only charge-resonance between adjacent nuclei – N and O) as the bond angle decreases. In linear cases, the electron can move from one end of the molecule to the other directly – triatomic charge-resonance. However, in bent configurations, the motion of the electron may occur in two steps – from one end nucleus to the central nucleus to the other end – which establishes charge resonance between adjacent nuclei.

To quantify the variation of ζ, we keep a value of 0.8 at $\theta_b = 140°$, which we have used to match our constant-ζ calculation to the measurement, and assume $\zeta = \zeta_{di} = 0.5$ at $\theta_b = 110°$, where R_C approaches its diatomic value. Furthermore,

for simplicity, we assume ζ varies as a linear function of $\sin(\theta_b/2)$, same way as the length of the molecule varies (Eq. 5.3). Therefore,

$$\zeta(\theta_b) = a + b\sin(\theta_b/2). \tag{5.4}$$

With $a = -1.539$ and $b = 2.489$, $\zeta(110^\circ) = 0.5$ and $\zeta(140^\circ) = 0.8$ for NO_2, which gives $\zeta(180^\circ) = 0.95$. For CO_2, the value of a is taken to be -1.639 to match the data points, which gives $\zeta(180^\circ) = 0.85$ and $\zeta(145^\circ) = 0.73$. Inserting Eq. 5.4 into Eq. 5.3, $R_C - \theta_b$ curves were generated through the saddle-point pathway (Page 94) – the electron moving from one oxygen to the nitrogen to the other oxygen, at small bond angles, instead of directly between two oxygen nuclei, as discussed in the last paragraph. The curves are shown in Fig. 5.18. This method works better ($\chi^2 = 0.0033$ nm^2 is smaller) than the constant-ζ curves ($\chi^2 = 0.0107$ nm^2 for the saddle-point pathway and $\chi^2 = 0.0055$ nm^2 for the quasi-diatomic pathway, see Fig. 5.17) for NO_2 and implies that electron dynamics becomes more diatomic-like as the bond angle decreases, where χ^2, the sum of the squares of the deviations between the measured and calculated R_C, is defined as

$$\chi^2 = \sum_{\theta_b} \Big(R_{C,\,\mathrm{EXP}}(\theta_b) - R_{C,\,\mathrm{CAL}}(\theta_b) \Big)^2. \tag{5.5}$$

The model curve is consistent with all the data points except the two end points at $\theta_b \sim 110^\circ$ and 180°. At the same time, although the curvature of the model curve for CO_2 is slightly larger than the data curve, the new curve falls within the uncertainty of all the CO_2 data points.

Although this $R_C - \zeta(\theta_b)$ model gives smaller χ^2 than the constant-ζ calculation, because the variation of ζ is taken into account, the description of the $\zeta(\theta_b)$

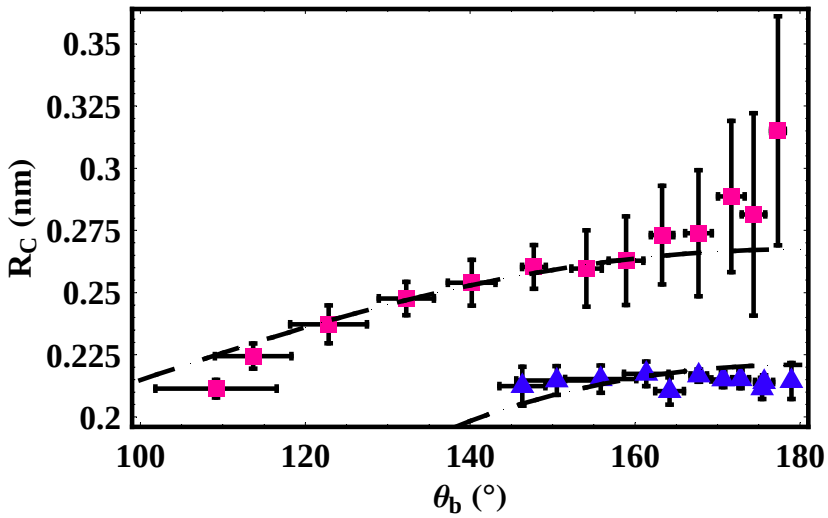

Figure 5.18: Experimental values of $R_C(\theta_b)$ for CO_2^{6+} (blue triangles) and NO_2^{6+} (red squares) explosions taken from Figs. 5.3 and 5.11 and the saddle-point $R_C - \zeta(\theta_b)$-model curves with I_p = 35.146 eV, q = 2, and $\zeta = a + b\sin(\theta_b/2)$ with b = 2.489 and a = -1.639 (-1.539) for CO_2 (NO_2). The smoothing parameter is s = 0.074 nm (0.055 nm) for CO_2 (NO_2).

function (Eq. 5.4) is a bit arbitrary and without much theoretical support. First, the values for ζ for diatomic and linear triatomic charge-resonance states – ζ_{di} = 0.5 and ζ_{tri} = 0.8 – were calculated from H_2^+ and H_3^{2+}, which almost certainly will not reflect all of the physics of multi-electron molecular ions. Second, the expression of $\zeta(\theta_b)$ (Eq. 5.4) is simplified, where the difference between CO_2 and NO_2 is only accounted for by a shift in the constant a. A detailed quantum calculation is necessary to determine how ζ depends on θ_b. However, if we assume Eq. 5.4 reflects some of the physics, a fit of the R_C curve to the data points with a and b as fit parameters could provide some information about how the energy shift changes as θ_b changes. For example, we can see that the curvature of the model curve for CO_2 (NO_2) is too large (small) (Fig. 5.18). The curvature of the NO_2 curve can be

increased to get a better match to the data points by raising $\zeta(\theta_b = 180°)$ and/or lowering $\zeta(\theta_b = 110°)$. This implies that the energy shift of the states in NO_2 at large (small) bond angles could be larger (smaller) than that in H_3 (H_2). Similar analysis for CO_2 would have the opposite implication.

5.1.2.2 Static Screening

Besides the enhanced-ionization (R_C) model, the explosion energy can also be predicted by the electron-screening model (Sec. 2.1.2). The downside of the dynamic-screening (DS) model is a more involved set of calculations. As will be shown below, however, that the DS-model gives the same explosion energy as the single-parameter R_C-model suggests that screening might be characterizable with a single parameter as well. Specifically, a charge defect (σ) [62] may be introduced such that the potential at the critical ionization stage is set by an effective charge, $q^{eff} \equiv q - \sigma$. Assuming σ depends only on q, it can be derived by equating the Coulomb potential energies at R_C with full charge q with that for R_e with effective charge q^{eff},

$$\begin{aligned} \mathcal{E}_C(R_C, q) &= \frac{2Kq^2e^2}{R_C} + \frac{Kq^2e^2}{2R_C\sin(\theta_b/2)}, \\ \mathcal{E}_C(R_e, q-\sigma) &= \frac{2K(q-\sigma)^2e^2}{R_e} + \frac{K(q-\sigma)^2e^2}{2R_e\sin(\theta_b/2)}, \\ \mathcal{E}_C(R_C, q) &= \mathcal{E}_C(R_e, q-\sigma). \end{aligned} \tag{5.6}$$

Then, σ can be defined as

$$\sigma \equiv q(1 - \sqrt{R_e/R_C}), \qquad R_C = \frac{R_e q^2}{(q-\sigma)^2}. \tag{5.7}$$

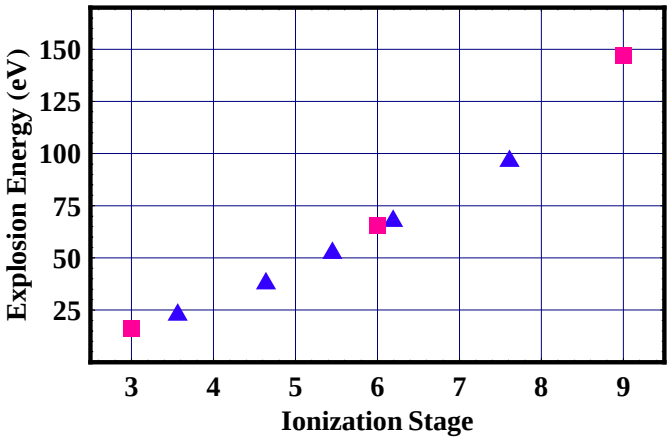

Figure 5.19: A comparison between the linear explosion energies for CO_2^{Z+} ($Z = 3-9$) calculated by the dynamic screening model of Ref. [82] (blue triangles) and by q^{eff} (red squares). The experimental value for R_C (= 0.215) nm measured for the 6-electron channel along with $R_e = 0.116$ nm were used to determine σ and q^{eff} (Eqs. 5.6 and 5.7).

Figure 5.19 shows that this mapping of R_C onto σ leads to the same explosion energies for symmetric ionization stages between 3 and 9 for linear CO_2 as calculated by the hydrodynamic equations of the DS-model [82] (Sec. 2.1.2). This surprisingly simple result suggests that a quasi-static electron distribution that envelopes the nuclei for early times during the explosion captures the essence of the dynamics, which would explain why an R_C concept works so well. What remains to be done, however, is to look at the behavior of σ as a function of bond angle and to determine if the measured σ is in agreement with the theory for 3-atom systems.

For simplicity, a static electron distribution is employed in the calculation. Its shape and density do not vary in time – *Static Screening* (SS). The energy deficit in the process of dissociative ionization is assumed to be solely determined by the Coulomb potential between electrons and the three ions at their initial bond length

and bond angle. The energy deficit, or the charge defect derived from the energy deficit, can be used to compare with the experimental measurement. To determine the angular behavior of $\mathcal{E}_C$ in the SS-model, the energy deficit is defined as,

$$\mathcal{E}_D \equiv \sum_{i=1}^{3} \int_A \frac{K\rho(x,y)q_i e^2 \mathrm{d}x\mathrm{d}y}{\sqrt{(x_i-x)^2+(y_i-y)^2+s^2}}, \tag{5.8}$$

the interaction energy between the positive ions (x_i, y_i) and the cloud of electrons represented by a 2-dimensional distribution $\rho(x,y)$ confined to an area A with the x-axis along the laser polarization direction. The smoothing parameter s is introduced to remove the singularity of the Coulomb potential. Since $\mathcal{E}_D$ is equal to the difference between Coulomb potential energies calculated at R_e with $q_i = 2$ and with $q_i^{eff} = q_i - \sigma$, we have

$$\begin{aligned} \mathcal{E}_D &= \mathcal{E}_C(R_e,q) - \mathcal{E}_C(R_e,q-\sigma), \\ &= \left(\frac{2Kq^2e^2}{R_e} + \frac{Kq^2e^2}{2R_e\sin(\theta_b/2)}\right) - \left(\frac{2K(q-\sigma)^2e^2}{R_e} + \frac{K(q-\sigma)^2e^2}{2R_e\sin(\theta_b/2)}\right), \end{aligned} \tag{5.9}$$

σ can be extracted once $\mathcal{E}_D$ is determined,

$$\sigma = q - \sqrt{q^2 - \frac{2R_e\mathcal{E}_D\sin(\theta_b/2)}{Ke^2(1+4\sin(\theta_b/2))}}. \tag{5.10}$$

Then, σ or $\mathcal{E}_C(R_e, q-\sigma)$ can be compared with the measured kinetic energy $\mathcal{E}_k$,

$$\mathcal{E}_k = \mathcal{E}_C(R_e,q-\sigma) = \mathcal{E}_C(R_e,q) - \mathcal{E}_D. \tag{5.11}$$

The positions of the ions (x_i, y_i) in Eq. 5.8 are set so that the CO or NO bond length in CO_2 or NO_2 is the ground state R_e; the bond angle (θ_b) is allowed to vary so that the angular dependence of $\mathcal{E}_D$ or σ can be determined. The distribution

(ρ), which is due to electrons being liberated at different intensities throughout the pulse, is approximated by a two-dimensional Gaussian function,

$$\rho(x, y) = \rho_0 e^{-x^2/x_0^2 - y^2/y_0^2}. \tag{5.12}$$

It is centered at the center of mass of the triatomic molecule, which is also the origin of the coordinate system (same as the one shown in Fig. D.1). The line between the two outer atoms is parallel to the x-axis as well as the laser polarization axis. The strength of the distribution $\rho_0 = Q_{el}/(\pi x_0 y_0)$ is determined by $Q_{el} = \int_A \rho(x, y)\mathrm{d}x\mathrm{d}y$. The area A is a $4x_0 \times 4y_0$ rectangle, out of which the Gaussian distribution $\rho(x, y)$ drops to less than 2% of its peak value. The total number of electrons in the distribution, Q_{el}, is bounded by 6, the total number of electrons freed from the system and constrained to be the same for CO_2 and NO_2, since the free electrons should behave approximately the same in both systems in the presence of the laser field along with three positive charge centers.

As Eq. 5.12 is inserted into Eqs. 5.8 and 5.10, it is obvious that $\mathcal{E}_D$ as well as σ are functions of x_0, y_0, Q_{el}, and s. In general, $\mathcal{E}_D(\theta_b)$ or $\sigma(\theta_b)$ decreases with increasing s. In contrast to the R_C model, s has a significant effect on the contour of the curve, bending the curve more as s decreases. At the same time, as x_0 or y_0 increases, $\sigma(\theta_b)$ decreases, and the curve bends more as y_0 decreases (Fig. 5.20).

Again, in order to make quantitative comparison with the experiment results, the adjustable parameters of the model need to be determined first. The size of the electron distribution is set by kinematics – the oscillation radius of the electrons, α_0, due to the ponderomotive force in the field along the polarization axis (x-axis),

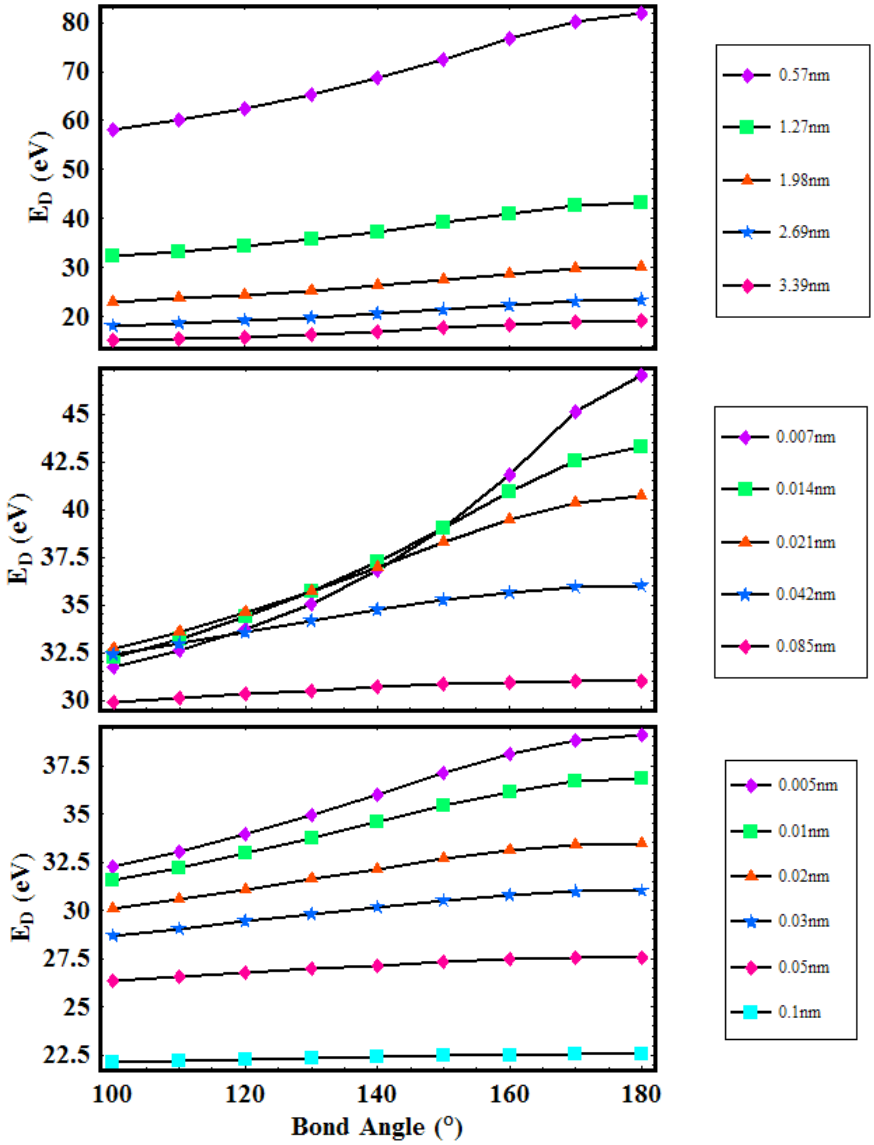

Figure 5.20: Energy deficit ($\mathcal{E}_D$) as a function of θ_b calculated by SS-model ($Q_{el} = 1$). Top: $x_0 = 0.57$, 1.27, 1.98, 2.69, 3.39 nm with $y_0 = 0.014$ nm and $s = 0.02$ nm; middle: $y_0 = 0.007$, 0.014, 0.021, 0.042, 0.085 nm with $x_0 = 1.27$ nm and $s = 0.02$ nm; bottom: $s = 0.005$, 0.01, 0.02, 0.03, 0.05, 0.1 nm with $x_0 = 1.27$ nm and $y_0 = 0.021$ nm.

and the bending vibration range along the y-axis. Along the polarization axis, x_0 depends on α_0, which is given by [109, 134],

$$\alpha_0 = \frac{eE_0}{m_e\omega^2}, \tag{5.13}$$

where e is the elementary charge, E_0 is the peak field strength of the laser, m_e is the electron mass, and ω is the laser frequency. Under the current condition, the intensity $I_0 \sim 10^{15}$ W/cm^2 ($E_0 = \sqrt{\frac{2I_0}{c\epsilon_0}} \sim 8.7 \times 10^{10}$ V/m) gives an $\alpha_0 \sim 2.7$ nm. Since electrons are freed at different times during the pulse (hence at different intensities), x_0 should be set roughly by the time-averaged α_0. If $x_0 = 1.27$ nm is taken, the distribution drops to 1% of its peak at $x = 2.7$ nm, which is roughly the upper limit of the electron radius in the distribution. The value $x_0 = 1.27$ nm probably reflects the fact that ionization starts at intensities in the low 10^{14} W/cm^2 range. Again, since the free electron dynamics in the field should be the same, x_0 is constrained to be the same in both CO_2 and NO_2.

As the length of the electron distribution (x_0) is determined by the oscillating laser field, the width (y_0) will depend on the effective molecular width, which is related to the amplitude of the bending vibration, since the source of electrons are the atoms in the molecule. From Figs. 5.3 and 5.4, CO_2 apparently vibrates between 145° and 215°. Assuming the molecule bends through these angles at its R_e, 0.116 nm, it is straightforward to show the O moves about 0.035 nm away from either side of the axis. If y_0 is taken as ~ 0.021, the distribution falls to about 6% of its maximum value at $y = 0.035$ nm and the model curve agrees with the experiment. For NO_2, the vibration is roughly between $\theta_b = 120°$ and 170°. With $R_e = 0.119$

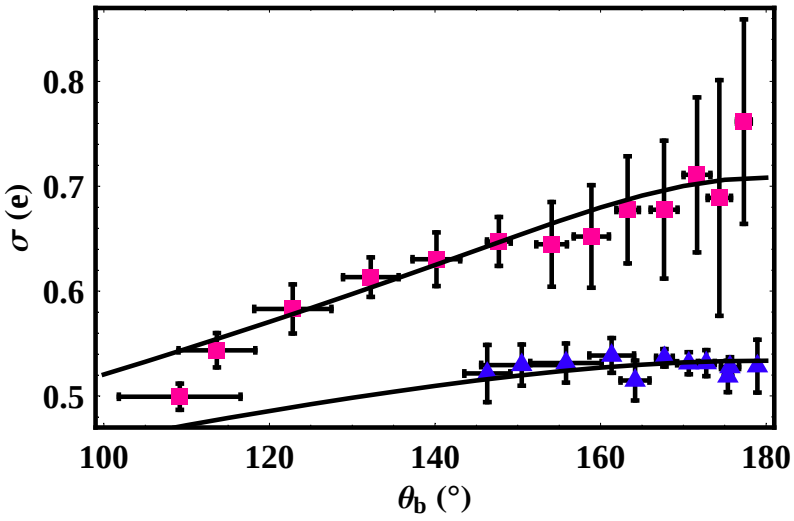

Figure 5.21: Experimental values of $\sigma(\theta_b)$ for CO_2^{6+} (blue triangles) and NO_2^{6+} (red squares) explosions derived from Figs. 5.3 and 5.11 by Eq. 5.7. The SS-model $\sigma(\theta_b)$ curves with $Q_{el} = 1.85$, $x_0 = 1.27$ nm, $y_0 = 0.021$ nm (0.014 nm), and $s = 0.03$ nm (0.01 nm) for CO_2 (NO_2) are represented by the solid curves.

nm, O moves about 0.05 nm. If y_0 is taken as 0.014 nm, the distribution falls to less than 5% at $y = \pm$ 0.025 nm.

For the model curves, once x_0 and y_0 are fixed, Q_{el} and s are used as the primary fit parameters. Since the electron dynamics should be very similar in the two systems, it is not surprising to recognize $Q_{el} \sim 2$ for both systems. It is also not surprising that all the electrons are not trapped in the field; only those born at the right phase of the pulse will revisit the origin for several cycles [109].

The SS-model curves for both triatomics are shown in Fig. 5.21 for the specific values of Q_{el}, x_0, y_0, and s given in the figure caption. It is clear that the SS-model gives a pretty good match to the measurements for both CO_2 and NO_2. The parameters of the curves provide some insight into the physics. First, since the length of the electron distribution (related to x_0) as well as the charge contained

within (Q_{el}) are the same for CO_2 and NO_2, the difference between the two systems would be associated with the width of the distribution, as well as s, the smoothing parameter. The best fit to the data is obtained when y_0 for CO_2 is 50% larger than it is for NO_2. This would imply a smaller charge density in the cloud for CO_2 making $\mathcal{E}_D$ smaller. A smaller $\mathcal{E}_D$ leads to a smaller σ (see Eq. 5.10) as observed. Second, σ decreases with θ_b because the electron distribution is longer than it is wide – its length is ~ 1 nm while its width is $\sim 0.01 - 0.02$ nm. During a linear explosion, for example, the electrons continue to screen the nuclei as they separate. During a bent explosion, where there is a substantial transverse component of the momenta, screening is less efficient as the nuclei move out of the high density area more quickly – σ is smaller. Finally, σ changes more rapidly for NO_2 than it does for CO_2 between about 170° and 145°. This is also due to the fact that the CO_2 electron cloud is wider. A wider cloud means that for the same θ_b, CO_2 experiences a smaller reduction in the screening than NO_2.

5.1.2.3 Discussion

The experimental results show that NO_2 explosion energies decrease monotonically by more than 25% from the smallest to the largest bond angles observed, in contrast to CO_2, which exhibits explosion energies that are nearly independent of bond angle. It is shown that both the enhanced-ionization model with $\zeta(\theta_b)$ and the static electron-screening model are consistent with the dynamics of highly symmetric Coulomb explosions for both CO_2^{6+} and NO_2^{6+}, as shown in Fig. 5.22.

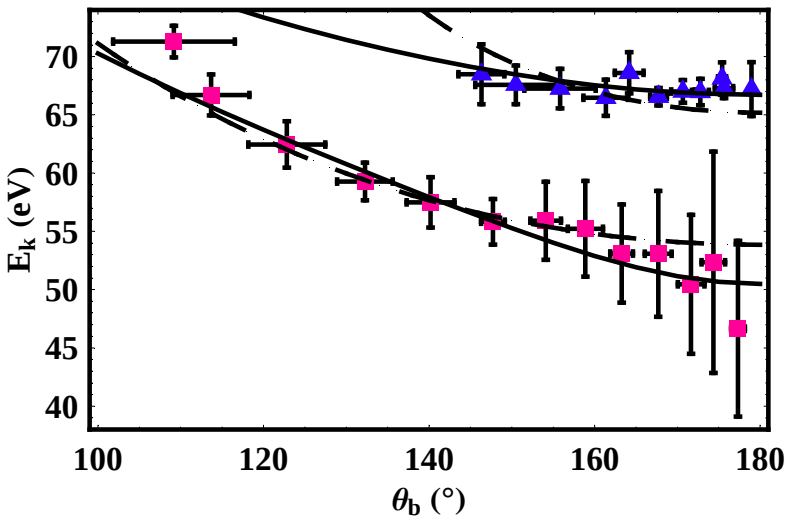

Figure 5.22: Experimental values of $\mathcal{E}_k(\theta_b)$ for CO_2^{6+} (blue triangles) and NO_2^{6+} (red squares) explosions taken from Figs. 5.3 and 5.11. The $R_C - \zeta(\theta_b)$ model curves (dashed) for CO_2 and NO_2 are derived from Fig. 5.18 by Eq. D.8 with $R = R_C$. The SS-model curves (solid) are derived from Fig. 5.21 by Eq. 5.6. The model parameters are the same as those in the figure captions.

The result that the $R_C - \zeta(\theta_b)$ model is consistent with the measurement indicates that the electron dynamics appears to depend on the bond angle and the energy shift between charge-resonance states has a tendency to decrease as the bond angle decreases. This is the simplest application of R_C model. More complicated calculations, such as moving two or more electrons between the charge-resonance states at a time or allowing the nuclei to move, and a better description of the $\zeta(\theta_b)$ function, should be able to produce a better match to the experiments and provide more information about the behavior of the charge-resonance states in triatomic molecular ions. To understand the physics behind this phenomenon, a full quantum treatment may be required.

At the same time, although the fact that a single parameter – the charge defect

(σ, Eqs. 5.6 and 5.7) – generates the same explosion energy as the dynamic-screening model (Fig. 5.19) suggests an average distribution may be sufficient to capture most of the physics, it is obvious that the static-screening model is over-simplified. The size of the electron distribution should depend on the time-dependent laser intensity, according to Eq. 5.13. In fact, we have performed two simple simulations to check how the initial time, when the electrons are freed by the laser field, would affect the final kinetic energy of the Coulomb explosion under the electron-screening effect (App. E). The first one, based on Eq. 5.13, was to simulate the electron distribution as a function of the initial time. The distribution is directly related to the probability for the electron to appear at different positions in the space when the electron is driven by the oscillating field. The result showed that the calculated electron distribution depended on the initial time when the electron was removed by the laser field, as well as the time interval and the laser intensity during the time interval when the electron was oscillating near the molecular ion. The second simulation was to simulate the explosion energy as a function of the initial time with a quasi-dynamic screening calculation. The explosion of three positive charges was simulated under their mutual Coulomb repulsion and the influence of electron wave packets moving according to the radius of vibration of a free electron in the laser field (Eq. 5.13). The result showed that the final kinetic energy of the explosion was sensitive to the initial time when the electrons were born and trapped near the nuclei by the laser field. Both simulations showed the instability of the dynamics – the results were very sensitive to the initial time – which posed a question whether electron screening was a practical and physical description of the dynamics. In order to explore the

validity of the electron screening model further, a full quantum mechanic treatment is required as well as the knowledge about the exact time, relative to the laser pulse, at which each electron is freed may be required.

In addition, experimental results showed that the explosion channels and energies are about the same for enhanced ionizations in both linearly and circularly polarized fields with either the same laser intensity [36] or same electric field[1] [41, 42]. This evidence questions the validity of the electron-screening model because the dynamic screening predicted that the explosion induced by circularly polarized laser pulses would result in the production of ions in higher charge states and larger kinetic energies when linearly and circularly polarized lasers have equal field strength [81]. Although the kinetic energy of the ions was predicted to be comparable for linearly and circularly polarized laser pulses with the same intensity [81], this prediction is conflicted with the argument that the electrons driven by a circularly polarized laser field will not be able to come back near the parent molecular ion [135, 136] so that the electron effect in circularly polarized fields should be significantly different from that in linearly polarized fields. If screening were correct, the kinetic energy release should be different in linearly and circularly polarized fields.

Step-by-step experimental evidence of the dynamics on shorter time scale is necessary to reveal the details of the physics behind dissociative ionization. One possible experiment is a pump-and-probe, similar to the idea proposed by Stapelfeldt *et al.* [137]. A 100-fs pulse pumps the molecule, a sub-10-fs pulse serves as a probe,

[1]With the same intensity (electric field), the electric fields (intensities) in linearly and circularly polarized lasers are $E_L = \sqrt{2}E_C$ ($I_L = I_C/2$).

while the delay between two pulses is varied. As the short pulse explodes the molecule at different stages of dissociative ionization induced by the long pulse, the kinetic energy as well as the angular spread of the ejected ions may be observed as a function of time at femtosecond resolution. The results should provide detailed information about how the molecular structure, or even electronic dynamics, evolves during ionization.

5.2 Ejection Anisotropy Measurement

In this section, the explosion dependence of the orientation angle (ejection anisotropy) in small triatomic and diatomic molecules are investigated. The experimental determination of the ejection anisotropy in enhanced ionization of a series of small molecules induced by intense laser fields includes two steps. First, the angular distribution of the energetic charge ejection subsequent to Coulomb explosion is determined by isolating a series of specific orientations (θ_g, *geometric* orientation angle, the angle between the molecular and polarization axes) of the precursor ions and measuring their relative signal strengths by *coincidence imaging* (Sec. 4.3). Second, the degree of dynamic alignment is determined quantitatively by comparing explosion signals induced by linearly and circularly polarized fields. The results are discussed in terms of the ionization stages, induced dipole moments, rotational constants of the molecules as well as the time that the precursor molecular ions spend in the field prior to the Coulomb explosions. The experimental results are presented in Sec. 5.2.1, while Sec. 5.2.2 gives the discussion.

5.2.1 Experiments and Results

In the determination of the ejection anisotropy in enhanced ionization of small molecules induced by intense laser fields, the experiment conditions are the same as described in Sec. 5.1.1, and the intensity of the circularly polarized field is twice that of the linearly polarized field so that the electric field is the same for the comparison. Small molecules (N_2, O_2, CO_2, and NO_2) composed of atoms with similar mass were used as samples to compare the ejection anisotropy in diatomic and triatomic Coulomb explosions, and the results were also compared with that for H_2 which has been found to be dynamically aligned in a short pulse ($\sim$ 50 fs) [86].

5.2.1.1 Angular Spread Measurement

In the first step of the determination of ejection anisotropy, the explosion angular distributions of two triatomic systems [63], CO_2 (nominally linear) and NO_2 (bent in its ground state with an equilibrium angle, $\theta_{be} = 134°$), were compared with that of H_2, N_2, and O_2. For the triatomics, the symmetric 6-electron channel, the dominant channel under our experimental conditions, is chosen ($XO_2^{6+} \rightarrow O^{2+} + X^{2+} + O^{2+}$, where X is C or N). In the symmetric channel, the magnitudes of the momenta of the two O ions are equal in the center of mass frame. *Coincidence imaging* (Sec. 4.3), with the ability to isolate precursor orientations and geometries, is used to make a series of measurements. The probability (signal strength) of strong-field induced Coulomb explosions is measured as a function of θ_g for a fixed bond angle (θ_b, see Figs. 4.8c and 4.8d). This series of measurements was repeated at

Table 5.2: Molecular constants and properties for CO_2, NO_2, H_2, N_2, and O_2. The quantities are extracted from experimental measurements: R_e, the equilibrium bond length [114]; R_C, the critical separation [this study]; θ_{be}, the equilibrium bond angle [114]; B_0, the ground state rotational constant [114]; n, the exponent of cosine distribution [this study]; $\Delta\theta_g$, the angular spread of the distribution [this study].

	CO_2	NO_2	H_2	N_2	N_2	O_2	O_2
Explosion Channel	2,2,2	2,2,2	1,1	1,2	2,2	1,2	2,2
R_e (nm)	0.116	0.119	0.074	0.110	0.110	0.121	0.121
R_C (nm)	0.22	0.26	0.25	0.22	0.23	0.23	0.23
θ_{be} (Deg)	180	134	N/A	N/A	N/A	N/A	N/A
B_0 (cm^{-1})	0.39	0.434	60.853	1.998	1.998	1.438	1.438
n	39	25	19	7	15	11	15
$\Delta\theta_g$ (Deg)	22	27	31	50	34	40	34

several bond angles between 110° and 180°. The probability for Coulomb explosions as a function of θ_g was also measured for diatomics under the same conditions at their peak explosion momenta.

The probability of Coulomb explosions for CO_2 and NO_2 at their equilibrium bond angles (180° and 134° respectively) are shown in Fig. 5.23 along with that of H_2. These distributions were fit to $\cos^n \theta_g$ and the full widths at half maximum ($\Delta\theta_g$) were extracted; the results are given in Table 5.2. There is a monotonic increase in the width of the distribution as one goes from CO_2 (the smallest) to H_2 (the intermediate), and to N_2 and O_2 (the largest). Curves representing $\Delta\theta_g$ vs θ_b for CO_2 and NO_2 are shown in Fig. 5.24. It should be noted that $\Delta\theta_g$ increases with decreasing n. Thus, the remarkable flatness of these curves is an indication that n is nearly independent of θ_b.

Since the induced dipole moment depends on the separation of charge between the two ends of the molecule, one might be tempted to argue that the ejection

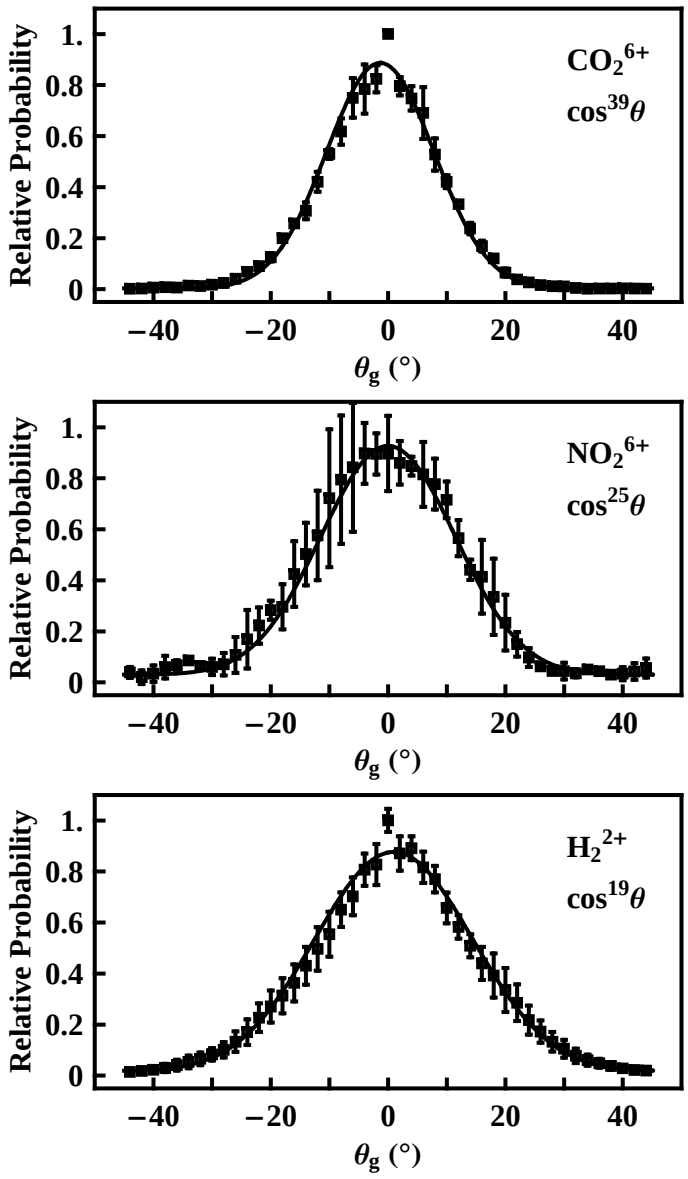

Figure 5.23: A comparison between the relative probabilities for Coulomb explosion as a function of θ_g: (upper) the symmetric CO_2^{6+} explosion channel at 180°, (middle) the symmetric NO_2^{6+} channel at its equilibrium bond angle (134°), and (lower) H_2. The error bars correspond to the standard deviation for four different runs. The solid curves are $\cos^n \theta_g$ fits where $n = 39$, 25 and 19, respectively for CO_2, NO_2 and H_2. The FWHM, $\Delta\theta_g$, of the distributions are respectively 22°, 27° and 31°.

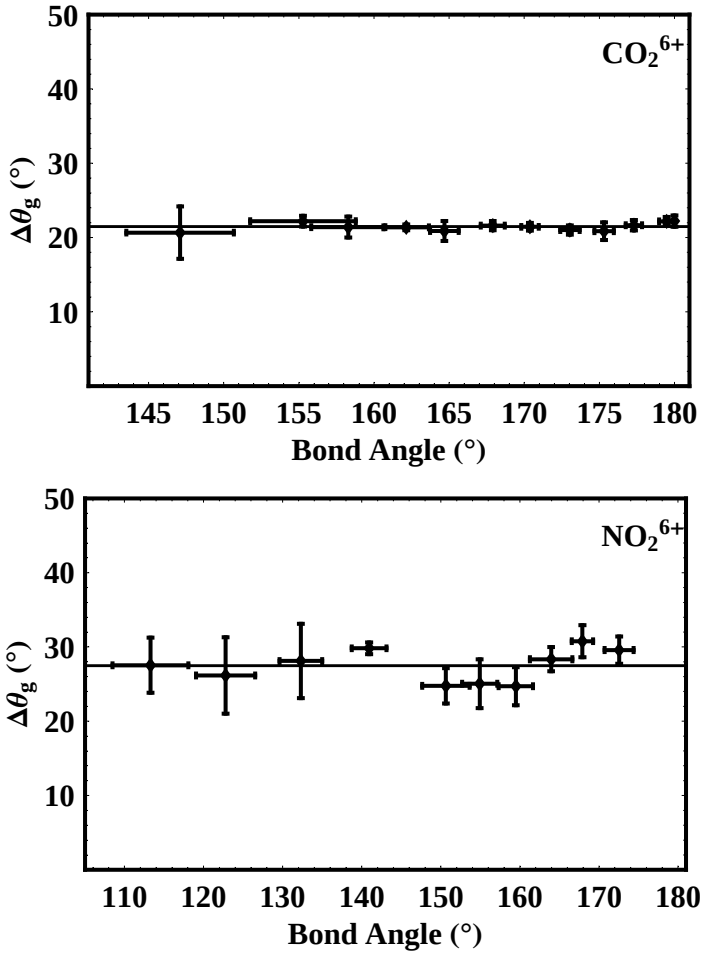

Figure 5.24: The widths ($\Delta\theta_g$) of the orientation distributions vary as a function of bond angle for the symmetric CO_2^{6+} (upper) and NO_2^{6+} (lower) Coulomb explosion channels. The data are extracted from distributions similar to those shown in Fig. 5.23. The error bars are the standard deviation over four different runs. The solid lines are the equilibrium $\Delta\theta_g$ values (22° for CO_2 and 27° for NO_2).

distribution in the Coulomb explosion of triatomics should depend on bond angle. Such an argument would be based on the fact that when the systems bend, the length of the molecules will change according to $2R\sin(\theta_b/2)$ (where R is the bond length between the outer and central atoms). For CO_2 (NO_2), this separation changes by 2.5% (15.5%) over the range of bond angles observed for a fixed bond length. While the scatter in the data in Fig. 5.24 is consistent with variations of these magnitudes,

there is no clear increase from one side to the other in either system. Since the ionization is at least in part sequential, ionization is distributed throughout the pulse, giving the triatomic systems time to execute bending vibration. The ground state vibrational frequencies, 667 and 750 cm^{-1}, correspond to periods of 50 and 44 fs respectively for CO_2 and NO_2. Higher vibration levels and ion states tend to be stiffer, leading to even shorter periods. Consequently, the flat distribution in Fig. 5.24 could be an indication of angular washout, resulting from various stages of ionization occurring at different bond angles.

5.2.1.2 Dynamic Alignment Measurement

In the second step of the determination of ejection anisotropy, the degree of dynamic alignment is measured by comparing the ion yield ratio in linearly and circularly polarized fields. The dynamic alignment is characterized by a parameter η, the degree of dynamic alignment, which ranges from 0 (no dynamic alignment) to 1. These limits can be linked to the relative number of atomic ions, $\mathcal{R}$, generated under linearly (N_{LP}) and circularly (N_{CP}) polarized fields;

$$\mathcal{R} = N_{LP}/N_{CP}. \tag{5.14}$$

In the absence of dynamic alignment, $N_{LP,G} < N_{CP}$ and $\mathcal{R} \to \mathcal{R}_G$. The subscript G means the population ionized solely through geometric alignment. When there are N_0 molecules in the laser focus,

$$N_{LP,G} = \frac{1}{\pi} N_0 \int_{-\pi/2}^{\pi/2} \cos^n \theta_g \mathrm{d}\theta_g, \tag{5.15}$$

where $\cos^n$ is the angular distribution of the explosion, while

$$N_{CP} = \frac{1}{\pi} N_0 \int_{-\pi/2}^{\pi/2} \mathrm{d}\theta_g = N_0. \tag{5.16}$$

At intensities of 10^{15} W/cm^2, all molecules parallel to $\vec{E}$ ($\theta_g = 0$) are ionized. The entire population is ionized in circularly polarized fields because all polarization directions are sampled. Therefore,

$$\mathcal{R}_G(n) = \frac{N_{LP,G}}{N_{CP}} = \frac{1}{\pi} \int_{-\pi/2}^{\pi/2} \cos^n \theta_g \mathrm{d}\theta_g = \frac{1}{\sqrt{\pi}} \Gamma\left(\frac{n+1}{2}\right) / \Gamma\left(\frac{n+2}{2}\right). \tag{5.17}$$

When all molecules are torqued into alignment with $\vec{E}$ (complete dynamic alignment), $N_{LP} \rightarrow N_{CP}$ and $\mathcal{R} \rightarrow 1$. Thus, the degree of alignment is defined as

$$\eta \equiv (\mathcal{R} - \mathcal{R}_G)/(1 - \mathcal{R}_G), \tag{5.18}$$

which is a measure of the population being torqued.

To measure N_{LP} and N_{CP}, linearly polarized radiation was generated directly from the Ti:Sapphire regenerative amplifier (Sec. 3.1). Elliptical polarization was generated with a quarter-wave plate. The experiments were run with an ellipticity, ϵ, of about 0.92, where $\epsilon = E^</E^>$. The electric field along the major (minor) axis is indicated by the superscript $>$ ($<$); $E^< = 0$ corresponds to linear polarization. The direction of the major axis was controlled with a half-wave plate. Enhanced ionization is assumed to occur at the critical radius, R_C, which is determined by the field strength [73]. Thus, to keep the field the same, the circular polarization intensity was twice that of the linear polarization. When $\epsilon = 0.92$, the fields are nearly the same for elliptical (EP) and linear (LP) polarizations – $E^>_{EP} \cong 1.04 E_{LP}$ and $E^<_{EP} \cong 0.96 E_{LP}$. approximate circular polarization more closely, we averaged

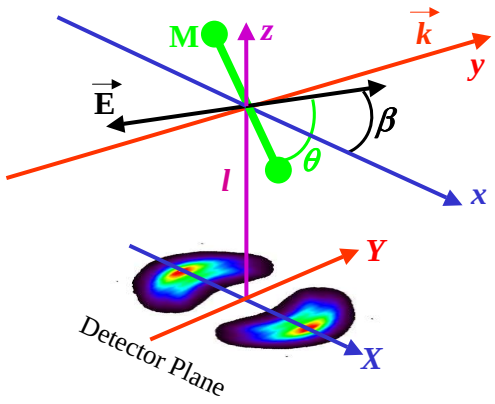

Figure 5.25: Coordinate systems in the focal and detector planes, separated by a distance l, with the x and y axes are parallel to the X and Y axes. The laser field ($\vec{E}$) is polarized in the xz-plane at an angle β and the molecular axis ($\vec{M}$) is oriented at an angle θ relative to $\vec{E}$.

four images with $\vec{E}_{EP}^{>}$, confined to the xz-plane (see Fig. 5.25), pointing in two orthogonal directions by rotating the half-wave plate through 180°.

The ion yield ratio $\mathcal{R}$ is extracted from Fig. 5.26, which contains: (1) linear polarization images obtained at 2×10^{15} W/cm^2 (top), (2) circular polarization images obtained at 4×10^{15} W/cm^2 (middle) and (3) an average of 18 linear polarization images each taken with a different β separated by 10° between 0° and 170° obtained at 2×10^{15} W/cm^2 (bottom). In these experiments, each image contained 200,000 laser shots. The CO_2 images contain doubly and triply charged ions, N_2 and O_2 images contain doubly charged ions while the H_2 images are exclusively protons. Since the physics is independent of β, the N_{LP} should be approximately the same in the top and bottom rows. This is clearly not the case, which is due primarily to gain variation over the MCP. Since the charges are collected over the same area of the plate in the two lower rows, gain variation divides out. Consequently, using the the two lower rows gives a better estimate of $\mathcal{R}$. To obtain η from Eq. 5.18, $\mathcal{R}_G(n)$

needs to be estimated from Eq. 5.17 first. Lacking detailed information of pure geometric alignment, the exponent of the cosine function (n) representing the angular distribution of the explosion in the absence of dynamic alignment is assumed to be roughly the same as the n measured in linear polarization (Table 5.2). If η, the degree of dynamic alignment, is small, this assumption should be pretty safe. Even if η is large, as the molecule is torqued and ionized at a final orientation angle θ_g, the ionization rate or probability at θ_g should still obey the angular distribution of pure geometric alignment and the measured value of n should be approximately the same with or without dynamic alignment.

Figure 5.27 displays $\mathcal{R}$ vs. n for the four systems along with an estimate of η, which graphically is related to the relative distance to the upper and lower curves. Clearly, η depends on the value of n. The values plotted correspond to n_{eff}, a weighted average of the primary channels for each system as discussed in the next paragraph. The values of n for specific channels are listed in Table 5.2. While at a given intensity n is independent of bond angle for CO_2, it is affected by several other parameters for all the systems. First, it depends on the intensity. At high enough intensities, ionization will saturate and all molecules within an angle around the polarization axis will ionize. This angle grows with intensity, broadening the distribution and reducing the apparent n. To explore this behavior, the intensity was varied between 1 and 4×10^{15} W/cm^2 and found n to be constant to within 7%. Wider intensity excursions caused n to exhibit larger variations. This is due in part to the opening and closing of different ionization channels; n increases monotonically with ionization stage [37, 39].

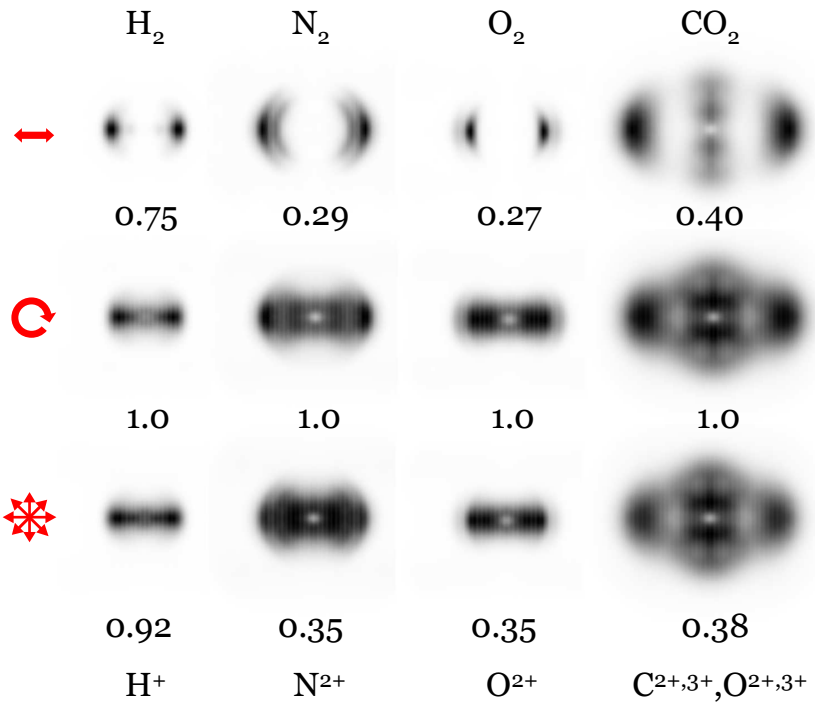

Figure 5.26: Momentum distributions of Coulomb explosions obtained with a linear polarization at $I_0 = 2 \times 10^{15}$ W/cm^2 and $\beta = 0°$ (top), circular polarization at $2I_0$ (middle) and average image composed of 18 linear polarizations at I_0 with β ranging from 0° to 170° in steps of 10° (bottom). Beneath each image is its relative ion yield normalized to the second row in each column. The images in the top and middle rows are composed of 200,000 laser shots and the bottom 18 × 200,000 shots.

Since the images in Fig. 5.26 are composed of several channels, except for H_2, n and η will be somewhere between the values for the dominant channels. The dominant channels for each system are listed in Table 5.3 along with the contribution this channel makes to the images in Fig. 5.26. Also given in the table are n_{eff} (the sum of n's for the primary and secondary channels weighted by the channel's contribution) for each system and an effective full width, $\Delta\theta_{eff}$, associated with n_{eff}. It is noted that n_{eff} is only approximate for CO_2 because the correlation signals between the doubly and triply charged ions were too weak to determine the

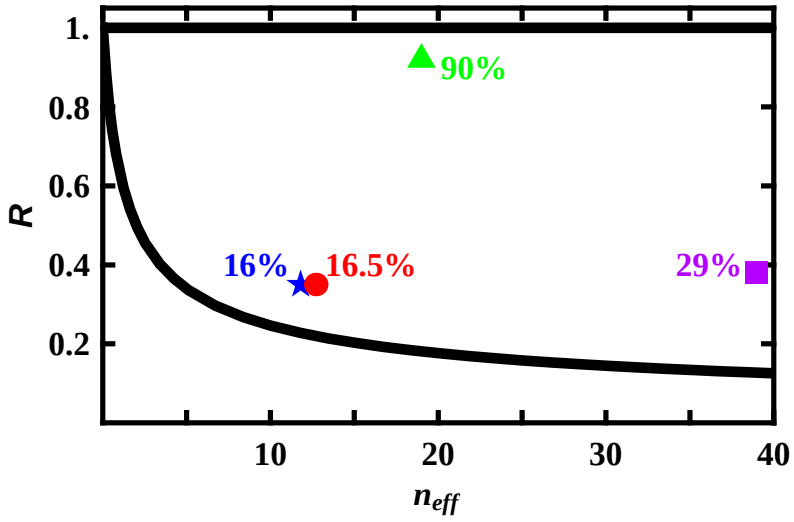

Figure 5.27: Ion yields, $\mathcal{R}$ vs n_{eff} for H_2 (green triangle, 0.92), N_2 (blue star, 0.35), O_2 (red circle, 0.35) and CO_2 (magenta square, 0.38). The upper (lower) solid curve is $\mathcal{R} = 1$ ($\mathcal{R} = \mathcal{R}_G$). Values for η (%) are also given.

angular distributions for mixed charge-state channels. The fact that n increases with the charge state means the n_{eff} given in the table should be considered a lower limit for CO_2. Since $\mathcal{R}_G(n)$ has a negative slope, η for CO_2 is also a lower limit.

5.2.2 Data Analysis and Discussion

Regarding the observed anisotropies (n and $\Delta\theta_g$ in Table 5.2), three issues are worth discussing. First, why are triatomics, especially CO_2, significantly narrower than diatomics? Second, why is NO_2 wider than CO_2? And third, why is H_2 narrower than the other two diatomics? The fact that the anisotropy is strongly correlated with the polarization axis suggests that the responsible mechanism must depend on the dipole moment, $\vec{\mu}$, induced by the field. While any molecule that is more polarizable along one of its axes will have an effective dipole given by $\boldsymbol{\alpha}\cdot\vec{E}$,

Table 5.3: Dynamic alignment parameters for H_2, N_2, O_2, and CO_2 obtained in the experiments: the primary (secondary) channel and its contribution (%), its n and $\Delta\theta_g$ taken from Table 5.2, $\Delta\theta_{eff}$ ($\Delta\theta_{da}$) the effective (apparent) angular spread for n_{eff} (n_{da}), R_e and R_C taken from Table 5.2, η the degree of dynamic alignment (Eq. 5.18), $\mathcal{R}$ the relative number of atomic ions generated under linearly and circularly polarized fields (Eq. 5.14), $\Delta\mathcal{R}$ the number of molecules torqued in the dynamic alignment, and $T_i/T_i(O_2)$ the interaction time relative to that for O_2 calculated at $\langle\bar{R}_{mol}\rangle = (R_e + R_C)/2$ by the two methods discussed in the text, where $R_{mol,e}$ ($R_{mol,C}$) $= 2R_e$ ($2R_C$) for CO_2.

	H_2	N_2	O_2	CO_2
Primary Channel	1,1 (100%)	2,2 (62%)	2,1 (62%)	2,2,2 (80%)
Primary n ($\Delta\theta_g$)	19 (31°)	15 (34°)	11 (40°)	39 (22°)
Secondary Channel	none	2,1 (38%)	2,2 (38%)	2,3,2/3,2,2 (20%)
Secondary n ($\Delta\theta_g$)	N/A	7 (50°)	15 (34°)	N/A
n_{eff}	19	12.1	12.5	~ 39
$\Delta\theta_{eff}$	31°	38.6°	37.8°	22°
n_{da}	0.13	4.67	4.67	3.88
$\Delta\theta_{da}$	179.4°	60.9°	60.9°	66.5°
R_e (nm)	0.074	0.110	0.121	0.116
R_C (nm)	0.25	0.23	0.23	0.22
η	90%	16%	16.5%	29%
$\mathcal{R}$	0.92	0.35	0.35	0.38
$\Delta\mathcal{R}$	0.74	0.12	0.13	0.25
$T_i/T_i(O_2)$	1.4, 17	0.8, 0.9	1, 1	2.7, 2.4

where $\boldsymbol{\alpha}$ is the polarizability matrix and $\vec{E}$ is the applied field, intense fields also establish a charge dichotomy between the two end atoms, promoted by charge resonance states. Transitions involving charge resonance states increase in strength with R [73, 93] eventually dominating the transition moments. As a result, the field becomes very effective at moving charge back and forth across the molecule establishing a very strong dipole, which interacts with the applied field.

When the pulse is very short compared with the rotational period of the molecule, the field essentially provides a coherent kick to the system, an effect that

has been exploited to align linear molecules (see, for example [138] and reference therein). At the other extreme, the field has sufficient time not only to torque the system but to restrict the rotational motion severely leading to pendular states [112, 138]. In the latter case, the depth of the confining potential is proportional to $|\vec{\mu} \cdot \vec{E}/B_o|$ (Page 28), the ratio between the dipole interaction energy with the field and the rotation energy. Since B_0 (Table 5.2) is about two orders of magnitude larger for H_2 and roughly four times larger for N_2 and O_2, the triatomics will find themselves in a much deeper and narrower potential, for the same field strength. In addition, the charge-resonance dipole moment is proportional to the molecular size, so that triatomics would have $\vec{\mu}$ twice as large as diatomics, for the same charge disparity.

At the same time, both CO_2 and NO_2 lose more electrons before they explode than do O_2 and N_2, while H_2 loses the least electrons. It is clear from both long and short pulse experiments that the anisotropy becomes more acute as electrons are removed. At 130 fs, for example, the width of N_2 explosions are observed to sharpen from about 58° for the 3-electron channel ($N_2^{3+} \rightarrow N^{2+} + N^+$) to about 28° for the 6-electron channel ($N_2^{6+} \rightarrow N^{3+} + N^{3+}$) [37]. This same study showed sharpening in the Cl_2 explosion spectra with ionization stages as well. At 40 fs, the 2-electron channel of N_2 ($N_2^{2+} \rightarrow N^+ + N^+$) was measured to have a width of 50° while the 5-electron channel ($N_2^{5+} \rightarrow N^{3+} + N^{2+}$) was observed to have a width of 36° [39]. The same sharpening, for both N_2 and O_2 from (1,2) to (2,2) channels, has been observed in our measurement (Table 5.2). This implies that the angular selection rule of the enhanced ionization $\langle i|\vec{\mu}\cdot\vec{E}|f\rangle^n$, thus the angular spread

due to geometric alignment, should become narrower as the charge state increases. Therefore, considering the confining potential and molecular ionization stage, the degree of alignment (n in angular distribution $\cos^n \theta_g$) should follow the order of CO_2 (NO_2) > O_2 (N_2) > H_2 for the explosion channels in this study (Table 5.2), thus the widths of the distributions should follow CO_2 (NO_2) < O_2 (N_2) < H_2.

While CO_2 and NO_2 have comparable moments of inertia and lose the same number of electrons in the final channel, the width of the distribution for CO_2 is considerably narrower. The reason could be that NO_2 bends through smaller angles than CO_2. If a dipole moment were established between the outer and central atoms, perpendicular to the molecular axis, the confining potential of pendular states as well as the angular selection of the ionization could be broadened so that NO_2 has a larger angular spread. A perpendicular dipole could also make the field less efficient at torquing NO_2. Consequently, that CO_2 has a narrower distribution than NO_2 is very reasonable.

While the angular distribution of H_2 determined by the confining potential and molecular ionization stage might be broader than all other molecules in this study, it has the highest degree of dynamic alignment (Fig. 5.27). In fact, its dynamic alignment is much higher than other molecules and almost complete, due to its significantly smaller moment of inertia, which causes its free rotation to be faster as well as making it easier to torque. As almost all the population is torqued into ionization, it is very reasonable for H_2 to produce a narrower angular distribution than O_2 and N_2 even with a lower molecular ionization stage.

Since the dynamic alignment of H_2 is almost complete, it is possible that

the angular spread of H_2 explosion could be actually broader in pure geometric alignment than the measurement made in the linearly polarized field where dynamic alignment is active. Since η depends on the angular spread ($\Delta\theta_g$ or n) in pure geometric alignment (Eqs. 5.17 and 5.18), different n or $\Delta\theta_g$ would result in different η. However, even if $\Delta\theta_g$ is assumed to be as large as 60° (double the value in Table 5.2 and corresponding to $n \sim 5$), η of H_2 would still be more than 80%, still much larger than O_2 or N_2 (Fig. 5.27). Nonetheless, the analysis described in the last paragragh would stand.

Following Fig. 5.27 and Tables 5.2 and 5.3, it is obvious that angular spread as well as dynamic alignment is essentially the same for N_2 and O_2. This is consistent with the fact that their R_C's, charge states, and moments of inertia are all about the same. However, an η for CO_2 higher than N_2 and O_2 is surprising. The degree of dynamic alignment, or the number of molecules torqued by the laser field, should be governed by the classical equation of motion for θ_g (App. A),

$$\ddot{\theta}_g = -\frac{\vec{\mu} \times \vec{E}}{I_m} = -\frac{\mu E}{I_m} \sin\theta_g = -\frac{\zeta e E R_{mol}}{I_m} \sin\theta\cos\theta, \tag{5.19}$$

where $\vec{\mu}$ is the induced dipole moment, $\vec{E}$ is the laser field, and I_m is the moment of inertia. While $|\vec{\mu}| \simeq \zeta e R_{mol} \cos\theta$ (App. A) sustained by charge-resonance states [73], where R_{mol} is the total length of the molecule, increases relative to N_2 and O_2, I_m of CO_2 is also larger ($\propto R_{mol}^2/4$), leading to an overall reduction in the torque at both R_e and R_C given in Table 5.2. At the same time, a higher ionization stage is consistent with the precursor ion spending more time in the field [37, 39]. The ionization stages are H_2^{2+}, N_2^{4+}, O_2^{4+} and CO_2^{6+}. Evidently, a longer interaction time

with the field, perhaps combined with multiphoton ionization prior to enhanced ionization, leads to a significant enhancement in the number of molecules torqued beyond that expected from Eq. 5.19.

The exact nature of the enhancement requires more knowledge of the evolution of the systems in the field than that we currently have. However, it is possible to see that the enhancement for CO_2 is consistent with a longer interaction time with the field, T_i. The simplest model assumes that $T_i \propto$ the number of molecules torqued; longer interaction times will allow more molecules to be aligned. Under the field strengths in this study, molecules nearly aligned within the polarization axis will be trapped in pendular states [112], so no molecules will be lost once aligned with the field. Thus, $\Delta\mathcal{R} = \mathcal{R} - \mathcal{R}_G$ from Fig. 5.27, which is a measure of the molecules torqued, can be exploited to estimate the relative interaction time, $T_i(CO_2)/T_i(O_2)$ $\propto \Delta\mathcal{R}(CO_2)/\Delta\mathcal{R}(O_2)$.

To estimate the relative time, however, the difference in the moments of inertia and molecular lengths of the two systems must be accounted for. The coefficient can be determined from Eq. 5.19. Assuming the molecules start from rest, this equation can be solved to give a rotation time from θ_g to 0 (Eq. A.18),

$$T(\theta_g) = K(\sin^2\theta_g)\sqrt{\frac{mR_{mol}}{2e\zeta E}}, \tag{5.20}$$

where K is the *elliptic integral of the first kind* (App. A). Thus, to compensate for the differences in the molecular size the relative interaction time can be written as

$$\frac{T_i(CO_2)}{T_i(O_2)} = \frac{\Delta\mathcal{R}(CO_2)}{\Delta\mathcal{R}(O_2)}\sqrt{\frac{\zeta_{O_2}R_{mol}(CO_2)}{\zeta_{CO_2}R_{mol}(O_2)}}. \tag{5.21}$$

As discussed in Appendix A, theoretical calculations for charge resonance showed

that $\zeta \propto 0.5R_{mol}$ and $0.4R_{mol}$ for H_2^+ [73] and H_3^{2+} [93], respectively, resulting $\sqrt{\zeta_{H_2}/\zeta_{H_3}} = 1.1 \approx 1$. Since no theoretical calculations, of which we are aware, have been published for N_2, O_2 or CO_2, we assumed ζ to be the same for all the molecules in this study. Therefore, Eq. 5.21 becomes

$$\frac{T_i(CO_2)}{T_i(O_2)} = \frac{\Delta\mathcal{R}(CO_2)}{\Delta\mathcal{R}(O_2)}\sqrt{\frac{R_{mol}(CO_2)}{R_{mol}(O_2)}}. \tag{5.22}$$

Values for the relative times are given as the first number in the last row in Table 5.3. Since it is unknown where the systems are torqued most efficiently, an average $\bar{R}$ is chosen for these calculations between R_e and R_C. This model shows that CO_2 spends about 2.7 times longer in the field than O_2. While O_2 and N_2 spend about the same amount of time, this model suggests H_2 spends about 40% more time in the field than O_2 and N_2. It is important to know that these ratios depend on the values selected for $\bar{R}$. If, for example, H_2 were torqued more efficiently near its R_e, while O_2 closer to its R_C, this model would suggest H_2 spends 20% less time than O_2. Since H_2 loses only two electrons while the other systems lose more, it is not unreasonable to expect H_2 to be torqued closer to R_e than the other systems.

It is also possible to estimate T_i more directly from $T(\theta_g)$ (Eq. 5.20), if it is recognized that the molecules torqued by the field for a specific n_{eff} lie outside $\Delta\theta_{eff}$, the width of the angular distribution given in Table 5.3. In the absence of dynamic alignment, only the molecules within this angular spread, $\mathcal{R}_G$ (Eq. 5.17), would be ionized. For $\mathcal{R}$ to exceed $\mathcal{R}_G$, extra molecules must be rotated into this angle prior to enhanced ionization. Since $K(\sin^2\theta_g)$ increases monotonically with θ_g from 0 to 90°, it gets harder and harder to rotate molecules as θ_g increases. One can estimate

the width of the distribution of the molecules responding to dynamic alignment, $\Delta\theta_{da}$, from an apparent exponent, n_{da}, which is obtained by equating $\mathcal{R}_G(n_{da})$ with the measured $\mathcal{R}$. The interaction time, T_i, can be estimated by calculating how long it takes molecules at θ_{da} $(= \Delta\theta_{da}/2)$ to rotate to θ_{eff} $(= \Delta\theta_{eff}/2)$, which is given by $T(\theta_{da}) - T(\theta_{eff})$. The relative interaction times in this approach are given as the second number in the last row in Table 5.3. Except for H_2, the two methods are in agreement. Again, the time for H_2 is most likely too large not only because of uncertainty in the molecular lengths but because it is assumed that the molecules are not rotating. A combination of the facts that $K(\sin^2\theta_g) \to \infty$ as $\theta_g \to 90^\circ$ and that $\theta_{da} \lesssim 90^\circ$, explains why the time for H_2 is so long. Since the H_2 molecules are rotating rather rapidly compared with the other systems, it is not necessary for the field to do all the work; most of the molecules will rotate to much smaller angles. For example, if $\theta_{da} = 59^\circ$, $R(H_2) = R_e$ and $R(O_2) = R_C$, the rotation times for H_2 and O_2 would be about the same.

In summary, a general technique is developed for measuring the contribution that geometric and dynamic alignment make to the ejection anisotropy induced by strong laser fields, and is employed in the quantitative angular dependence study of 2- and 3-atom Coulomb explosions on a time scale of 100 fs. The experimental results show clearly that triatomic systems can have narrower distributions than diatomic systems at comparable ionization stages. This is probably because of the higher ionization stage, larger induced dipole and smaller rotational constant of the triatomics. The width of the CO_2 distribution is narrower than that of NO_2, but both are nearly independent of bond angle. While the difference in the widths could

be associated with a larger induced dipole moment perpendicular to the molecular axis, which is caused by NO_2 bending to smaller bond angles, the independence of bond angle could be an exhibition of angular washout, resulting from various stages of ionization occurring at different bond angles. The argument that the small moment of inertia of H_2 allows it to be more easily torqued even by a short pulse is confirmed by its degree of dynamic alignment. However, the potential restricting rotational motion (to pendular states) established by the field is broader for a larger rotational constant. Thus, systems with a smaller rotational constant relative to H_2 (e.g., CO_2, NO_2, N_2 etc.) will experience a narrower confinement potential when sufficient time is allowed for them to be trapped. This is confirmed recently by alignment experiments with 300 ps laser pulses [139, 140], where the degree of alignment is found in the order of $CS_2 > CO_2 > N_2 > H_2$, and consistent with our analysis. The results also show that the anomalous dynamic alignment in the linear triatomic CO_2 is consistent with the removal of more electrons at the time of the Coulomb explosion, thus the precursor ion spends more time in the field than diatomic systems such as N_2 and O_2. While the simple classical model sheds some light on the underlying physics, a full quantum mechanical treatment is necessary to confirm these ideas about the interaction times. At the same time, the effect of the valence electron structure on ejection anisotropy in enhanced ionization, which is neglected in this study, and the potential contribution that angular momentum introduced by circular polarization [35] makes to the anisotropy need to be investigated.

Chapter 6

SUMMARY AND FUTURE WORK

6.1 Summary

Correlation detection techniques (*image labeling* [99], *coincidence imaging* [63], and *joint variance* [103]) developed in this study are based on the image spectrometer that is capable of collecting charges ejected over 4π sr and the digital camera that can be synchronized with the laser repetition rate at up to 735 Hz [22, 99, 100]. The collection capability in both spatial and temporal domain ensures that all the ejected ions with momenta up to $\sim 80\sqrt{qm}$ a.u., where qe is the charge and m is the atomic mass, can be detected and analyzed with enough statistics. The advantage provided by these techniques is that both diatomic and triatomic molecular explosion channels with different momenta (energies), bond angles, and/or orientation angles can be isolated; thus, the pre-explosion molecular configurations (bond lengths and/or bond angles) and orientations as well as their distributions can be derived. These results draw a clear picture about the molecular dynamics. As these techniques are applied in the study of strong-field dynamics, details of how the molecules respond to the ultra-fast intense fields are revealed quantitatively. Furthermore, as different decay channels can be easily isolated, these techniques should be useful tools for laser control studies to detect transient states in molecular dynamics as shorter (broader bandwidth) pulses are applied and as the incoming pulses are being shaped.

With the correlation detection techniques, molecular dynamics, specifically Coulomb explosion as a function of bond angle in linear and bent triatomics and ejection anisotropy of both triatomics and diatomics under the influence of intense 100-fs laser fields, were investigated in this study.

The experimental results revealed that the NO_2 explosion energies decrease monotonically by more than 25% from the smallest to the largest bond angle. This is in sharp contrast to the behavior of CO_2, where the explosion energies are nearly independent of bond angle [62]. We developed 2-D enhanced-ionization and static-screening models to analyze the measured explosion energies as a function of bond angle. In the enhanced-ionization model, the energy shifts of the charge-resonance states at the three charge centers, represented by the parameter ζ (Eqs. 5.3 and 5.4), is recognized to be the primary reason for the bond-angle dependence of the explosion energy. Smaller shifts (smaller ζ) lead to larger explosion energy and vise versa. In the static-screening model, the shape and density of the photo-electron distribution around the exploding molecular ion, represented by the parameters x_0, y_0 and ρ_0 (Eqs. 5.8 and 5.12), are believed to be responsible for the variation of the explosion energy as a function of the bond angle. A broader or thinner electron distribution causes a larger explosion energy. As we have shown, the predictions of both the enhanced-ionization and static-screening models are consistent with the explosion energies of highly symmetric Coulomb explosions for both CO_2^{6+} and NO_2^{6+} (Fig. 5.22). However, the instability of the electron-screening calculation is an issue that needs to be addressed further. At the same time, the observed explosion signals as a function of bond angle for both CO_2 and NO_2 showed large-amplitude

vibrations and peaked at the equilibrium bond angles of the neutral molecules.

The contributions geometric and dynamic alignment make to the ejection anisotropy observed following molecular Coulomb explosion induced by strong laser fields were measured with correlation techniques [63] and by comparing the image spectra obtained in linearly and circularly polarized fields. The magnitude of the spread in the observed angular distributions ($\Delta\theta_g$, Table 5.2) in increasing order was found to be CO_2 (NO_2) < H_2 < O_2 (N_2). The narrower angular distributions of the triatomic systems was explained in terms of the precursor molecular parent system reaching a higher ionization stage prior to explosion and larger induced dipole. A narrower distribution of H_2 than that of O_2 (N_2) was seen to be due to a dynamic alignment being nearly complete. The measured degrees of dynamic alignment (η, Table 5.3) in decreasing order was found to be H_2 > CO_2 > O_2 (N_2). The near-complete dynamic alignment of H_2, the highest among the samples, is due to the fact that it has the smallest moment of inertia. The analysis, based on the classical pendulum equation, showed that the anomalously large dynamic alignment in the linear triatomic CO_2 is consistent with the field removing more electrons prior to and during the Coulomb explosion, thus the precursor ion spends more time in the field than do diatomic systems such as N_2 and O_2.

In summary, this study provided a better understanding of the bending and alignment motion of the molecules in an intense field and is one step in the path to understand laser control of the molecules, which will become practical as more details of the dynamics are revealed and better laser and detection technologies are developed.

6.2 Future Work

Despite the experiments and the theoretical analyses being in agreement in this work, important details undergirding the physics responsible for the molecular dynamics in strong fields are still unknown. On the theoretical side, a full quantum treatment is necessary to understand the motion of nuclei as well as electrons as a function of time. On the experiment side, other triatomic molecules, such as N_2O (linear) and SO_2 (bent), should be studied under the same conditions and the results should be compared to the models we developed in order to check the validity and generality of the theories. Furthermore, molecular ionization leading to Coulomb explosion under different pulse widths and pulse shapes should be investigated to understand the evolution of the molecules in the field. In particular, if the laser pulse is shaped so that the 2-body and 3-body channels of NO_2 are separated, details of both channels might be revealed with less confusions. For ejection anisotropy, experiments with different laser pulse widths can be used to measure the degree of dynamic alignment as a function of time. If pump-probe schemes are employed to pre-align the molecules, the ionization probability as a function of orientation angle can be measured to obtain information about the geometric alignment effect. In this study, the arrival time of the charges collected on the image was determined to within a few tens of nanoseconds. If a multinode photon-multiplier could be employed [141, 142] along with the digital camera to achieve better temporal resolution (on the order of 200 ps as claimed in Ref. [142]) in charge detection without compromising the high detection rate, abundant details of the dynamics could be obtained.

Appendix A

Classical Pendulum Equation of Motion

This appendix shows that a classical pendulum equation of motion can be solved for general values of the angle and the rotation time can be derived with the *elliptic integral of the first kind* [115].

A classical pendulum equation of motion for the dynamic alignment of a polarized molecule with a dipole moment ($\vec{\mu}$) in an external field ($\vec{E}$) has the form of [36, 96]

$$\ddot{\theta} = -\frac{\vec{\mu} \times \vec{E}}{I_m} = -\frac{\mu E}{I_m} \sin\theta, \tag{A.1}$$

where θ is the angle between the field and the molecular axis, $I_m = mR_{mol}^2/2$ is the moment of inertia of the molecule with m as the mass of the atom at both ends of the molecule. The damping term ($2\dot{R}_{mol}\dot{\theta}/R_{mol}$) [42, 97], essentially the variation of R_{mol} in time, is ignored because it has been shown to be small at intensities of 10^{15} W/cm^2 [97]. The dipole moment can be estimated with the concept of charge-resonance states [107, 108]. In enhanced ionization, the electron displacement or field-induced dipole moment is mostly due to the charge-resonance states and proportional to the bond length [73], so that the dipole moment can be taken as $\mu_{CR} \simeq \zeta e R_{mol} \cos\theta$, where ζ is nearly constant and at best a slowly varying function of R_{mol} and θ, depending on how μ_{CR} and R_{mol} are related in diatomic or triatomic molecules. For diatomics, the value is $\zeta = 0.5$ [107, 108], while it was

shown as ~ 0.4 in H_3^{2+} and H_3^+ [93]. As μ_{CR} is employed, the equation of motion (Eq. A.1) becomes

$$\ddot{\theta} = -\frac{\zeta e E R_{mol}}{I_m} \sin\theta\cos\theta, \qquad \ddot{\Theta} = -\frac{\zeta e E R_{mol}}{I_m} \sin\Theta, \tag{A.2}$$

where $\Theta = 2\theta$, and the characteristic frequency of the pendulum at small Θ approximation can be expressed as

$$\omega_{CR} = \sqrt{\frac{2\zeta e E}{m R_{mol}}}. \tag{A.3}$$

Although ω_{CR} by no means reflects the complexity of the ejection anisotropy in enhanced ionization quantitatively, it provides qualitative analysis for how the strength of dynamic alignment of molecules may vary. It reads from the expression of ω_{CR} (Eq. A.3) or

$$\tau_{CR} = \frac{2\pi}{\omega_{CR}} = \pi\sqrt{\frac{2mR_{mol}}{\zeta e E}}, \tag{A.4}$$

that dynamic alignment grows as the mass of the atom, size of the molecule, or laser frequency decreases and as the laser field increases.

For general values of Θ, the equation of motion,

$$\ddot{\Theta} = -\omega_{CR}^2 \sin\Theta, \tag{A.5}$$

can be integrated over Θ, and yield [115, 143],

$$\int_0^\Theta \frac{\mathrm{d}^2\Theta}{\mathrm{d}t^2}\mathrm{d}\Theta = -\int_0^\Theta \omega_{CR}^2 \sin\Theta \mathrm{d}\Theta. \tag{A.6}$$

Using

$$\int_0^\Theta \frac{\mathrm{d}^2\Theta}{\mathrm{d}t^2}\mathrm{d}\Theta = \int_0^\Theta \frac{\mathrm{d}^2\Theta}{\mathrm{d}t^2}\frac{\mathrm{d}\Theta}{\mathrm{d}t}\mathrm{d}t = \frac{1}{2}\int_0^\Theta \mathrm{d}\left(\frac{\mathrm{d}\Theta}{\mathrm{d}t}\right)^2 = \frac{1}{2}\left(\dot{\Theta}^2 - \dot{\Theta}^2|_{\Theta=0}\right) \tag{A.7}$$

and

$$-\int_0^{\Theta} \omega_{CR}^2 \sin\Theta \mathrm{d}\Theta = \omega_{CR}^2(\cos\Theta - 1) = -2\omega_{CR}^2 \sin^2\frac{\Theta}{2}, \tag{A.8}$$

Eq. A.6 becomes

$$\frac{1}{2}\left(\dot{\Theta}^2 - \dot{\Theta}^2|_{\Theta=0}\right) = -2\omega_{CR}^2 \sin^2\frac{\Theta}{2}. \tag{A.9}$$

If the maximum angle of the motion is $\Theta_0 = 2\theta_0$ and $\dot{\Theta}|_{\Theta=\Theta_0} = 0$,

$$\dot{\Theta}^2|_{\Theta=0} = 4\omega_{CR}^2 \sin^2\frac{\Theta_0}{2}. \tag{A.10}$$

Equation A.9 becomes

$$\dot{\Theta}^2 = 4\omega_{CR}^2(\sin^2\frac{\Theta_0}{2} - \sin^2\frac{\Theta}{2}). \tag{A.11}$$

Define $k = \sin^2\frac{\Theta_0}{2} < 1$, then $k = \sin^2\theta_0$, and

$$\frac{\mathrm{d}\Theta}{\mathrm{d}t} = 2\omega_{CR}\sqrt{k - \sin^2\frac{\Theta}{2}}, \tag{A.12}$$

or

$$\mathrm{d}t = \frac{\mathrm{d}\Theta}{2\omega_{CR}\sqrt{k - \sin^2\frac{\Theta}{2}}}. \tag{A.13}$$

Define $\sin^2\frac{\Theta}{2} = k\sin^2\phi = \sin^2\frac{\Theta_0}{2}\sin^2\phi$ with $-\Theta_0 \le \Theta \le \Theta_0$ and $-\pi/2 \le \phi \le \pi/2$,

then

$$\sqrt{k - \sin^2\frac{\Theta}{2}} = \sqrt{k(1 - \sin^2\phi)} = \sqrt{k}\cos\phi, \tag{A.14}$$

From the definition of ϕ,

$$\begin{aligned} \sqrt{k}\cos\phi\mathrm{d}\phi &= \frac{1}{2}\cos\frac{\Theta}{2}\mathrm{d}\Theta, \\ \frac{\mathrm{d}\Theta}{2\sqrt{k - \sin^2\frac{\Theta}{2}}} = \frac{\mathrm{d}\Theta}{2\sqrt{k}\cos\phi} &= \frac{\mathrm{d}\phi}{\cos\frac{\Theta}{2}} = \frac{\mathrm{d}\phi}{\sqrt{1 - k\sin^2\phi}}. \end{aligned} \tag{A.15}$$

Therefore,

$$\mathrm{d}t = \frac{\mathrm{d}\phi}{\omega_{CR}\sqrt{1 - k\sin^2\phi}}, \tag{A.16}$$

As the molecule moves from $\Theta = \Theta_0$ ($\theta = \theta_0$) and $\phi = \pi/2$ to $\Theta = 0$ ($\theta = 0$) and $\phi = 0$, it takes a quarter of the period of the motion,

$$T_{\theta_0} = \tau/4 = \frac{1}{\omega_{CR}}\int_0^{\pi/2} \frac{\mathrm{d}\phi}{\sqrt{1 - k\sin^2\phi}} = \frac{K(k)}{\omega_{CR}}, \tag{A.17}$$

where the integral is the *elliptic integral of the first kind*, $K(k) = \int_0^{\pi/2} \frac{\mathrm{d}\phi}{\sqrt{1-k\sin^2\phi}}$, with $k = \sin^2\theta_0$ [115]. The rotation time (T_θ) can also be expressed by the small-angle period (τ_{CR}) as

$$T_\theta = \frac{K(\sin^2\theta)}{\omega_{CR}} = \frac{K(\sin^2\theta)\tau_{CR}}{2\pi} = K(\sin^2\theta)\sqrt{\frac{mR_{mol}}{2\zeta eE}}. \tag{A.18}$$

Appendix B

Charge Arrival Position and Time of Flight

Given the initial velocity of the ejected ion along with its charge and mass, it is possible to calculate where and when it will strike either the image or TOF MCP of the spectrometer (Sec. 3.2). The structure of the spectrometer is shown in Fig. 3.6. The calculations of arrival position and time on the image MCP [100] are given in Sec. B.1, while the flight time to the TOF MCP is given in Sec. B.2.

B.1 Charge Arrival Position and Time on Image MCP

The two coordinate systems used in the calculation for the image side are shown in Fig. B.1. The first, xyz, has its origin located at the focal point of the laser with its x axis parallel to $k-$vector of the laser beam. The second, XYZ, is attached to the surface of the MCP a distance l from the focal point with the XY-plane in the surface. The origin of the XYZ system locates the center of mass of the dynamics in the XY-plane. The x and Y axes are parallel as are the line joining the origins of the axes and the static electric field. A charge, qe with e as the elementary charge, ejected from the focal point in the direction (θ, ϕ) with initial kinetic energy $\mathcal{E}$ ($=mv_0^2/2$), has velocity components:

$$\begin{aligned} v_{0x} &= v_0 \cdot \sin\theta \cdot \cos\phi, \\ v_{0y} &= v_0 \cdot \sin\theta \cdot \sin\phi, \end{aligned} \tag{B.1}$$

$$v_{0z} = v_0 \cdot \cos\theta,$$

in the xyz system and land at point (X, Y) on the MCP given by:

$$\begin{aligned} X &= \frac{2l\cos\theta}{\epsilon}(\sqrt{\sin^2\theta\cdot\sin^2\phi+\epsilon}-\sin\theta\cdot\sin\phi), \\ Y &= \frac{2l\cos\phi\cdot\sin\theta}{\epsilon}(\sqrt{\sin^2\theta\cdot\sin^2\phi+\epsilon}-\sin\theta\cdot\sin\phi), \end{aligned} \tag{B.2}$$

where $\epsilon = qeEl/\mathcal{E}$ is the ratio between the electrostatic energy acquired in the field E pushing the charge toward the MCP (numerator) and the initial kinetic energy (denominator); l is the distance between the focal point and the detector. The time it takes the charge to reach the MCP is given by

$$t = \frac{\sqrt{m^2v_{0y}^2+2mqeEl}-mv_{0y}}{qeE}. \tag{B.3}$$

In the limit of large ϵ ($\geq$25), which is true for most of the experiments, Eq. B.2 reduces to

$$X \simeq \frac{2l\cos\theta}{\sqrt{\epsilon}}, \qquad Y \simeq \frac{2l\cos\phi\cdot\sin\theta}{\sqrt{\epsilon}}. \tag{B.4}$$

For the $\phi \simeq 0$ trajectories, Eq. B.2 further reduces to

$$X \simeq \frac{2l\cos\theta}{\sqrt{\epsilon}}, \qquad Y \simeq \frac{2l\sin\theta}{\sqrt{\epsilon}}, \tag{B.5}$$

and the ions fall on a circle of radius $R_{\mathcal{E}}$ given by

$$R_{\mathcal{E}} = 2\sqrt{\frac{l\mathcal{E}}{qeE}}. \tag{B.6}$$

In a general case, Eq. B.6 does not hold at most of the locations on the image because the ions are ejected into all directions. Even the image produced by an isotropic mono-energetic distribution of charges has contribution at $R < R_{\mathcal{E}}$

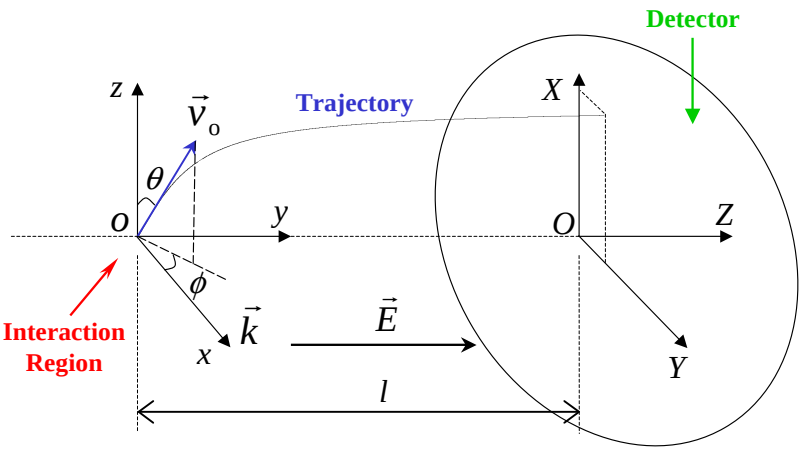

Figure B.1: Coordinate systems used for calculating the ion trajectory on the image side. The laser is focused at "o" and the wave vector $\vec{k}$ is in the x-direction. The center of mass of the dynamics is "O", which is the center of the image. The initial velocity of the ion is $\vec{v_0}$, which is pushed toward the detector by the static field $\vec{E}$. The field strength is $E = V_{int}/l$ (Fig. 3.6). The detector, $XY-$plane, is parallel to $xz-$plane.

because of the $\phi \neq 0$ components for large θ. When the ions have multiple energies, the higher energy trajectories with $\phi \neq 0$ will distort the distribution of the lower energy components. However, for a given energy and ejection angle θ, trajectories with $\phi \approx 0$ have the largest density of points on the image. These trajectories collect on a circle on the image as θ changes and Eq. B.6 holds for them. On the other hand, if θ were restricted to small angles (i.e., charges ejected nearly parallel to $z-$axis) and the angular distribution were cylindrically symmetric about the $z-$axis which is true in a laser field with the linear polarization also parallel to $z-$axis, energetic charges would appear at a distance from the center of the image given by Eq. B.6. Thus, the energy ($\mathcal{E}$) and momentum ($p = mv_0$) can be determined from the peak

position along the $X-$axis ($X_{peak} = R_{\mathcal{E}}$ as $Y = 0$) on the image as

$$\mathcal{E} \simeq \frac{qeE}{4l} X_{peak}^2, \qquad p \simeq \sqrt{\frac{qeEm}{2l}} X_{peak}. \tag{B.7}$$

In a multi-component ejection, Eq. B.7 holds for each component if the peaks are spatially separated on the image. In practice, the potential $V_{int} = E \cdot l$ or $V_4 = 4V_{int}/3$ (Fig. 3.6) is obtained directly and R_{peak} is used for peaks on and off the axis instead of X_{peak}. Thus, Equation B.7 is rewritten as

$$\begin{aligned} \mathcal{E} &\simeq \frac{qeV_{int}}{4l^2} R_{peak}^2 = \frac{3qeV_4}{16l^2} R_{peak}^2, \\ p &\simeq \sqrt{\frac{qemV_{int}}{2}} \frac{R_{peak}}{l} = \sqrt{\frac{3qemV_4}{2}} \frac{R_{peak}}{2l}. \end{aligned} \tag{B.8}$$

Since the radius R is proportional to the momentum p, the image is often called the momentum distribution or momentum spectrum.

The radius on the image is measured by the pixel on the images. The correspondence of the pixel and the image size on the phosphor screen is calibrated by taking an image of a thin ruler placed at the screen. In order to accommodate the full size of the screen in the camera frame, the calibration κ_{calib} is adjusted to be about 0.3 mm per pixel by varying the distance from the camera to the screen and changing the focus of the camera lens.

In order for Eqs. B.2 and B.3 to hold exactly, the static field in the spectrometer needs to be uniform. The uniformity of the static field was checked by measuring the energy and momentum of protons ejected from H_2 under the influence of a linearly polarized laser field while the static field was varied. In linear polarization, protons are ejected mostly within a small angular spread around the z-axis so that their

momenta nearly obey Eq. B.7 or B.8. As the static field V_4 increases, the peak radii of the protons decrease. However, if the laser intensity is fixed (1.5×10^{15} W/cm^2), the proton momenta or energies do not change so that the product $R\sqrt{V_4}$ or R^2V_4 (Eq. B.8) should stay constant as V_4 varies. Figure B.2 shows the measured momenta are consistent with a constant for each ejection channel within the uncertainty of the measurement, and confirms the uniformity of the static field. Since the energy is proportional to V_4, the uncertainty of energy measurement can be treated as an estimate of the non-uniformity of the static field. The uncertainty of energy measurement at five different V_4 (6%) was calculated as [144]

$$\bar{\sigma} = \sqrt{\frac{1}{N(N-1)} \sum_{i=1}^{N} \sigma_i^2}, \tag{B.9}$$

with $N = 5$. Thus, the non-uniformity of the static field was estimated as about 6%. At the same time, the inner peak (H + H$^+$ dissociation) of protons should have an energy of about 0.5 eV [21] under current conditions (800 nm, 100 fs, and 1.5×10^{15} W/cm^2), which corresponds to a momentum of 8.2 a.u.. Assuming these values (0.5 eV and 8.2 a.u.) are correct, the errors in the measurement (0.53 eV and 8.4 a.u.) were about 6% and 3% for energy and momentum, respectively, which gave an overall estimate about the uncertainty of the determination of energy and momentum with Eq. B.8, including the uncertainties of l, V_4, and calibration κ_{calib}.

B.2 Time of Flight

On the TOF side of the spectrometer, as shown in Fig. B.3, the flight time of am ejected ion can be calculated as described in this section.

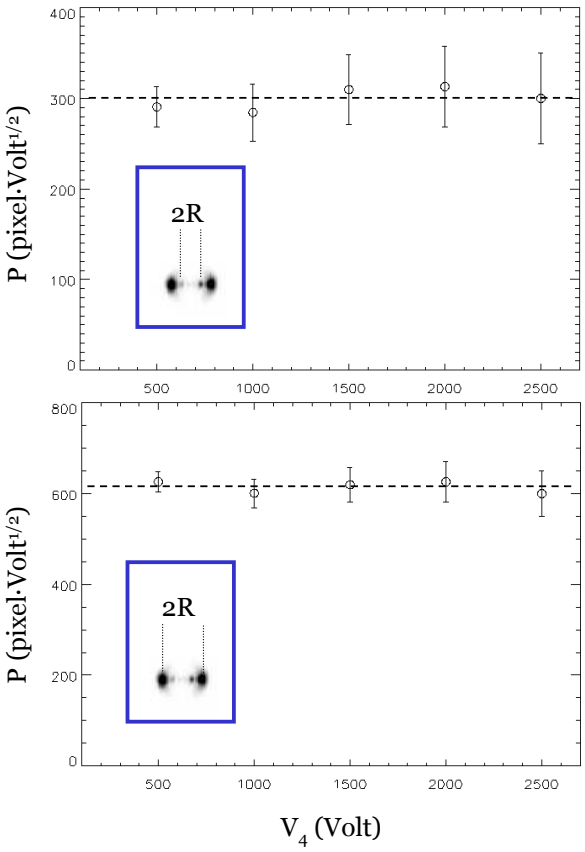

Figure B.2: Momenta of protons ejected from H_2 under the influence of a linearly polarized laser field at 1.5×10^{15} W/cm^2 as functions of the static field in the spectrometer (V_4, see Fig. 3.6). Since the image calibration, charge qe, mass m and distance l (Fig. B.1) are the same, the momentum p is expressed by $R_{peak} \cdot \sqrt{V_4}$ (Eq. B.8), where R_{peak} is the radius of the proton peak in the unit of pixel. The data points were taken with V_4 varying from 500 to 2500 volts with 500 volts at each step. The dashed lines are the average of the five points in each plot. The error bars correspond to ± 1 pixel which is the uncertainty of the determination of the peak positions. The upper plot is for the inner peak from the low-energy dissociation, while the lower one for the outer peak from Coulomb explosion. The insets (blue rectangles) are the image taken at $V_4 = 2000$ volts to show where R_{peak} was measured.

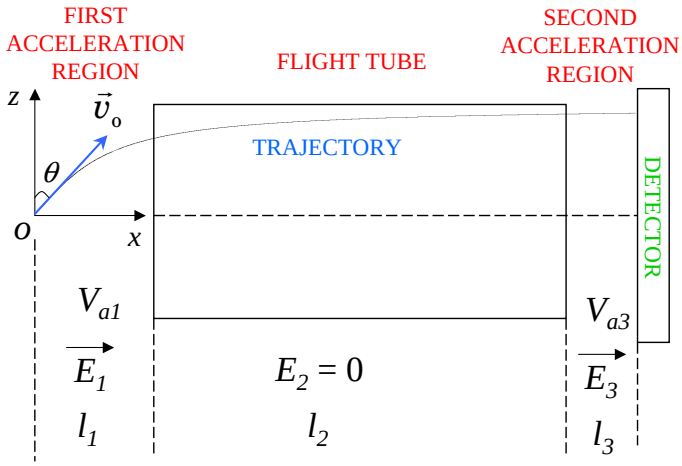

Figure B.3: Structure and coordinate system of TOF spectrometer. The laser is focused at "o" and propagates in or out of the paper. The $x-$axis is parallel to the external fields $\vec{E_1}$ and $\vec{E_3}$ and the flight tube, while z-axis is parallel to the detector, which is a 50-mm-diameter MCP with 40-mm active area. The initial velocity of the ion is $\vec{v_0}$. The distances and potentials are, according to Fig. 3.6, $l_1 = 19.05$ mm, $l_2 = 140$ mm, $l_3 = 30$ mm, and $V_{a1} = V_4/4 = 500$ volts, $V_{a3} = 300$ volts.

The ion $(qe,\ m)$ with initial velocity $\vec{v_0}$ is pushed by $\vec{E_1}$ in the first acceleration region, drifts through the flight tube, then is accelerated again in the second acceleration region to strike the detector (Fig. 3.6). The flight times in these three regions are

$$\begin{aligned} t_1 &= \frac{ml_1}{qeV_{a1}}\left(\sqrt{v_0^2\sin^2\theta + \frac{2qeV_{a1}}{m}} - v_0\sin\theta\right), \\ t_2 &= l_2 \Big/ \sqrt{v_0^2\sin^2\theta + \frac{2qeV_{a1}}{m}}, \\ t_3 &= \frac{ml_3}{qeV_{a3}}\left(\sqrt{v_0^2\sin^2\theta + \frac{2qe(V_{a1}+V_{a3})}{m}} - \sqrt{v_0^2\sin^2\theta + \frac{2qeV_{a1}}{m}}\right), \end{aligned} \tag{B.10}$$

where $V_{a1} = V_4/4$. The total time-of-flight is $t_{TOF} = t_1 + t_2 + t_3$. The transverse displacement on the detector is $d_T = v_0 t_{TOF}\cos\theta$ and all the ions with $d_T(v_0, \theta = 0) \leq R_{MCP}$, where $R_{MCP} = 20$ mm is the radius of the MCP, are detected. For ions with $d_T(v_0, \theta = 0) > R_{MCP}$, only the ones with an ejection angle θ greater than a

certain limit θ_m are detected, which can be determined by solving the equation

$$d_T = v_0 t_{TOF} \cos\theta_m = R_{MCP}. \tag{B.11}$$

There are two solutions with $\theta_{m+} > 0$ and $\theta_{m-} < 0$ for forward and backward ions initially ejected toward and away from the detector and their acceptance angles are defined as $\theta_{\pm}^{Acc} = \pi/2 - |\theta_{m\pm}|$. The acceptance angle can be measured from the experiment. When the linear polarization axis of the laser is rotated relative to the TOF axis from parallel to perpendicular, the TOF signal strength would decrease due to a finite acceptance angle since the ions generated are ejected primarily along the polarization direction. The acceptance angle can be estimated at the rotation angle where the signal strength drops to a half of its value at parallel direction. The acceptance angles estimated for N^{2+} from N_2 explosions (about 11 eV) and H^+ from H_2 (about 2.5 eV) are roughly 40° and 45°, respectively.

Under the condition $v_0 = 0$ or $\theta = 0$, Eq. B.10 reduces to

$$\begin{aligned} t_1 &= l_1\sqrt{\frac{2qeV_{a1}}{m}}, \\ t_2 &= l_2\sqrt{\frac{m}{2qeV_{a1}}}, \\ t_3 &= \frac{l_3}{V_{a3}}\sqrt{\frac{2m}{qe}}(\sqrt{V_{a1}+V_{a3}} - \sqrt{V_{a1}}). \end{aligned} \tag{B.12}$$

If $v_0 \neq 0$ and $\theta \neq 0$, the time difference of the forward and backward ions is

$$\Delta t = t_{TOF}(-\theta) - t_{TOF}(\theta) = \frac{2ml_1 v_0 \sin\theta}{qeV_{a1}}. \tag{B.13}$$

Then the longitudinal momentum component $p_\parallel = mv_0 \sin\theta$ and the energy associated with it $\mathcal{E}_\parallel = m(v_0 \sin\theta)^2/2$ can be calculated from Δt as

$$p_\parallel = \frac{V_{a1}}{2l_1} qe\Delta t, \qquad \mathcal{E}_\parallel = \frac{V_{a1}^2}{8ml_1^2}(qe\Delta t)^2. \tag{B.14}$$

Appendix C

Image Processing

The raw images (camera frames) streamed to the SCSI drive from the digital camera are stored by recording the value of each pixel. Since only a few percent of the pixels (100 out of 16,384) have values higher than the background (Page 53), these frames can be compressed dramatically into much smaller files [126]. The procedure of image compression and recovery is given in Sec. C.1. At the same time, each ion striking the MCP illuminates a cluster of adjacent pixels on the CCD camera. The procedure to group the adjacent pixels into a cluster and to determine the centroid of each cluster is given in Sec. C.2.

C.1 Image Compression and Recovery

The flowchart of image compression is shown in Fig. C.1. The basic idea is to record only the pixels with values higher than the background noise (nonzero pixels) and get rid of the rest (zero pixels), which occupy most of the storage space of camera frames [126]. In the compressed frames, each nonzero pixel is recorded as a pair of bytes, where the first byte stores the signal value of this pixel and the second byte stores the position. In general, the position of a pixel in a 128×128 image could be as high as $2^{14}-1$, which cannot be stored in one byte. Thus, a relative position smaller than 256 (2^8) counted from a marker instead of an absolute position counted

from the first pixel of the frame is used. The marker is inserted before the byte pair of the pixel when necessary, and also recorded as a pair of bytes. The first byte of the marker is always zero to distinguish from the pairs for the nonzero pixels; the second byte stores the shift in the unit of 256 from the last marker or the first pixel if this is the first marker in this frame. Therefore, the absolute position of a pixel is the summation of the shifts in all previous markers multiplied by 256 and plus the relative position. A pair of zeros is placed at the end of each frame as a separator in a compressed file with multiple frames. A counter file, containing the numbers of nonzero pixels and pairs of bytes used for each frame, and a summary text file are generated along with the compressed image file for easy indexing. In such a manner, the size of the compressed images is only a few percent of the size of the camera frame file. A typical compressed image file containing 100,000 to 500,000 frames only occupies several to a few hundred MB instead of a few GB of disk space and can be stored or transfered to a CD or a flash drive easily. First five nonzero pixels in a sample camera frame and their corresponding pairs of bytes in the compressed image file including the markers are listed in Table C.1.

The flowchart of image recovery from the compressed file is shown in Fig. C.2. As the nonzero pixels are placed to their corresponding positions in a blank frame, and the rest of the pixels are set to be zero, this compression–recovery process also eliminates the background of the frames. Figure C.3 shows a comparison of two images before and after the background elimination.

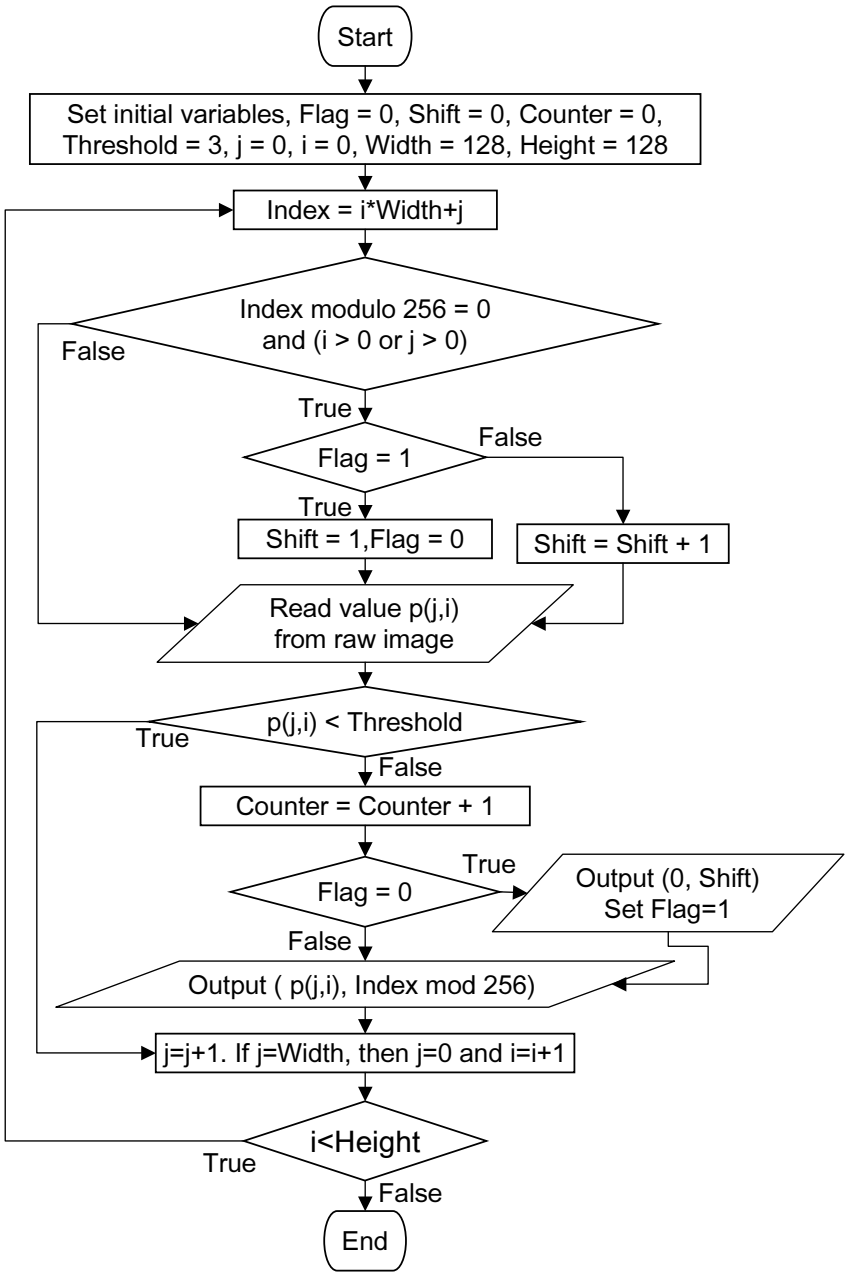

Figure C.1: Flowchart of the image compression process. *Flag* and *Shift* are used to compute the shift which will be placed in the marker. *Counter* is used to count the number of nonzero pixels in this frame.

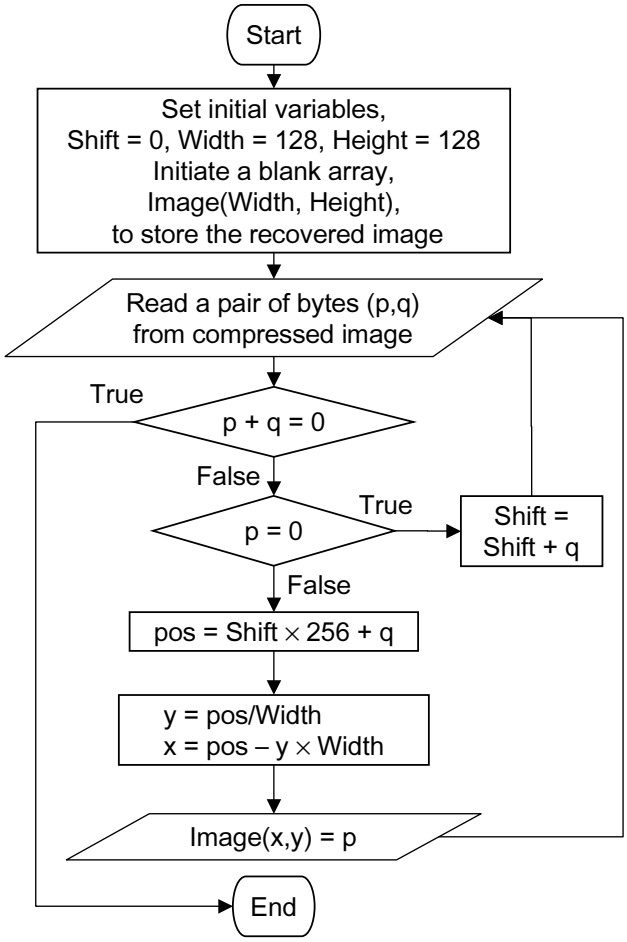

Figure C.2: Flowchart of the process of image recovery from the compressed image file.

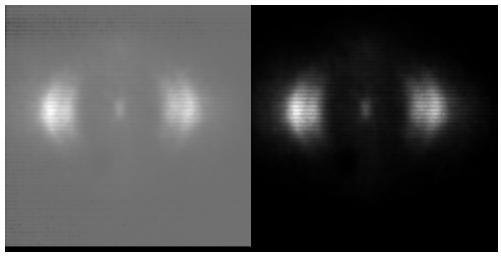

Figure C.3: Comparison of two images before (left) and after (right) the background elimination. Both images are composed by 10,000 single frames, each of which corresponds to one laser pulse.

Table C.1: First five nonzero pixels in a camera frame and their corresponding pairs of bytes (a, b) in the compressed image file including the markers (the pairs with $a = 0$). The position of each pixel (P) is computed as $P = x + y * w$, where x and y are the coordinates of the pixel on the frame and $w = 128$ is the width of the frame. The position can also be computed from (a, b) as $P_i = b_i + 256 \times \sum_{j<i, a_j=0} b_j$.

i	Signal	Coordinates (x, y)	Position (P)	pair of bytes (a, b)
1		marker		0, 21
2	4	89, 43	5593	4, 217
3	4	90, 43	5594	4, 218
4		marker		0, 1
5	4	89, 44	5721	4, 89
6	4	90, 44	5722	4, 90
7		marker		0, 1
8	4	53, 47	6069	4, 181

C.2 Image Clustering

In general, each ion striking the MCP illuminates a cluster of adjacent pixels on the CCD camera. The number of pixels within a cluster is typically between 1 and 5. The following procedure is carried out to determine the centroid of such a cluster. First, all the adjacent nonzero pixels around the one with the largest signal value on an image are identified as a cluster, then this step is repeated for the nonzero pixels left on the image. Each time after a cluster is identified, it is tested to determine whether it is a new cluster or a part of one previously identified one, depending on the distance between the two clusters and the values of their pixels. Then, the pixel with the largest value in a cluster is defined as the center or centroid. If there are two or more pixels with the same peak value, the one closest to the center of mass of the cluster is defined as the center or centroid, where the signal of a pixel is used to calculate the center of mass. Details of the procedure are

shown as a flowchart in Fig. C.4.

A sample of an H_2 image before and after its pixels were grouped into clusters is shown in Fig. C.5. Five clusters were identified in the magnified part of the image. The measured occurrence frequencies (F) as a function of the number of pixels in a cluster on the images of five molecular Coulomb explosions are listed in Table C.2. The molecules are H_2 (H^+), N_2 (N^{2+}), O_2 (O^{2+}), CO_2 (C^{2+} and O^{2+}) and NO_2 (N^{2+} and O^{2+}). The probability (P) can be calculated as the frequency divided by the total number of clusters (N_{tot}, sum of all the frequencies)

$$P_x = \frac{F_x}{N_{tot}}, \quad N_{tot} = \sum_{x=1}^{N} F_x, \tag{C.1}$$

where x is the number of pixels in a cluster, N is the maximum possible number of pixels found in a cluster (the limit of N is 128×128, where the entire image is found to be one cluster). The mean (μ) and standard deviation (σ) of the frequency curve can be calculated as

$$\begin{aligned} \mu &= \sum_{x=1}^{N} x \cdot P_x, \\ \sigma &= \sqrt{\sum_{x=1}^{N} (x-\mu)^2 \cdot P_x}. \end{aligned} \tag{C.2}$$

The measured parameters (μ, σ, and N_{tot}) are listed in Table C.3. The histograms showing how the frequency varies as a function of the number of pixels in each cluster for H_2, CO_2 and NO_2 images are shown in Fig. C.6.

In an event-counting experiment similar to the occurences of the clusters described above, a Poisson distribution, which is the limit of a binomial distribution [145], is often used to fit the probability (P_x). If the probability for event A to occur

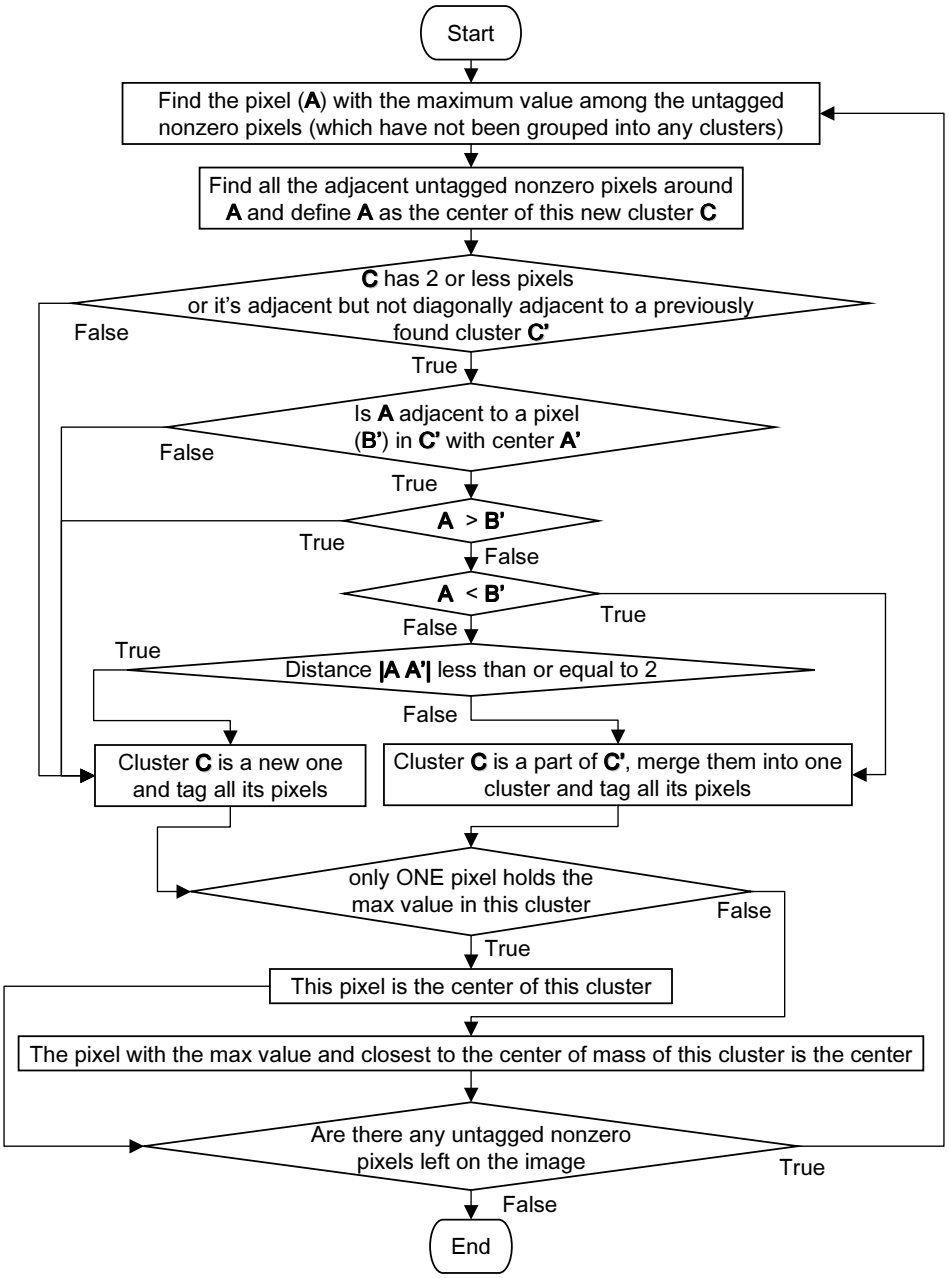

Figure C.4: Flowchart of the procedure to determine the centroid of a cluster on an image. The adjacent pixels $p_1(i_1, j_1)$ and $p_2(i_2, j_2)$ are determined when $|i_1 - i_2| \leq 1$ and $|j_1 - j_2| \leq 1$. In the special case of $|i_1 - i_2| = |j_1 - j_2| = 1$, they are called diagonally adjacent, as pixels 1 and 2 shown in Fig. 4.8g.

Table C.2: Occurrence frequency as a function of the number of pixels (x) in a cluster measured in H_2 (H^+), N_2 (N^{2+}), O_2 (O^{2+}), CO_2 (C^{2+} and O^{2+}) and NO_2 (N^{2+} and O^{2+}) images. Laser pulses are linearly polarized with an intensity of 2×10^{15} W/cm^2. The measured μ, σ (Eq. C.2) and N_{tot}, as well as the number of frames involved, are listed in Table C.3.

x	H_2	N_2	O_2	CO_2	NO_2
1	1469367	82847	204837	2351480	427780
2	609562	40252	101575	2694049	448808
3	226543	21661	53661	1841137	219042
4	97789	11857	26926	2336344	322707
5	32359	4098	10185	1306536	104465
6	14026	1883	4649	1135043	76893
7	5667	785	1867	834526	39714
8	2264	249	661	655483	18766
9	865	87	222	429286	6463
10	351	31	77	267040	1822
11	143	5	39	195071	769
12	37	6	10	134708	267
13	27		2	95006	113
14	3		1	65930	34
15	1		0	44568	14
16	2		1	29150	3
17				19503	2
18				12811	2
19				8279	
20				5417	
21				3479	
22				2178	
23				1320	
24				842	
25				501	
26				330	
27				178	
28				85	
29				60	
30				36	
31				22	
32				9	
33				2	
34				3	
35				1	
36				1	
37				1	

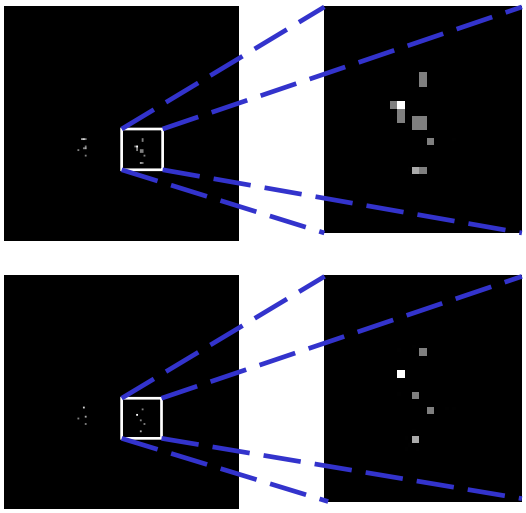

Figure C.5: A sample of the results of the cluster procedure. The upper left image and its magnified part (upper right) is one of the 500,000 single frames of H_2 Coulomb explosions taken with linearly polarized pulses with laser intensity of 2×10^{15} W/cm^2. The lower images are the same image after being clustered and show only the centroids of the clusters.

Table C.3: The measured μ, σ (Eq. C.2) and N_{tot} from the occurrence frequency as a function of the number of pixels (x) in a cluster for H_2, N_2, O_2, CO_2 and NO_2 images (Table C.2), as well as the number of frames involved.

	H_2	N_2	O_2	CO_2	NO_2
μ	1.66	1.93	1.92	4.26	2.86
σ	1.03	1.25	1.24	3.01	1.74
N_{tot}	2459042	163761	404713	14470415	1667664
frames	500000	200000	200000	500000	500000

is P, the probability for the number or frequency of the occurrence of event A to be x in N *independent* tests is given by a binomial distribution,

$$P(x|N) = \frac{N!}{x!(N-x)!} P^x (1-P)^{N-x}, \tag{C.3}$$

where the factor $\frac{N!}{x!(N-x)!}$ is the number of combinations of x objects chosen from a set of N divided by the number of permutations. As $N \to \infty$ and $P \to 0$, the product $P \cdot N$ approaches to a finite value μ, and Eq. C.3 becomes a Poisson distribution,

$$P_x = \frac{\mu^x}{x!} e^{-\mu}. \tag{C.4}$$

It is easy to show that both the mean and variance of Poisson distribution are equal to μ ($\mu = \sigma^2$). In practice, the value of x observed in one set of N tests will vary randomly – x can be any value between 0 and N. Thus, the set of N tests would be repeated many times (N_{tot}) and the frequency for event A to occur x times ($x = 1, 2, \cdots N$) is counted in the N_{tot} sets. The frequency as a function of x should approach a Poisson distribution as N approach infinity.

In our case, if we consider the probability to find x nonzero pixels in a cluster, finding a nonzero pixel in a cluster can be seen as event A and the maximum possible number of pixels in a cluster can be seen as the sample space – N is the number of the tests. The act of reading the value of each pixel and finding x nonzero pixels is equivalent to running N tests and finding x occurrences of event A. However, the tests (pixels) are not *independent* since a cluster requires its nonzero pixels are all adjacent. Thus, the probability for a cluster to have x pixels does not follow Eq. C.3 because the number of combinations of x *adjacent* pixels chosen from a set of N does not follow $\frac{N!}{x!(N-x)!}$. This can be seen in Fig. C.7, where the frequencies

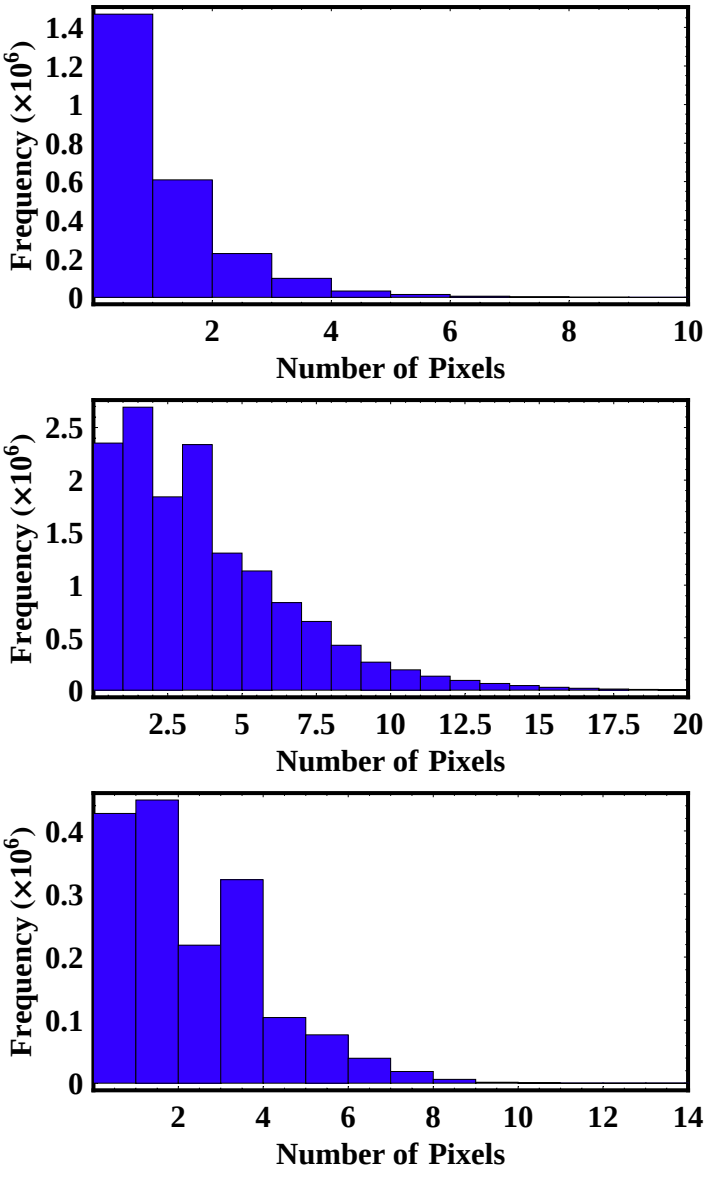

Figure C.6: Frequency (F_x) as a function of the number of pixels in each cluster. Laser pulses are linearly polarized with an intensity of 2×10^{15} W/cm^2. Upper: 500,000 frames of H_2 Coulomb explosions with measured $\mu = 1.66$, $\sigma = 1.03$, and $N_{tot} = 2.46{\times}10^6$; middle: 500,000 frames of CO_2 Coulomb explosions with measured $\mu = 4.26$, $\sigma = 3.01$, and $N_{tot} = 1.45{\times}10^7$; lower: 500,000 frames of NO_2 Coulomb explosions with measured $\mu = 2.86$, $\sigma = 1.74$, and $N_{tot} = 1.67{\times}10^6$.

as a function of the number of pixels in each cluster for H_2, CO_2 and NO_2 images are plotted with fitting Poisson distributions. The fitting curves are narrower than the experimental frequencies; the values of μ for all three molecules calculated by Eq. C.2 are larger than the corresponding fitting parameters. The experimental frequencies are apparently super-poissonion.

As shown in Table C.2, the maximum number of pixels in a cluster for CO_2 is much higher than H_2 and NO_2. It is obvious that the more pixels are included in a cluster, the more likely this cluster could be actually illuminated by more than one charges landing closely on the detector. Thus, it needs to be tested for CO_2 whether the number of pixels in a cluster would affect the results of coincidence measurement (Sec. 4.3). As described in Sec. 4.3, valid clusters in the coincidence measurement are restricted to those having a maximum number of pixels M to minimize the inclusion of clusters, each of which corresponds to two or more ions landing near each other. To test how M would affect the coincidence measurement, angular distributions for CO_2 Coulomb explosions ($CO_2^{6+} \rightarrow O^{2+} + C^{2+} + O^{2+}$) were measured by *coincidence imaging* (Sec. 4.3) with different M at two bond angles (180° and 173°). The test showed that the value of M had little effect on the angular spread measurement (Fig. C.8). The standard deviation of angular spreads ($\Delta\theta_g$), measured with M between 6 and 15, was less than 1% for both bond angles in the test. However, a cluster with large number of pixels could still correspond to multiple charges landing closely on the detector. Therefore, in *coincidence imaging* measurements, M was chosen so that the probability, $P_x|_{x=M}$ (Eq. C.1), drops to about 10% of the peak value in order to eliminate counting multiple charges as one.

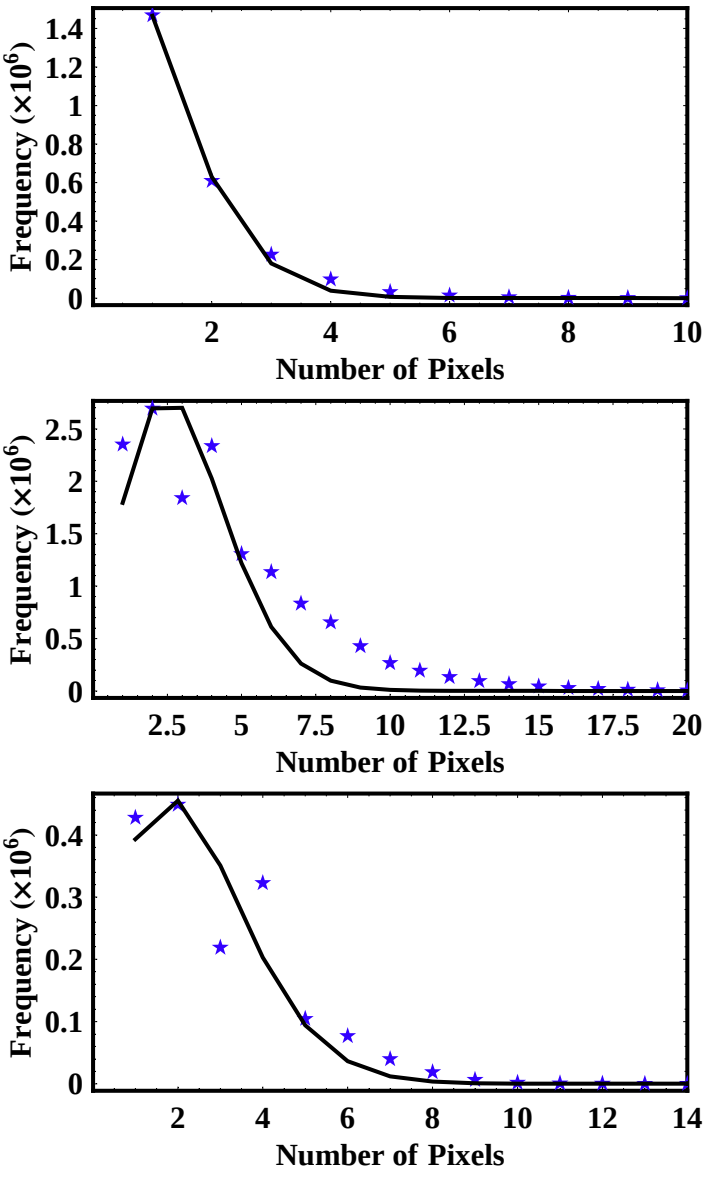

Figure C.7: Frequency as a function of the number of pixels in each cluster. The data are the same as in Fig. C.6. In order to be compared to the fitting curves, the data were plotted as stars instead of histograms. The solid curves are Poisson distributions, $g(x) = g_0 \frac{\mu^x}{x!} e^{-\mu}$, where x is the number of pixels in a cluster. The fit parameters are, upper (H_2): $\mu = 0.86$ and $g_0 = 4.0{\times}10^6$; middle (CO_2): $\mu = 3.0$ and $g_0 = 1.2{\times}10^7$; lower (NO_2): $\mu = 2.3$ and $g_0 = 1.7{\times}10^6$.

For H_2, CO_2 and NO_2, the value of M was 4, 9, and 9, respectively.

Another distribution, invoked in the clustering process, is the number of clusters or charges collected in each frame. The ultimate limit of the number of clusters in a frame is the frame size – 128×128, which is the sample size N = 16,384, as the entire frame serves as the sample space. Then, the act of reading the entire frame and finding x clusters is equivalent to running N tests and finding x occurrence(s) of an event. This act is repeated as each frame is taken – N_{tot} is the total number of frames. Although these tests are still not absolutely independent because the ions ejected from the same parent molecule would land on the MCP with correlated momenta or positions, they are much more random than the tests for the number of pixels in a cluster. Thus, the probability or frequency of the number of clusters in a frame should more or less follow a Poisson distribution. The fitting Poisson distributions (solid curves) and the experimental frequencies for the frames in H_2, CO_2, and NO_2 images (same data sets as in Fig. C.7) agree with each other rather well as shown in Fig. C.9.

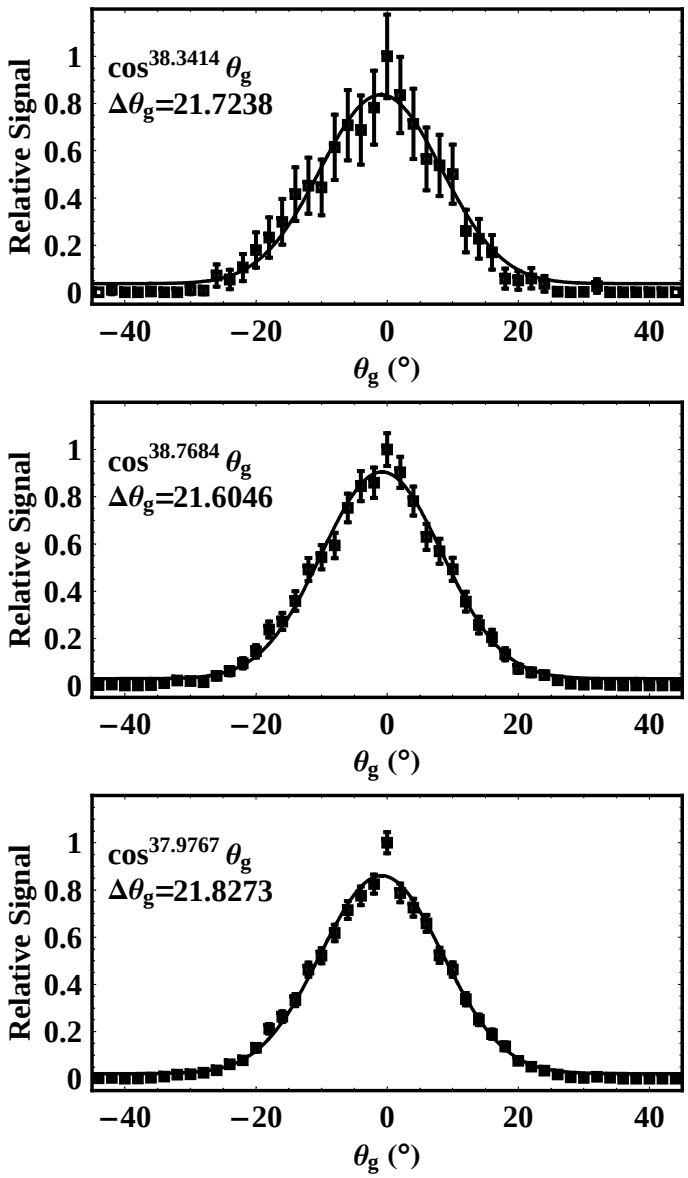

Figure C.8: Angular distributions for CO_2 Coulomb explosions ($CO_2^{6+} \rightarrow O^{2+} + C^{2+} + O^{2+}$) measured by *coincidence imaging* (Sec. 4.3) with different M at the bond angle of 180°. The values of M are 7, 9, 11 from the top to the bottom, respectively. The solid curves are the fitting functions $\cos^n \theta_g$ with the corresponding $\Delta\theta_g$ (full width at half maximum) labeled in the plots.

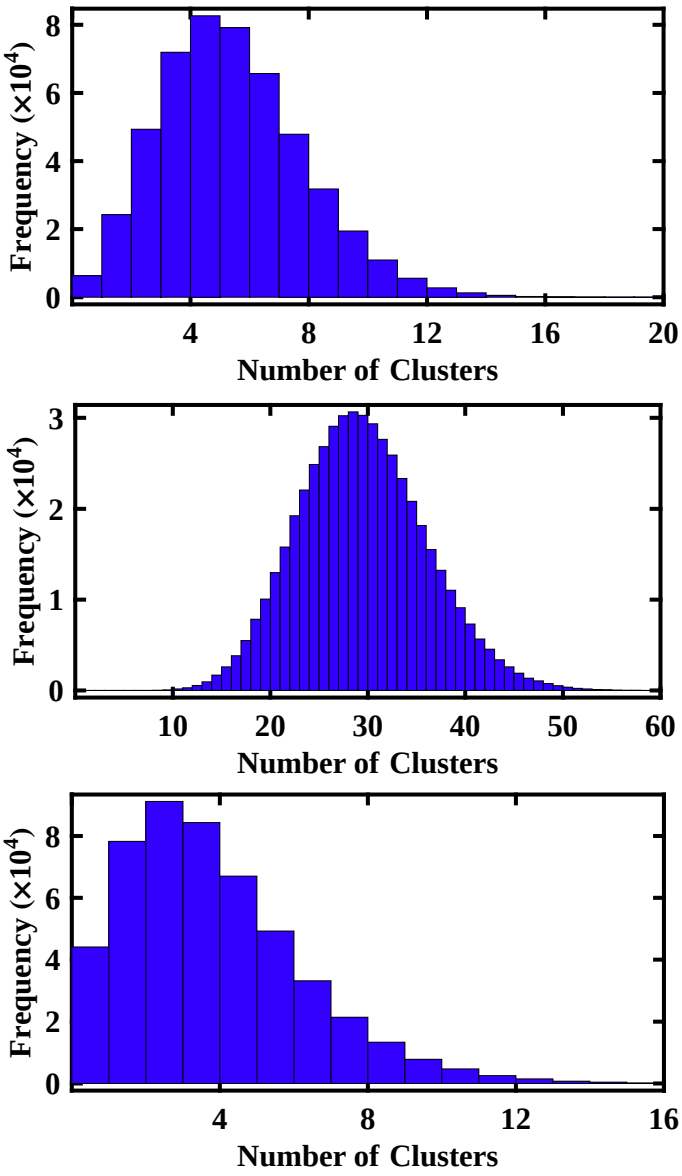

Figure C.9: Frequency as a function of the number of clusters in each frame. Laser pulses are linearly polarized with an intensity of 2×10^{15} W/cm^2. The histograms are the measured frequencies as a function of the number of clusters in each frame. The measured μ and σ in 500,000 frames are, upper (H_2): $\mu = 4.92$ and $\sigma = 2.45$; middle (CO_2): $\mu = 28.94$ and $\sigma = 6.56$; lower (NO_2): $\mu = 3.34$ and $\sigma = 2.44$.

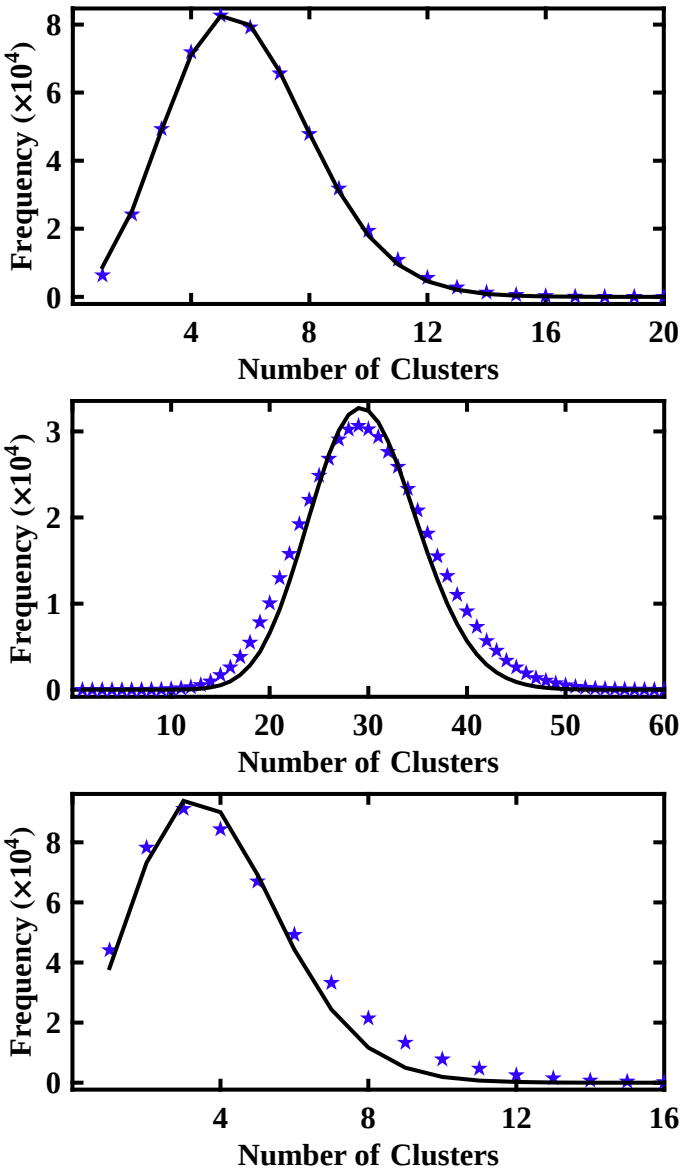

Figure C.10: Frequency as a function of the number of clusters in each frame. The data are the same as in Fig. C.9. Again, in order to be compared to the fitting curves, the data were plotted as stars. The solid curves are Poisson distributions, $g(x) = g_0 \frac{\mu^x}{x!} e^{-\mu}$, where x is the number of clusters in a frame. The fit parameters are, upper (H_2): $\mu = 5.81$ and $g_0 = 4.99\times10^5$; middle (CO_2): $\mu = 29.72$ and $g_0 = 4.47\times10^5$; lower (NO_2): $\mu = 3.84$ and $g_0 = 4.62\times10^5$.

Appendix D

Three-body Coulomb Explosion Kinematics

In general, Newton's equations of motion of a three-body system do not have analytic solutions. This appendix describes how the three-body Coulomb explosion encountered in this study is solved numerically so that the molecular structure where the explosion occurs is extracted from the momenta of the ejected ions measured in the experiments.

As a triatomic molecular ion (CO_2^{6+} or NO_2^{6+}, for example) explodes at $t = 0$ from a bond length R, the Hamiltonian in the center of mass coordinate system (Fig. D.1) takes the following form,

$$H = \frac{1}{2}\sum_{i=1}^{3} m_i \dot{r}_i^2 + \sum_{i>j}^{3} \frac{K q_i q_j e^2}{r_{ij}}, \tag{D.1}$$

assuming pure Coulomb forces between the three charges. The subscripts 1 and 2 represent the two outer ions (oxygen) while 3 represents the center ion (carbon or nitrogen). The mass, charge, position and momentum of each ion is given by m_i, $q_i e$, $\vec{r}_i = x_i\hat{x} + y_i\hat{y}$ and $\vec{p}_i \equiv m_i\dot{\vec{r}}_i(t)$, respectively, where e is the elementary charge. The separation between charges is given by $\vec{r}_{ij} = \vec{r}_i - \vec{r}_j$. The angle between vectors $\vec{r}_{13}$ and $\vec{r}_{23}$ at the time of the explosion, $t = 0$, is the bond angle θ_b. Then the equations of motion are,

$$\begin{aligned} \frac{\mathrm{d}}{\mathrm{d}t}p_{x_i} &= -\frac{\partial H}{\partial x_i}, \\ m_i\ddot{x}_i &= -\frac{\partial}{\partial x_i}\left(\frac{K q_i q_j e^2}{r_{ij}} + \frac{K q_i q_k e^2}{r_{ik}}\right), \end{aligned} \tag{D.2}$$

$$= \frac{Kq_iq_je^2(x_i - x_j)}{((x_i - x_j)^2 + (y_i - y_j)^2)^{3/2}} + \frac{Kq_iq_ke^2(x_i - x_k)}{((x_i - x_k)^2 + (y_i - y_k)^2)^{3/2}},$$

where i, j, $k = 1, 2, 3$. For symmetric 3-body Coulomb explosion, $m_O = m_1 = m_2$, $m_C = m_3$, $q_O = q_1 = q_2$, $q_C = q_3$, and $r_{13} = r_{23} = 0$ at $t = 0$. The subscripts O and C represent outer and center ions. Since the origin of the coordinate system is the center of mass and the third charge moves along the y-axis, $x_O = x_1 = -x_2$, $x_C = 0$, $y_O = y_1 = y_2$, $y_C = y_3$, and the equations of motion reduce to

$$\begin{aligned} m_O\ddot{x}_O &= \frac{Kq_O^2e^2}{4x_O^2} + \frac{Kq_Oq_Ce^2x_O}{(x_O^2 + (y_O - y_C)^2)^{3/2}}, \\ m_O\ddot{y}_O &= \frac{Kq_Oq_Ce^2(y_O - y_C)}{(x_O^2 + (y_O - y_C)^2)^{3/2}}, \\ m_O\ddot{y}_C &= \frac{2Kq_Oq_Ce^2(y_C - y_O)}{(x_O^2 + (y_O - y_C)^2)^{3/2}}, \end{aligned} \tag{D.3}$$

with the initial conditions,

$$x_O(0) = R\sin(\theta_b/2), y_O(0) = -\frac{R\cos(\theta_b/2)}{1 + 2m_O/m_C}, y_C(0) = \frac{R\cos(\theta_b/2)}{1 + m_C/m_O/2},$$
$$\dot{x}_O(0) = \dot{y}_O(0) = \dot{y}_C(0) = 0. \tag{D.4}$$

Without external force, the center of mass of the system does not move, $m_1y_1 + m_2y_2 + m_3y_3 = 0$, then $y_C = -\frac{2m_O}{m_C}y_O$. The equations of motion further reduce to

$$\begin{aligned} m_O\ddot{x}_O &= \frac{Kq_O^2e^2}{4x_O^2} + \frac{Kq_Oq_Ce^2x_O}{(x_O^2 + y_O^2(1 + 2m_O/m_C))^{3/2}}, \\ m_O\ddot{y}_O &= \frac{Kq_Oq_Ce^2y_O(1 + 2m_O/m_C)}{(x_O^2 + y_O^2(1 + 2m_O/m_C))^{3/2}}, \end{aligned} \tag{D.5}$$

with the initial conditions,

$$x_O(0) = R\sin(\theta_b/2), y_O(0) = -\frac{R\cos(\theta_b/2)}{1 + 2m_O/m_C},$$
$$\dot{x}_O(0) = \dot{y}_O(0) = 0. \tag{D.6}$$

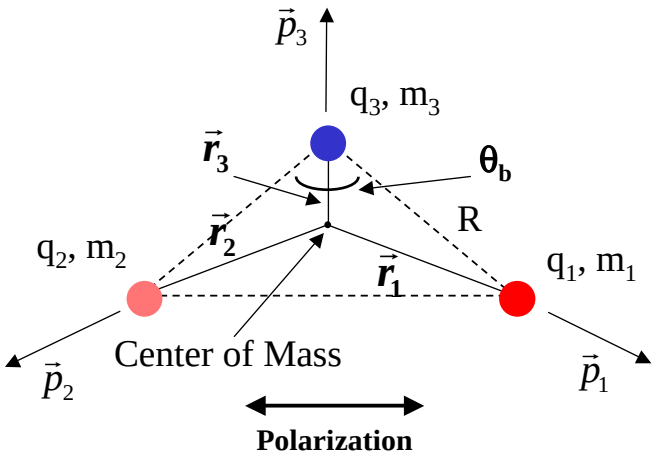

Figure D.1: Three-body Coulomb explosion. The center of mass of the system is located at the origin of the coordinate system. The x-axis is horizontal and parallel to the polarization axis. Without external force, the center of mass will not move. At $t = 0$, assuming symmetric geometry, $|\vec{r}_1 - \vec{r}_3| = |\vec{r}_1 - \vec{r}_3| = R$ is the bond length. The angle between $\vec{r}_1 - \vec{r}_3$ and $\vec{r}_2 - \vec{r}_3$ is the bond angle θ_b. The center-of-mass angle θ_{CM} is defined as the asymptotic value of the angle between $\vec{p}_1$ and $\vec{p}_2$ as $t \to \infty$.

Since there is no analytic solution, the differential equations were solved numerically with *Mathematica* (Wolfram Research, Inc.) between $t_0 = 0$ and a final time t_f. For the molecules in this study (CO_2 and NO_2), if $q = 2$ and $R = 0.1 - 0.3$ nm, $\dot{x}_O$ and $\dot{y}_O$ change less than 3% between $t = 200$ and 2000 fs. Thus the final time t_f is set at 2200 fs to ensure $\dot{x}_O(t_f)$ and $\dot{y}_O(t_f)$ approach their asymptotic values as $t \to \infty$. The center of mass angle θ_{CM} between $\vec{p}_1$ and $\vec{p}_2$ is evaluated as $\theta_{CM} = 2\tan^{-1}\frac{\dot{x}_O(t_f)}{\dot{y}_O(t_f)}$, which can be measured by *image labelling*.

For a given R and θ_b, there is a unique solution of final momentum $\vec{p}_O = m_O(\dot{x}_O(t_f)\hat{x} + \dot{y}_O(t_f)\hat{y})$ and θ_{CM}. The final momenta of all three charges can be written as

$$\vec{p}_1 = m_O(\dot{x}_O(t_f)\hat{x} + \dot{y}_O(t_f)\hat{y}),$$

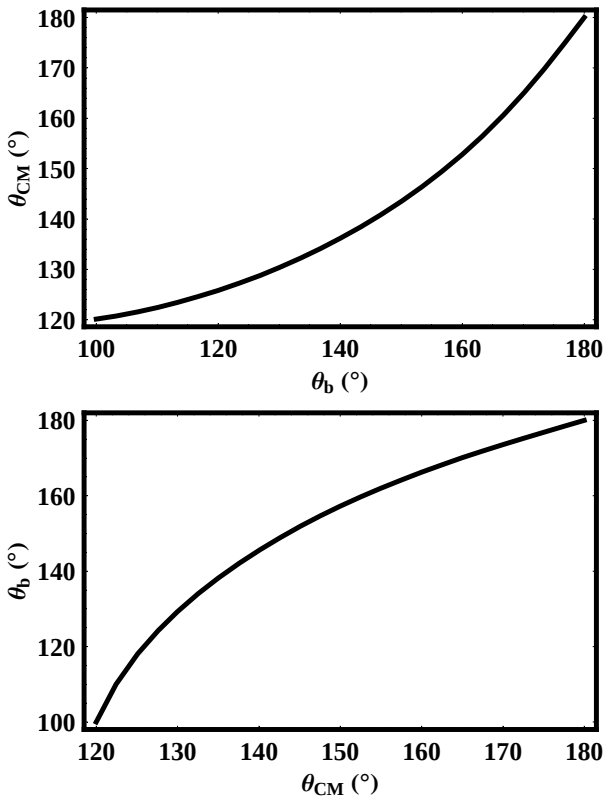

Figure D.2: Simulated functions $\theta_{CM}(\theta_b)$ and $\theta_b(\theta_{CM})$ for CO_2^{6+} symmetric explosions with $R = 0.22$ nm and $q_O = q_C = 2$, assuming pure Coulomb interaction.

$$\vec{p}_2 = m_O(-\dot{x}_O(t_f)\hat{x} + \dot{y}_O(t_f)\hat{y}), \tag{D.7}$$

$$\vec{p}_3 = m_C\dot{y}_C(t_f)\hat{y} = -2m_O\dot{y}_O(t_f)\hat{y}.$$

If R and θ_{CM} are given, θ_b can be found by solving the equation $\theta_{CM} = f(R, \theta_b)$ numerically, where f is not analytical in most cases. As the bisection root-finding method [146] is implemented, the solution converges to a relative error smaller than 1×10^{-6} within 30 iterations. The functions $\theta_{CM}(\theta_b)$ and $\theta_b(\theta_{CM})$ are plotted in Fig. D.2 for CO_2^{6+} explosions assuming $R = 0.22$ nm. The functions $\theta_{CM}(\theta_b)$ are plotted in Fig. D.3 for symmetric explosions of four 6-fold charged triatomic molecular ions (XY_2^{6+}) as well as H_2O^{3+} with $R = 0.22$ nm.

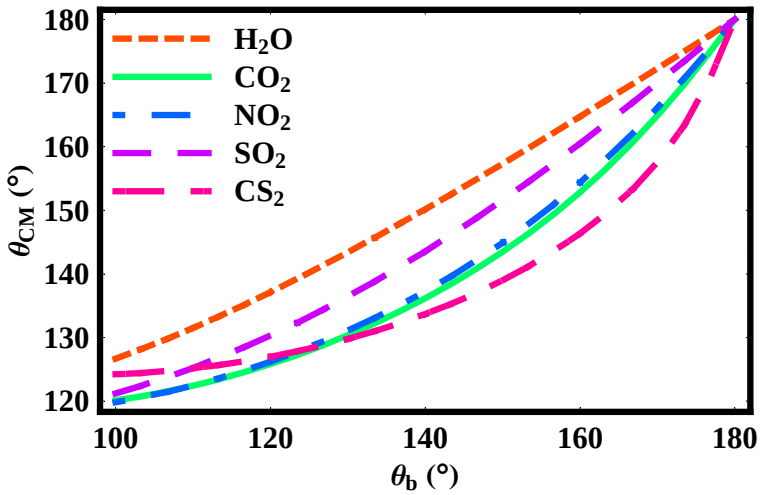

Figure D.3: Simulated functions $\theta_{CM}(\theta_b)$ for symmetric explosions of four 6-fold charged triatomic molecular ions (XY_2^{6+}) with $R = 0.22$ nm and $q_O = q_C = 2$, as well as H_2O^{3+} with $q_O = q_C = 1$, assuming pure Coulomb interaction.

Therefore, the initial molecular structure (R and θ_b) can be evaluated from the final momenta (p_O, p_C) and θ_{CM} measured by *image labelling* with energy conservation,

$$\begin{aligned} \mathcal{E}_C &= \sum_{i>j}^{3} \frac{K q_i q_j e^2}{r_{ij}} = \frac{2K q_C q_O e^2}{R} + \frac{K q_O^2 e^2}{2R\sin(\theta_b/2)}, \\ \mathcal{E}_k &= \frac{1}{2}\sum_{i=1}^{3} \frac{p_i^2}{m_i} = \frac{p_O^2}{m_O} + \frac{p_C^2}{2m_C}, \\ \mathcal{E}_k &= \mathcal{E}_C. \end{aligned} \tag{D.8}$$

In the linear configuration where $\theta_b = \theta_{CM} = 180°$ and $p_C = 0$, Eq. D.8 becomes

$$2K q_C q_O e^2/R + K q_O^2 e^2/(2R) = p_O^2/m_O, \tag{D.9}$$

so the bond length for the linear configuration is

$$R^{lin} = K q_O (4q_C + q_O) e^2 m_O/(2p_O^2). \tag{D.10}$$

Assuming the same R^{lin} for $\theta_{CM} \neq 180$, θ_b can be determined by the bisection

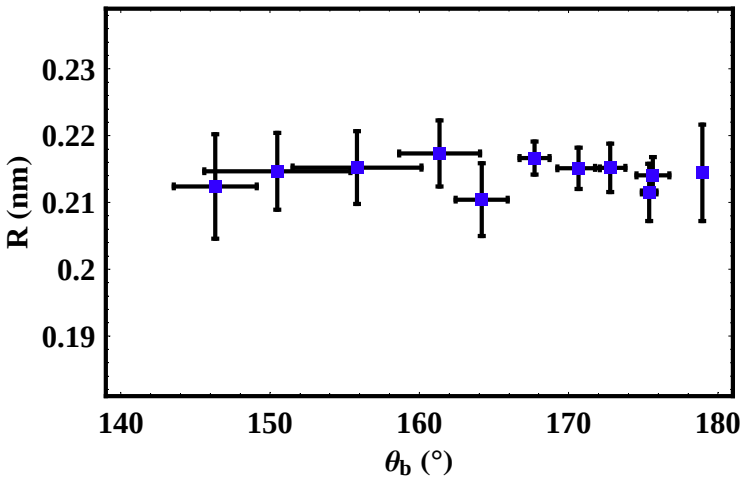

Figure D.4: Bond lengths and bond angles where CO_2^{6+} symmetric explosions initiate with $q_O = q_C = 2$ measured by *image labelling* (Sec. 4.2) at laser intensity of 2×10^{15} W/cm^2. Bond angles θ_b are determined from measured θ_{CM} using Fig. D.2. The error bars are the standard deviation of four experiments under the same conditions.

method, and R for this θ_b can be determined by Eq. D.8. Figure D.4 shows the result of CO_2^{6+} explosions induced by linearly polarized field at 2×10^{15} W/cm^2.

Although the bond lengths plotted in Fig. D.4 are approximately constant for different bond angles, this may not be true in general. The bond length in a bent configuration (θ_b and $\theta_{CM} < 180°$) may not be the same as R^{lin}. On the other hand, θ_b determined from θ_{CM} may also depend on R. As shown in Fig. D.5, θ_b as a function of R, for fixed θ_{CM}, monotonically decreases as R increases from 0.1 to 0.3 nm.

Therefore, the variation $\Delta\theta_b \equiv \theta_b(R = 0.1, \theta_{CM}) - \theta_b(R = 0.3, \theta_{CM})$ can be used as a measure of how accurate θ_b can be determined from θ_{CM} assuming $R = R^{lin}$. Figure D.6 shows that the variation $\Delta\theta_b$ is less than 0.08° or 0.05% for $CO_2^{6+} \rightarrow O^{2+} + C^{2+} + O^{2+}$ explosions with θ_{CM} between 120° and 180°. For the other

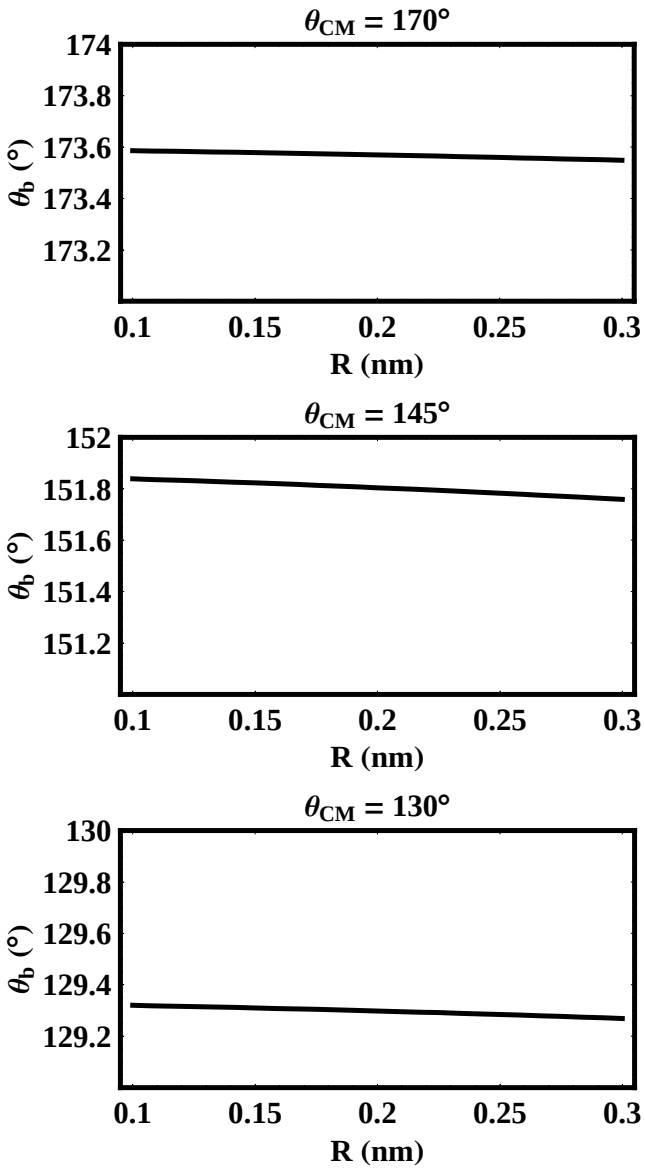

Figure D.5: Calculated bond angle as a function of bond length as θ_{CM} is fixed at 170°, 145° and 130°. The calculation is carried out with CO_2^{6+} symmetric explosions and $q_O = q_C = 2$.

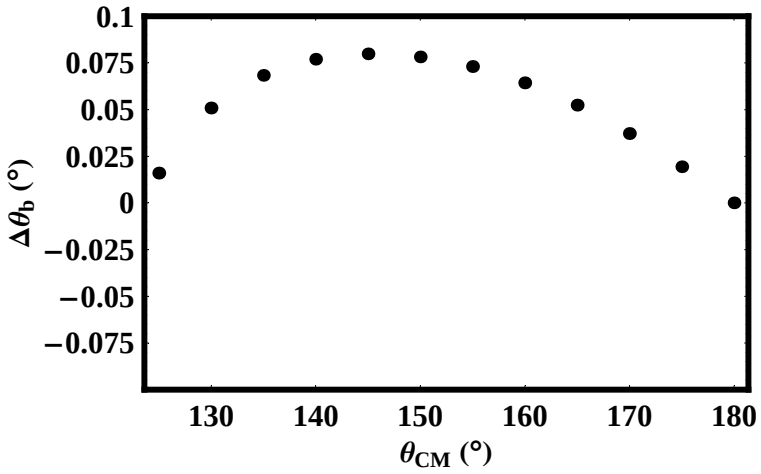

Figure D.6: Calculated variation $\Delta\theta_b \equiv \theta_b(R = 0.1, \theta_{CM}) - \theta_b(R = 0.3, \theta_{CM})$ as a function of θ_{CM} for $CO_2^{6+} \rightarrow O^{2+} + C^{2+} + O^{2+}$ explosion with θ_{CM} between 125° and 180°. The maximum $\Delta\theta_b$, 0.08° or 0.05%, appears near $\theta_{CM} = 145°$.

3-body Coulomb explosion discussed in this study, $NO_2^{6+} \rightarrow O^{2+} + N^{2+} + O^{2+}$, the upper limit of $\Delta\theta_b$ is about the same (0.08° or 0.055%). Thus, the functions $\theta_b(\theta_{CM})$ and $\theta_{CM}(\theta_b)$ can be considered independent of R. Consequently, θ_b can be determined from θ_{CM} assuming any R between 0.1 and 0.3 nm.

In summary, the motion of the three ejected ions from a symmetric 3-body Coulomb explosion is determined numerically. The relationship between the final center-of-mass angle and initial bond angle is found to be independent on the bond length. After the bond angle is determined from the center-of-mass angle assuming any bond length between 0.1 and 0.3 nm, the bond length can be calculated using Eq. D.8. Therefore, the bond length and bond angle where the Coulomb explosion takes place can be fully determined from the measured momenta and center-of-mass angle of the ejected ions.

Appendix E

Two Simulations for Electron Screening

Two simple simulations were performed to check how the initial time (t_1), when the electrons are freed by the laser field in molecular dissociative-ionization, would affect the final kinetic energy of the Coulomb explosion assuming the electron screening effect (Secs. 2.1.2 and 5.1.2). The first one was to simulate the electron distribution as a function of t_1. The second was to simulate the explosion energy as a function of t_1 with a quasi-dynamic screening calculation. Both simulations showed certain degree of instability of the dynamics – the results were sensitive to the initial time.

In the electron distribution simulation, one electron was assumed to follow the oscillation of the laser field since it was born at t_1. The laser pulse was assumed as a single-frequency sech^2 pulse whose electric field and intensity were given by

$$\begin{aligned} E(t) &= E_0 \cos(\omega t)\mathrm{sech}(t/\tau), \\ I(t) &= I_0 \cos^2(\omega t)\mathrm{sech}^2(t/\tau), \end{aligned} \tag{E.1}$$

where $\omega = 2.35\times10^{15}$Hz, which corresponds to $\lambda = 800$ nm, $\tau = 50$ fs with which the corresponding intensity pulse envelop has a width of about 90 fs, and $E_0 = 8.7\times10^8$ V/cm so that $I_0 = 10^{15}$ W/cm^2. Thus, following the radius of vibration of a free electron in the laser field (Eq. 5.13) [109, 134], the position of the electron as a

function of time can be expressed as

$$\begin{aligned} x_e(t) &= \frac{eE(t)}{m_e\omega^2}, \\ &= \frac{eE_0}{m_e\omega^2}\cos(\omega t)\mathrm{sech}(t/\tau), \end{aligned} \tag{E.2}$$

where e is the elementary charge, and m_e is the mass of electron.

Since the maximum field was $E_0 = 8.7 \times 10^8$ V/cm ($I_0 = 10^{15}$ W/cm^2), the maximum radius of electron was 2.7 nm. The probability or distribution of the electron in the space was therefore presented by the histogram of the appearance frequency of the electron at a position (x) between ± 2.7 nm as the electron was driven by the laser field according to Eq. E.2 between the initial time t_1 when the electron was removed from the molecule and a final time t_2 relative to the peak of the pulse. For a fixed $t_2 = 180$ fs at the end of the pulse, as t_1 varied from -130 to -70 fs, a double-peak structure stayed fixed near the center of the plot (Fig. E.1), which corresponded to the low intensity part of the pulse at the falling edge (as the time approached t_2). However, the distribution on both sides of the double-peak moved toward larger radii ($\pm x$) as t_1 moved closer to the peak of the pulse (Fig. E.1). The variation of the electron distribution became more significant as a fixed $\Delta t = t_2 - t_1$ was used instead of a fixed t_2 (Fig. E.2). Both width and height of the double-peak structure varied non-monotonically, which was related to the laser intensity variation between t_1 and t_2. These results showed that the calculated electron distribution depended on and was sensitive to the initial time when the electron was removed by the laser field, as well as the time interval and the laser intensity during that time when the electron was oscillating near the molecular ion.

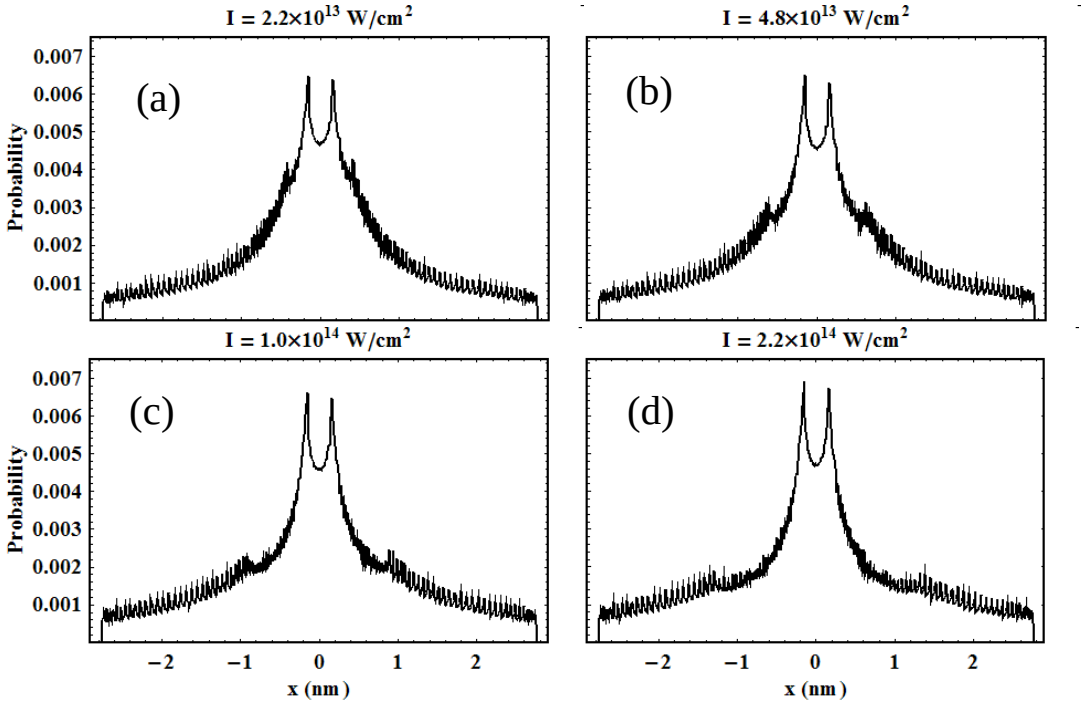

Figure E.1: Calculated histogram of the appearance frequency of the electron at a position (x) between ± 2.7 nm as the electron is driven by the laser field according to Eq. E.2 between t_1 and t_2. The initial time t_1 relative to the peak of the pulse and the intensity at t_1 are (a) -130 fs and 2.2×10^{13} W/cm^2; (b) -110 fs and 4.8×10^{13} W/cm^2; (c) -90 fs and 1.0×10^{14} W/cm^2; and (d) -70 fs and 2.2×10^{14} W/cm^2. The final time $t_2 = 180$ fs, which is roughly the end of the pulse. The total probability in each plot is normalized to unity.

If this electron distribution is assumed to be the source of the screening effect in the electron screening model of the molecular dissociative ionization, the dynamics described by the model will also be sensitive to the initial time.

In the quasi-dynamic screening calculation, two electron wave packets represented by two 2D Gaussian density functions located at $\pm x_e$ were moving according to the radius of vibration of a free electron in the laser field (Eq. E.3),

$$x_e(t) = \frac{eE(t)}{m_e \omega^2}, \tag{E.3}$$

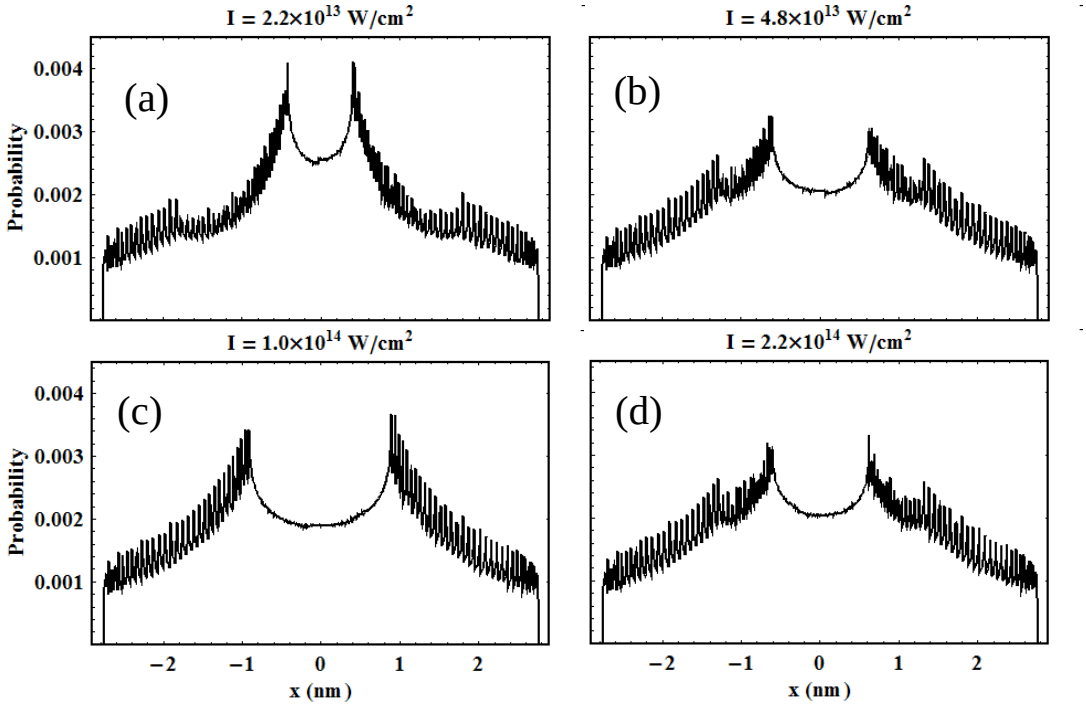

Figure E.2: Calculated histogram of the appearance frequency of the electron at a position (x) between ± 2.7 nm as the electron is driven by the laser field according to Eq. E.2 between t_1 and t_2. The initial time t_1 relative to the peak of the pulse and the intensity at t_1 are (a) -130 fs and 2.2×10^{13} W/cm^2; (b) -110 fs and 4.8×10^{13} W/cm^2; (c) -90 fs and 1.0×10^{14} W/cm^2; and (d) -70 fs and 2.2×10^{14} W/cm^2. The final time $t_2 = t_1 + 180$ fs. The total probability in each plot is normalized to unity.

where $E(t) = E_0 \cdot \mathrm{sech}(t/\tau)$ was the time-dependent electric field envelop of the laser pulse (peaking at $t = 0$) with $\tau = 50$ fs and the corresponding intensity pulse envelop $I(t) = I_0 \cdot \mathrm{sech}^2(t/\tau)$ had a width of about 90 fs. Then, the electron distribution, which was time-dependent through x_e, was given by

$$\rho(x, y) = \rho_0 \left[e^{-(x-x_e)^2/x_0^2} + e^{-(x+x_e)^2/x_0^2} \right] e^{-y^2/y_0^2}, \tag{E.4}$$

where $\rho_0 = Q_{el}/(2\pi x_0 y_0)$ was determined by $Q_{el} = \int \rho(x, y) \mathrm{d}x\mathrm{d}y$, the total number of electrons in the density distribution.

Three positive charges were released at $t = t_1$ from their initial positions separated by the equilibrium bond length (R_e) for the ground-state molecule, $q_1(R_e, 0)$, $q_2(-R_e, 0)$, and $q_3(0, 0)$ where the linear configuration and symmetric charge distribution ($q_1 = q_2 = q_3 = q = 2$) were considered. The charges begin to move under the Coulomb repulsion between them and the Coulomb force from the electron distribution. As both molecules in this study (CO_2 and NO_2) are symmetric in mass ($m_1 = m_2 = m_O$), the motion of the charges would also be symmetric, $x_1 = -x_2$, $y_1 = y_2 = 0$, and $x_3 = y_3 = 0$. Thus, the equations of motion reduced to

$$\begin{aligned} m_1\ddot{x}_1 &= \frac{Kq^2e^2}{4x_1^2} + \frac{Kq^2e^2}{x_1^2} \\ &\quad - \int \frac{Kqe^2\rho(x,y)(x_1 - x)\mathrm{d}x\mathrm{d}y}{[(x_1 - x)^2 + y^2 + s^2]^{3/2}}, \end{aligned} \tag{E.5}$$

where s is the smoothing parameter to remove the singularity of the Coulomb potential. The first two terms are the Coulomb repulsion from the other two charges, and the third term is the force from the electron distribution – the screening effect.

The propagation of Eq. E.5 was carried out on discrete time intervals, $t = t_1$, t_2, $t_3 \cdots$, where the step size $\Delta t = t_{i+1} - t_i = 0.5$ fs was fixed. The initial conditions at $t = t_1$ are

$$x_1(t_1) = R_e, \qquad \dot{x_1}(t_1) = 0, \qquad \ddot{x_1}(t_1) = 0. \tag{E.6}$$

At each step ($t = t_i$), the acceleration $\ddot{x_1}(t_i)$ was calculated from $x_1(t_{i-1})$ and $\rho(x, y)$ with $x_e(t_i)$ by Eq. E.5. Then, the velocity and position,

$$\begin{aligned} \dot{x_1}(t_i) &= \dot{x_1}(t_{i-1}) + \ddot{x_1}(t_i) \cdot \Delta t, \\ x_1(t_i) &= x_1(t_{i-1}) + \dot{x_1}(t_i) \cdot \Delta t, \end{aligned} \tag{E.7}$$

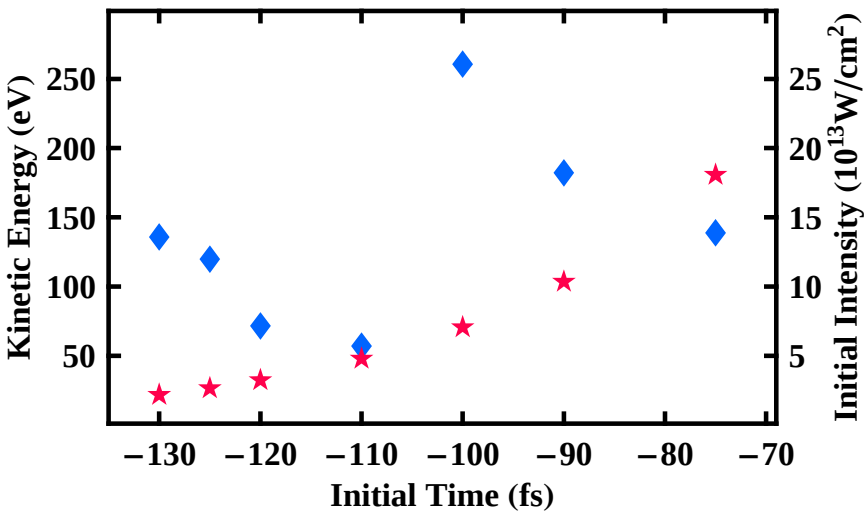

Figure E.3: Calculated final kinetic energy (Blue diamonds, left axis) by the quasi-dynamic simulation as a function of the initial time t_1 when the electrons are born, and the laser intensity (Red stars, right axis) at these times. The initial time is relative to the peak of the pulse.

can be determined. At the end of the calculation, normally 800 steps and roughly 300 fs after the peak of the laser pulse at $t = 0$, the kinetic energy of the oxygen ion (q_1) was given by

$$\mathcal{E}_{k1} = m_1 \dot{x_1}^2(t_f)/2, \tag{E.8}$$

where $f = 800$. Since the central ion would gain no momentum in a linear and symmetric configuration, the total kinetic energy release of this electron-screened Coulomb explosion was

$$\mathcal{E}_k = 2\mathcal{E}_{k1} = m_1 \dot{x_1}^2(t_f). \tag{E.9}$$

As t_1 was being varied, kinetic energy release $\mathcal{E}_k$ as a function of t_1 can be plotted.

The values of the parameters were chosen as the following: $x_0 = 0.28$ nm so that the two Gaussian functions would barely overlap at the origin; $y_0 = 0.021$ nm and $s = 0.026$ nm to roughly match with the values in the static screening model

(Sec. 5.1.2); $Q_{el} = 4$ so that the minimum on the curve of $\mathcal{E}_k$ vs t_1 was about 60 eV, which was roughly the same as the observation in the experiments; $R_e = 0.119$ nm for NO_2, and the peak intensity was $I_0 = 10^{15}$ W/cm^2. As t_1 moved from 130 to 75 fs earlier than the peak of the laser pulse and the laser intensity at t_1 changed from 2.2×10^{13} to 1.8×10^{14} W/cm^2, the final kinetic energy varied by a factor of 4 between roughly 60 and 260 eV and the curve was not monotonic, as shown in Fig. E.3. The result showed that, in this simple quasi-dynamic screening calculation, the final kinetic energy was sensitive to the initial time when the electrons were born and trapped near the nuclei by the laser field, and the variation of the kinetic energy was not a monotonic function of the initial time.

BIBLIOGRAPHY

[1] R. S. Judson and H. Rabitz, "Teaching Lasers to Control Molecules," Phys. Rev. Lett. **68**, 1500 (1992).

[2] L. Zhu, V. Kleiman, X. Li, S. P. Lu, K. Trentelman, and R. J. Gordon, "Coherent Laser Control of the Product Distribution Obtained in the Photoexcitation of HI," Science **270**, 77 (1995).

[3] A. Assion, T. Baumert, M. Bergt, T. Brixner, B. Kiefer, V. Seyfried, M. Strehle, and G. Gerber, "Control of Chemical Reactions by Feedback-Optimized Phase-Shaped Femtosecond Laser Pulses," Science **282**, 919 (1998).

[4] H. Rabitz, R. de Vivie-Riedle, M. Motzkus, and K. Kompa, "Whither the Future of Controlling Quantum Phenomena?" Science **288**, 824 (2000).

[5] R. J. Levis, G. M. Menkir, and H. Rabitz, "Selective Bond Dissociation and Rearrangement with Optimally Tailored, Strong-Field Laser Pulses," Science **292**, 709 (2001).

[6] B. J. Pearson, J. L. White, T. C. Weinacht, and P. H. Bucksbaum, "Coherent control using adaptive learning algorithms," Phys. Rev. A **63**, 063412 (2001).

[7] C. M. Dion, A. Ben Haj-Yedder, E. Cancès, C. Le Bris, A. Keller, and O. Atabek, "Optimal laser control of orientation: The kicked molecule," Phys. Rev. A **65**, 063408 (2002).

[8] I. R. Sola, "Laser-assisted molecular engineering of bond lengths and vibrational motion," Phys. Rev. A **69**, 033401 (2004).

[9] I. Plesser, Z. Vager, and R. Naaman, "Structure of C_3 as Measured by the Coulomb-Explosion Technique," Phys. Rev. Lett. **56**, 1559 (1986).

[10] Z. Vager, R. Naaman, and E. P. Kanter, "Coulomb Explosion Imaging of Small Molecules," Science **244**, 426 (1989).

[11] D. Kella, M. Algranati, H. Feldman, O. Heber, H. Kovner, E. Malkin, E. Miklazky, R. Naaman, D. Zajfman, and Z. Vager, "A system for Coulomb explosion imaging of small molecules at the Weizmann Institute," Nucl. Instrum. Methods **A329**, 440 (1993).

[12] A. E. Siegman, *Lasers* (University Science Books, Sausalito, California 1986).

[13] L. J. Frasinski, K. Codling, P. Hatherly, J. Barr, I. N. Ross, and W. T. Toner, "Femtosecond Dynamics of Multielectron Dissociative Ionization by Use of Picosecond Laser," Phys. Rev. Lett. **58**, 2424 (1987).

[14] K. Codling, L. J. Frasinski, P. Hatherly, and J. R. M. Barr, "On the major mode of multiphoton multiple ionisation," J. Phys. B **20**, L525 (1987).

[15] K. Codling, L. J. Frasinski, and P. A. Hatherly, "Multiphoton ionisation of H_2 and D_2 using an intense sub-picosecond laser," J. Phys. B **21**, 783 (1988).

[16] P. H. Bucksbaum, A. Zavriyev, H. G. Muller, and D. W. Schumacher, "Softening of the H_2^+ Molecular Bond in Intense Laser Fields," Phys. Rev. Lett. **64**, 1883 (1990).

[17] A. Zavriyev, P. H. Bucksbaum, H. G. Muller, and D. W. Schumacher, "Ionization and dissociation of H_2 in intense laser fields at 1.064 μm, 532 nm, and 355 nm," Phys. Rev. A **42**, 5500 (1990).

[18] L. J. Frasinski, M. Stankiewicz, P. A. Hatherly, G. M. Cross, K. Codling, A. J. Langley, and W. Shaikh, "Molecular H_2 in intense laser fields probed by electron-electron, electron-ion, and ion-ion covariance techniques," Phys. Rev. A **46**, R6789 (1992).

[19] H. Rottke, J. Ludwig, and W. Sandner, "H_2 and D_2 in intense sub-picosecond laser pulse: Photoelectron spectroscopy at 1053 and 527 nm," Phys. Rev. A **54**, 2224 (1996).

[20] G. N. Gibson, M. Li, C. Guo, and J. Neira, "Strong-Field Dissociation and Ionization of H_2^+ Using Ultrashort Laser Pulses," Phys. Rev. Lett. **79**, 2022 (1997).

[21] M. R. Thompson, M. K. Thomas, P. F. Taday, J. H. Posthumus, A. J. Langley, L. J. Frasinski, and K. Codling, "One and two-colour studies of the dissociative ionization and Coulomb explosion of H_2 with intense Ti:sapphire laser pulses," J. Phys. B **30**, 5755 (1997).

[22] J. Zhu and W. T. Hill, III, "Momentum and correlation spectra following intense-field dissociative ionization of H_2," J. Opt. Soc. Am. B **14**, 2212 (1997).

[23] A. Staudte, C. L. Cocke, M. H. Prior, A. Belkacem, C. Ray, H. W. Chong, T. E. Glover, R. W. Schoenlein, and U. Saalmann, "Observation of a nearly isotropic, high-energy Coulomb explosion group in the fragmentation of D_2 by short laser pulses," Phys. Rev. A **65**, 020703 (2002).

[24] K. Boyer, T. S. Luk, J. C. Solem, and C. K. Rhodes, "Kinetic energy distribution of ionic fragments produced by subpicosecond multiphoton ionization of N_2," Phys. Rev. A **39**, 1186 (1989).

[25] L. J. Frasinski, K. Codling, and P. A. Hatherly, "Multiphoton multiple ionisation of N_2 probed by covariance mapping," Phys. Lett. A **142**, 499 (1989).

[26] C. Cornaggia, J. Lavancier, D. Normand, J. Morellec, and H. X. Liu, "Intensity dependence of the multielectron dissociative ionization of N_2 at 305 and 610 nm," Phys. Rev. A **42**, 5464 (1990).

[27] K. Codling, C. Cornaggia, L. J. Frasinski, P. A. Hatherly, J. Morellec, and D. Normand, "Charge-symmetric fragmentation of diatomic molecules in intense picosecond laser fields," J. Phys. B **24**, L593 (1991).

[28] C. Cornaggia, J. Lavancier, D. Normand, J. Morellec, P. Agostini, J. P. Chambaret, and A. Antonetti, "Multielectron Dissociative Ionization of Diatomic Molecules in an Intense Femtosecond Laser Field," Phys. Rev. A **44**, 4499 (1991).

[29] C. Cornaggia, D. Normand, and J. Morellec, "Role of the molecular electronic configuration in the Coulomb fragmentation of N_2, C_2H_2 and C_2H_4 in an intense laser field," J. Phys. B **25**, L415 (1992).

[30] W. T. Hill, III, J. Zhu, D. L. Hatten, Y. Cui, J. Goldhar, and S. Yang, "Role of Non-Coulombic Potential Curves in Intense-Field Dissociative Ionization of Diatomic Molecules," Phys. Rev. Lett. **69**, 2646 (1992).

[31] M. Stankiewicz, L. J. Fransinski, G. M. Cross, P. A. Hatherly, K. Codling, A. J. Langley, and W. Shaikh, "Dissociative ionization of N_2 and CO using intense lasers at 248 and 305 nm," J. Phys. B **26**, 2619 (1993).

[32] Ph. Hering and C. Cornaggia, "Production of multicharged atomic ions from laser-induced multiple ionization of small molecules," Phys. Rev. A **57**, 4572 (1998).

[33] A. Hishikawa, A. Iwamae, K. Hoshina, M. Kono, and K. Yamanouchi, "Mass-resolved two-dimensional momentum imaging of the Coulomb explosion of N_2 and SO_2 in an intense laser field," Chem. Phys. Lett. **282**, 283 (1998).

[34] A. Hishikawa, A. Iwamae, K. Hoshina, M. Kono, and K. Yamanouchi, "Coulomb explosion dynamics of N_2 in intense laser field by mass-resolved momentum imaging," Chem. Phys. **231**, 315 (1998).

[35] S. Banerjee, G. Ravindra Kumar, and D. Mathur, "Multiple ionization of N_2 in intense, linearly and circularly polarized light fields," Phys. Rev. A **60**, R25 (1999).

[36] Ph. Hering and C. Cornaggia, "Coulomb explosion of N_2 and CO_2 using linearly and circularly polarized femtosecond laser pulses," Phys. Rev. A **59**, 2836 (1999).

[37] M. Schmidt, S. Dobosz, P. Meynadier, P. D'Oliveira, D. Normand, E. Charron, and A. Suzor-Weiner, "Fragment-emission patterns from the Coulomb explosion of diatomic molecules in intense laser fields," Phys. Rev. A **60**, 4706 (1999).

[38] J. P. Nibarger, S. V. Menon, and G. N. Gibson, "Comprehensive analysis of strong-field ionization and dissociation of diatomic nitrogen," Phys. Rev. A **63**, 053406 (2001).

[39] K. Miyazaki, T. Shimizu, and D. Normand, "Femtosecond-laser-induced alignment in Coulomb explosion of N_2," J. Phys. B **37**, 753 (2004).

[40] D. Normand, C. Cornaggia, J. Lavancier, J. Morellec, and H. X. Liu, "Multielectron dissociative ionization of O_2 in an intense picosecond laser field," Phys. Rev. A **44**, 475 (1991).

[41] Ch. Ellert, H. Stapelfeldt, E. Constant, H. Sakai, J. Wright, D. M. Rayner, and P. B. Corkum, "Observing molecular dynamics with timed Coulomb explosion imaging," Philos. Trans. R. Soc. London, Ser. A **356**, 329 (1998).

[42] Ch. Ellert and P. B. Corkum, "Disentangling molecular alignment and enhanced ionization in intense laser fields," Phys. Rev. A **59**, R3170 (1999).

[43] P. A. Hatherly, L. J. Fransinski, K. Codling, A. J. Langley, and W. Shaikh, "The angular distribution of atomic ions following the multiphoton ionisation of carbon monoxide," J. Phys. B **23**, L291 (1990).

[44] J. Lavancier, D. Normand, C. Cornaggia, J. Morellec, and H. X. Liu, "Laser-intensity dependence of the multielectron ionization of CO at 305 and 610 nm," Phys. Rev. A **43**, 1461 (1991).

[45] D. Normand, L. A. Lompré, and C. Cornaggia, "Laser-induced molecular alignment probed by a double-pulse experiment," J. Phys. B **25**, L497 (1992).

[46] A. Talebpour, S. Larochelle, and S. L. Chin, "Dissociative ionization of NO in an intense laser field: a route towards enhanced ionization," J. Phys. B **30**, 1927 (1997).

[47] A. Iwamae, A. Hishikawa, and K. Yamanouchi, "Extraction of molecular dynamics in intense laser fields from mass-resolved momentum imaging maps: application to Coulomb explosion of NO," J. Phys. B **33**, 223 (2000).

[48] M. Schmidt, D. Normand, and C. Cornaggia, "Laser-induced trapping of chlorine molecules with pico- and femtosecond pulses," Phys. Rev. A **50**, 5037 (1994).

[49] D. T. Strickland, Y. Beaudoin, P. Dietrich, and P. B. Corkum, "Optical Studies of Inertially Confined Molecular Iodine Ions," Phys. Rev. Lett. **68**, 2755 (1992).

[50] P. Dietrich, D. T. Strickland, and P. B. Corkum, "Multiphoton ionization of inertially confined molecular ions," J. Phys. B **26**, 2323 (1993).

[51] P. A. Hatherly, M. Stankiewicz, K. Codling, L. J. Frasinski, and G. M. Cross, "The multielectron dissociative ionization of molecular iodine in intense laser fields," J. Phys. B **27**, 2993 (1994).

[52] E. Constant, H. Stapelfeldt, and P. B. Corkum, "Observation of Enhanced Ionization of Molecular Ions in Intense Laser Fields," Phys. Rev. Lett. **76**, 4140 (1996).

[53] J. H. Posthumus, A. J. Giles, M. R. Thompson, W. Shaikh, A. J. Langley, L. J. Frasinski, and K. Codling, "The dissociation dynamics of diatomic molecules in intense laser fields," J. Phys. B **29**, L525 (1996).

[54] F. Rosca-Pruna, E. Springate, H.L. Offerhaus, M. Krishnamurthy, N. Farid, C. Nicole, and M.J.J. Vrakking, "Spatial alignment of diatomic molecules in intense laser fields: I. Experimental results," J. Phys. B **34**, 4919 (2001).

[55] E. Springate, F. Rosca-Pruna, H.L. Offerhaus, M. Krishnamurthy, and M.J.J. Vrakking, "Spatial alignment of diatomic molecules in intense laser fields: II. Numerical modelling," J. Phys. B **34**, 4939 (2001).

[56] C. Cornaggia, M. Schmidt, and D. Normand, "Coulomb explosion of CO_2 in an intense femtosecond laser field," J. Phys. B **27**, L123 (1994).

[57] L. J. Frasinski, P. A. Hatherly, K. Codling, M. Larsson, A. Persson, and C-G Wahlstrom, "Multielectron dissociative ionization of CO_2 in intense laser fields," J. Phys. B **27**, L109 (1994).

[58] C. Cornaggia, "Large-amplitude nuclear motions in the laser-induced Coulomb explosion of carbon dioxide molecules," Phys. Rev. A **54**, R2555 (1996).

[59] J. H. Sanderson, R. V. Thomas, W. A. Bryan, W. R. Newell, A. J. Langley, and P. F. Taday, "Alignment and bending of CO_2 by intense femtosecond laser pulses," J. Phys. B **31**, L599 (1998).

[60] A. Hishikawa, A. Iwamae, and K. Yamanouchi, "Ultrafast deformation of the geometrical structure of CO_2 induced in intense laser fields," Phys. Rev. Lett. **83**, 1127 (1999).

[61] W. A. Bryan, J. H. Sanderson, A. El-Zein, W. R. Newell, P.F. Taday, and A. J. Langley, "Laser-induced Coulomb explosion, geometry modification and reorientation of carbon dioxide," J. Phys. B **33**, 745 (2000).

[62] K. Zhao, G. Zhang, and W. T. Hill, III, "Strong-field dissociative-ionization of a linear triatomic molecule: Relationship between Coulomb-explosion energies and bond angle," Phys. Rev. A **68**, 063408 (2003).

[63] K. Zhao and W. T. Hill, III, "Ejection anisotropy in 3-atom Coulomb explosions," Phys. Rev. A **71**, 013412 (2005).

[64] L. J. Frasinski, P. A. Hatherly, and K. Codling, "Multiphoton multiple ionisation of N_2O probed by three-dimensional covariance mapping," Phys. Lett. A **142**, 499 (1991).

[65] H. Hasegawa, A. Hishikawa, and K. Yamanouchi, "Coincidence imaging of Coulomb explosion of CS_2 in intense laser fields," Chem. Phys. Lett. **349**, 57 (2001).

[66] J. H. Sanderson, T. R. J. Goodworth, A. El-Zein, W. A. Bryan, W. R. Newell, A. J. Langley, and P.F. Taday, "Coulombic and pre-Coulombic geometry evolution of carbonyl sulfide in an intense femtosecond laser pulse," Phys. Rev. A **65**, 043403 (2002).

[67] J. H. Sanderson, A. El-Zein, W. A. Bryan, W. R. Newell, A. J. Langley, and P.F. Taday, "Geometry modifications and alignment of H_2O in an intense femtosecond laser pulse," Phys. Rev. A **59**, R2567 (1999).

[68] A. Hishikawa, A. Iwamae, and K. Yamanouchi, "Ultrafast structural deformation of NO_2 in intense laser fields studied by mass-resolved momentum imaging," J. Chem. Phys. **111**, 8871 (1999).

[69] C. Cornaggia, F. Salin, and C. Le Blanc, "Changes in the SO_2 geometry during the laser-induced multiple ionization and Fragmentation," J. Phys. B **29**, 749 (1996).

[70] J. H. Posthumus, L. J. Frasinski, A. J. Giles, and K. Codling, "Dissociative ionization of molecules in intense laser fields: a method of predicting ion kinetic energies and appearance intensities," J. Phys. B **28**, L349 (1995).

[71] K. Codling, L. J. Frasinski, and P. A. Hatherly, "On the field ionisation of diatomic molecules by intense laser fields," J. Phys. B **22**, L321 (1989).

[72] K. Codling and L. J. Frasinski, "Dissociative ionization of small molecules in intense laser fields," J. Phys. B **26**, 783 (1993).

[73] S. Chelkowski and A. D. Bandrauk, "Two-step Coulomb explosions of diatoms in itense laser fields," J. Phys. B **28**, L723 (1995).

[74] T. Seideman, M. Yu. Ivanov, and P. B. Corkum, "The Role of Electron Localization in Intense-Field Molecular Ionization," Phys. Rev. Lett. **75**, 2819 (1995).

[75] T. Zuo and A. D. Bandrauk, "Charge-resonance-enhanced ionization of diatomic molecular ions by intense lasers," Phys. Rev. A **52**, R2511 (1995).

[76] M. Ivanov, T. Seideman, P. Corkum, F. Ilkov, and P. Dietrich, "Explosive ionization of molecules in intense laser fields," Phys. Rev. A **54**, 1541 (1996).

[77] J. H. Posthumus, A. J. Giles, M. R. Thompson, and K. Codling, "Field ionization, Coulomb explosion of diatomic molecules in intense laser fields," J. Phys. B **29**, 5811 (1996).

[78] S. Chelkowski, C. Foisy, and A. D. Bandrauk, "Electron-nuclear dynamics of multiphoton H_2^+ dissociative ionization in intense laser fields," Phys. Rev. A **57**, 1176 (1998).

[79] M. Brewczyk, K. Rzążewski, and C. W. Clark, "Multielectron Dissociative Ionization of Molecules by Intense Laser Radiation," Phys. Rev. Lett. **78**, 191 (1997).

[80] M. Brewczyk and K. Rzążewski, "One-dimensional Thomas-Fermi model of atoms, molecules, and small clusters exposed to an intense laser field," Phys. Rev. A **60**, 2285 (1999).

[81] M. Brewczyk and K. Rzążewski, "Multielectron dissociative ionization of molecules by strong femtosecond pulses," Phys. Rev. A **61**, 023412 (2000).

[82] Ph. Hering, M. Brewczyk, and C. Cornaggia, "Hydrodynamic description of laser-induced Coulomb explosion for small molecules," Phys. Rev. Lett. **85**, 2288 (2000).

[83] H. Kono, S. Koseki, M. Shiota, and Y. Fujimura, "A Theoretical Study of Electronic Dynamics and Deformation of CO_2 in Intense Laser Fields," J. Phys. Chem. A **105**, 5627 (2001).

[84] Y. Sato, H. Kono, S. Koseki, and Y. Fujimura, "Description of Molecular Dynamics in Intense Laser Fields by the Time-Dependent Adiabatic State Approach: Application to Simultaneous Two-Bond Dissociation of CO_2 and Its Control," J. Am. Chem. Soc. **125**, 8019 (2003).

[85] H. Kono, Y. Sato, N. Tanaka, T. Kato, K. Nakai, S. Koseki, and Y. Fujimura, "Quantum mechanical study of electronic and nuclear dynamics of molecules in intense laser fields," Chem. Phys. **304**, 203 (2004).

[86] J. H. Posthumus, J. Plumridge, M. K. Thomas, K. Codling, L. J. Frasinski, A. J. Langley, and P. F. Taday, "Dynamic and geometric laser-induced alignment of molecules in intense laser fields," J. Phys. B **31**, L553 (1998).

[87] P. Dietrich, D. T. Strickland, M. Laberge, and P. B. Corkum, "Molecular reorientation during dissociative multiphoton ionization," Phys. Rev. A **47**, 2305 (1993).

[88] M. Brewczyk, M. Gajda, and K. Rzążewski, "Statistical Theory of Multielectron Ionization of Atoms and Molecules," Laser Phys. **3**, 343 (1993).

[89] P. Dietrich, M. Yu. Ivanov, F. A. Ilkov, and P. B. Corkum, "Two-Electron Dissociative Ionization of H_2 and D_2 in Infrared Laser Fields," Phys. Rev. Lett. **77**, 4150 (1996).

[90] H. Yu, T. Zuo, and A. D. Bandrauk, "Molecules in intense laser fields: Enhanced ionization in a one-dimensional model of H2," Phys. Rev. A **54**, 3290 (1996).

[91] I. Kawata, H. Kono, Y. Fujimura, and A.D. Bandrauk, "Intense-laser-field-enhanced ionization of two-electron molecules: Role of ionic states as doorway states," Phys. Rev. A **62**, 031401 (2000).

[92] T. Zuo and A.D. Bandrauk, "Phase control of molecular ionization: H_2^+ and H_3^{2+} in intense two-color laser fields," Phys. Rev. A **54**, 3254 (1996).

[93] H. Yu and A. D. Bandrauk, "Molecules in intense laser fields: Enhanced ionization in one- and two-electron linear triatomic molecules," Phys. Rev. A **56**, 685 (1997).

[94] H. Yu, T. Zuo, and A. D. Bandrauk, "Intense field ionization of molecules with ultra-short laser pulses – enhanced ionization and barrier-suppression effects," J. Phys. B **31**, 1533 (1998).

[95] I. Kawata, H. Kono, and A. D. Bandrauk, "Mechanism of enhanced ionization of linear H_3^+ in intense laser fields," Phys. Rev. A **64**, 043411 (2001).

[96] A. D. Bandrauk and J. Ruel, "Charge-resonance-enhanced ionization of molecular ions in intense laser pulses: Geometric and orientation effects," Phys. Rev. A **59**, 2153 (1999).

[97] S. Banerjee, D. Mathur, and G. R. Kumar, "Propensity of molecules to spatially align in intense light fields," Phys. Rev. A **63**, 045401 (2001).

[98] L. J. Frasinski, K. Codling, and P. A. Hatherly, "Covariance Mapping: A Correlation Method Applied to Multiphoton Multiple Ionization," Science **246**, 1029 (1989).

[99] K. Zhao, G. Zhang, and W. T. Hill, III, "Image Labeling: A graphical interface to correlation in multiparticle ejection dynamics," Opt. Express **9**, 42 (2001).

[100] K. Zhao, Colvin, Jr., T., W. T. Hill, III, and G. Zhang, "Deconvolving two-dimensional images of three-dimensional momentum trajectories," Rev. Sci. Instrum. **73**, 3044 (2002).

[101] J. Ullrich, R. Moshammer, R. Dörner, O. Jagutzki, V. Mergel, H. Schmidt-Böcking and L. Spielberger, "Recoil-ion momentum spectroscopy," J. Phys. B **30**, 2917 (1997).

[102] R. Dörner, V. Mergel, O. Jagutzki, L. Spielberger, J. Ullrich, R. Moshammer, and H. Schmidt-Böcking, "Cold Target Recoil Ion Momentum Spectroscopy: a 'momentum microscope' to view atomic collision dynamics," Phys. Rep. **330**, 95 (2000).

[103] W. T. Hill, III, K. Zhao, L. N. Elberson, and G. Menkir, "Strong-Field Correlation Imaging: Revealing Molecular Geometries, Orientation and Dynamics," in *Progress in Ultrafast Intense Laser Science*, edited by K. Yamanouchi (Springer, New York, in press), Vol. 1.

[104] L. V. Keldysh, "Ionization in the field of a strong electromagnetic wave," Zh. Eksp. Teor. Fiz. **47**, 1945 (1964) [Sov. Phys. JETP **20**, 1307 (1965)].

[105] F. Schwabl, *Quantum Mechanics* (Springer, New York 1995).

[106] S. Augst, D. Strickland, D. D. Meyerhofer, S. L. Chin, and J. H. Eberly, "Tunneling Ionization of Noble Gases in a High-Intensity Laser Field," Phys. Rev. Lett. **63**, 2212 (1989).

[107] R.S. Mulliken, "Intensities of Electronic Transitions in Molecular Spectra II. Charge-Transfer Spectra," J. Chem. Phys. **7**, 20 (1939).

[108] T. Zuo, S. Chelkowski, and A. D. Bandrauk, "Harmonic generation by the H_2^+ molecular ion in intense laser fields," Phys. Rev. A **48**, 3837 (1993).

[109] P. B. Corkum, "Plasma Perspective on Strong-Field Multiphoton Ionization," Phys. Rev. Lett. **71**, 1994 (1993).

[110] V. R. Bhardwaj, S. A. Aseyev, M. Mehendale, G. L. Yudin, D. M. Villeneuve, D. M. Rayner, M. Yu. Ivanov, and P. B. Corkum, "Few Cycle Dynamics of Multiphoton Double Ionization," Phys. Rev. Lett. **86**, 3522 (2001).

[111] M. Brewczyk, K. Rzążewski, and C.W. Clark, "Appearance intensities for multiply charged ions in a strong laser field," Phys. Rev. A **52**, 1468 (1995).

[112] B. Friedrich and D. Herschbach, "Alignment and Trapping of Molecules in Intense Laser Fields," Phys. Rev. Lett. **74**, 4623 (1995).

[113] B. Friedrich and D. Herschbach, "Polarization of Molecules Induced by Intense Nonresonant Laser Fields," J. Phys. Chem. **99**, 15686 (1995).

[114] NIST Standard Reference Database 101, "Computational Chemistry Comparison and Benchmark DataBase," Release 9 (2003), http://srdata.nist.gov/cccbdb/.

[115] G. Arfken, *Mathematical Methods for Physicists* (Academic Press, Orlando, Florida 1985), Chap. 5.8.

[116] *Tsunami User's Manual* (Spectra-Physics, Mountain View, California, 1995).

[117] *BeamLok 2060 User's Manual* (Spectra-Physics, Mountain View, California 1995).

[118] D. E. Spence, J. M. Evans, W E. Sleat, and W Sibbett, "Regeneratively initiated self-mode-locked Ti:sapphire laser," Opt. Lett. **16**, 1762 (1991).

[119] T. Brabec, Ch. Spielmann, P. F. Curley, and F Krausz, "Kerr lens mode locking," Opt. Lett. **17**, 1292 (1992).

[120] R. L. Fork, O. E. Martinez, and J. P. Gordon, "Negative dispersion using pairs of prisms," Opt. Lett. **9**, 150 (1984).

[121] See for example, Ch. Spielmann, P. F. Curley, T. Brabec, and F. Krausz, "Ultrabroadband Femtosecond Lasers," IEEE J. Quantum Electron. **30**, 1100 (1994), and reference therein.

[122] See for example, P. Maine, D. Strickland, P. Bado, M. Pessot, and G . Mourou, "Generation of Ultrahigh Peak Power Pulses by Chirped Pulse Amplification," IEEE J. Quantum Electron. **24**, 398 (1988).

[123] *Spitfire User's Manual* (Spectra-Physics, Mountain View, Califonia 1995).

[124] See for example, F. Salin, P. Georges, G. Roger, and A. Brun, "Single-shot measurement of a 52-fs pulse," Appl. Opt. **26**, 4528 (1987).

[125] *DALSA CA-D1 (RO1) Camera User's Manual* (DALSA Inc., Waterloo, Ontario, Canada 1999).

[126] The method of image compression was initially created and implemented by Mr. Brent Yorgey in Year 2000.

[127] C. J. Dasch, "One-dimensional tomography: a comparison of Abel, onion-peeling, and filtered back-projection methods," Appl. Opt. **31**, 1146 (1992).

[128] C. Bordas, F. Paulig, H. Helm, and D. L. Huestis, "Photoelectron imaging spectrometry: Principle and inversion method," Rev. Sci. Instrum. **67**, 2257 (1996).

[129] J. Winterhalter, D. Maier, J. Honerkamp, V. Schyja, and H. Helm, "Imaging of charged atomic reaction products: Inversion by a two-dimensional regularization method," J. Chem. Phys. **110**, 11187 (1999).

[130] M. J. J. Vrakking, "An iterative procedure for the inversion of two-dimensional ion/photoelectron imaging experiments," Rev. Sci. Instrum. **72**, 4084 (2001).

[131] G. Herzberg, *Molecular Spectra and Molecular Structure: II. Infrared and Ramon Spectra of Polyatomic Molecules* (Van Nostrand Reinhold Co., New York, NY, 1945).

[132] L. Burnelle, A. M. May, and R. A. Gangi, "Electronic Structure and Electronic Spectrum of Nitrogen Dioxide: Study by the Nonempirical Self-Consistent Field Method," J. Chem. Phys. **49**, 561 (1968).

[133] W. L. Wiese, J. R. Fuhr, and T. M. Deters, "Atomic Transition Probabilities of Carbon, Nitrogen, and Oxygen: A Critical Data Compilation," J. Phys. Chem. Ref. Data, Monograph 7, (1996).

[134] F. H. M. Faisal, *Theory of Multiphoton Processes* (Kluwer Academic Publishers, New York, New York 1987), Chap. 1.

[135] M. Protopapas, D. G. Lappas, and P. L. Knight, "Strong Field Ionization in Arbitrary Laser Polarizations," Phys. Rev. Lett. **79**, 4550 (1997).

[136] F. A. Rajgara, M. Krishnamurthy, and D. Mathur, "Electron rescattering and the dissociative ionization of alcohols in intense laser light," J. Chem. Phys. **119**, 12224 (2003).

[137] H. Stapelfeldt, E. Constant, and P. B. Corkum, "Wave Packet Structure and Dynamics Measured by Coulomb Explosion," Phys. Rev. Lett. **74**, 3780 (1995).

[138] H. Stapelfeldt and T. Seideman, "Aligning molecules with strong laser pulses," Rev. Mod. Phys. **75**, 543 (2003).

[139] R. Velotta, N. Hay, M. B. Mason, M. Castillejo, and J. P. Marangos, "High-Order Harmonic Generation in Aligned Molecules," Phys. Rev. Lett. **87**, 183901 (2001).

[140] R. de Nalda, E. Heesel, M. Lein, N. Hay, R. Velotta, E. Springate, M. Castillejo, and J. P. Marangos, "Role of orbital symmetry in high-order harmonic generation from aligned molecules," Phys. Rev. A **69**, 031804(R) (2004).

[141] A. A. Hoops, J. R. Gascooke, A. E Faulhaber, K. E. Kautzman, and D. M. Neumark, "Fast beam studies of I_2^- and $I_2^- \cdot$Ar photodissociation," Chem. Phys. Lett. **374**, 235 (2003).

[142] A. A. Hoops, J. R. Gascooke, A. E Faulhaber, K. E. Kautzman, and D. M. Neumark, "Two- and three-body photodissociation of gas phase I_3^-," J. Chem. Phys. **120**, 7901 (2004).

[143] S. S. Liu and S. D. Liu, *Te Shu Han Shu* (*Special Functions*) (China Meteorological Press, Beijing, China 1988), Chap. 11.1.5.

[144] NIST webpage on Uncertainty of Measurement Results (http://physics.nist.gov/cuu/Uncertainty/index.html).

[145] Description of Poisson distribution can be easily found in most statistical textbooks or online, for example, Eric W. Weisstein, "Poisson Distribution," From MathWorld – A Wolfram Web Resource, http://mathworld.wolfram.com/PoissonDistribution.html.

[146] Description of bisection root-finding method can be easily found in most books about scientific computation or online, for example, Eric W. Weisstein, "Bisection," From MathWorld – A Wolfram Web Resource, http://mathworld.wolfram.com/Bisection.html.